Università degli Studi di Firenze

Dipartimento di chimica

Dottorato di Ricerca in Scienze Chimiche

XXIII Ciclo

CHIM/02 – Chimica Fisica

Synthesis and characterization of nanoparticles for industrial application and for cultural heritage preservation

Sintesi e caratterizzazione di nanoparticelle per applicazioni industriali e per la preservazione del patrimonio culturale

Ph.D. Thesis by

Nicola Toccafondi

Tutor

Prof. Piero Baglioni

Coordinator

Prof. Andrea Goti

Index

Chapter 1 - Introduction

1.1 The world of nanoparticles

There is no universally accepted definition of a nanoparticle, but one given in the new PAS71 document is: *"A particle having one or more dimensions of the order of 100 nm or less"*. There is a note associated with this definition: *"Novel properties that differentiate nanoparticles from the bulk material typically develop at a critical length scale of under 100 nm"*. The above mentioned *"novel properties"* are entirely dependent on the fact that at the nano-scale, the physics of nanoparticles is different from that of the bulk material. This makes the size of particles or the scale of its features the most important attribute of nanoparticles.

The field of nanoparticle research covers a wide range of interests in the fields of chemistry, physics, biology, medicine, environmental, materials science, etc... Control of the nanoscale morphology enables precise control of the properties of the end product. Particle size, morphology and composition can be manipulated to produce materials with different properties. Some nanoparticle application areas include colloidal dispersions, metallic nanoparticles, biopolymers and nanostructured materials.

1.1.1 Optical properties

Nanoparticles can increase the optical properties of the materials: (**i**) anti-reflection coatings with silica nanoparticles [1] applied to the surface of lenses and other optical devices reduce reflection. This improves the efficiency of the system since less light is lost. In a telescope, the reduction in reflections also improves the contrast of the image by elimination of stray light. This is especially important in planetary astronomy. (**ii**) Tailored refractive index of low losses hydrib-organic–inorganic waveguides

constituted by (3-glycidoxypropil)trimethoxisilane and ZnO nanoparticles. The refractive index depends on the organic/inorganic molar ratio between GPTS–ZnO [2]. (**iii**) Electrochromics are materials that change their color upon application of an electric field. Even if the applications are currently limited to side and rear-view mirrors, sunglasses, sun-roofs and, in general, small area glazing, a number of leading manufacturers have now demonstrated the commercial viability of products incorporating electrochromic materials. G.D. Filpo describes the fabrication and the characterization of a new nanostructured and self-supplied photoelectrochromic device [3]. The main properties of the produced film were its all-solid nature, its fast coloration time as well as its fast bleaching time. The photoelectrochromic film was manufactured by coating dye functionalized TiO_2 nanoparticles (dye-TiO_2) on a layer of WO_3 nanoparticles.

1.1.2 Storage devices

Single domain ferromagnetic alloy nanoparticles have tremendous potentiality in the application of storage device [4]: (**i**) CoPt alloy nanoparticles with high coercivity and small grain size are one of the potential candidates having its application in high-density storage media manufacturing [5]. (**ii**) Magnetic nanoparticles can create improved detail and contrast in MRI images. Gadolinium lipid nanoparticles (Gd-LNP), with its 7 unpaired electrons in 4f orbitals that provide a very large magnetic moment, is proven to be among the best agents for contrast enhanced MRI [6].

1.1.3 Thermal properties

The thermal properties of nanoparticles have a great interest in various application areas: (**i**) in organic polymer-inorganic particles nanocomposites, since they often exhibit unique properties, as improved mechanical and thermal properties compared to the pristine polymer [7]. (**ii**) The integrated solar collector is considered to be a promising direction for increasing the economic feasibility of low-temperature solar systems for heating water in domestic and industrial applications. Nanofluids using Carbon Nanotubes (CNT) which enhances the thermal properties for solar thermal energy storage applications [8]. (**iii**) It is well known that the poor heat transfer properties of conventional coolants such as water, ethylene glycol and engine oils acts as a primary barrier to the development of

energy-efficient heat exchangers. There have been strong demands for more efficient heat transfer fluids in many industries: the innovative idea of 'nanofluids', i.e. dispersions of nanosized material in liquid (e.g. Al_2O_3 and transformer oil) [9], has been developed by Dr. Choi of Argonne National Laboratory in 1995 [10].

1.1.4 Mechanical properties

The mechanical properties of polymers or alloys can be improved by using nanoparticles: (**i**) Functionally graded materials (FGM) are a novel engineering material developed in the mid-1980s. The character of FGM is that its properties change with change in composition and structure. The materials can be designed for specific function and applications. Various approaches based on the bulk (particulate processing), preform processing, layer processing and melt processing are used to fabricate the functionally graded materials. An example of FGM, one side of a ceramic/metal FGM is characterized by good heat insulation, wear resistance, high hardness, temperature resistance, corrosion resistance, etc., like a ceramic, and the other side has metallic characters such as high heat conductivity. One of the most important types of FGM is composite coatings. Composite coatings consist of a metal or alloy matrix containing a dispersion of second phase particles. These particles can be hard oxide or carbide particles, such as Al_2O_3, SiC, TiO_2, WC, SiO_2 or diamond, a solid lubricant, such as PTFE, graphite or MoS_2, or even liquid-containing microcapsules. Composite coatings can be an attractive alternative, particularly to chromium coatings. Composite coatings have applications as coatings of engine cylinders, high-pressure valves and dies and in the production of musical instruments, drill fittings, car accessories and small aircraft and electrotechnical parts [11,12]. The formation of electrodeposited graded electrolyte is maintained at a predetermined value by a Ni–Al_2O_3 nanocomposite [13], or a Ni–SiC nanocomposite [14], coatings by changing the process variables. (**ii**) Also the organic-inorganic hybrid nanomaterials are very important for their extraordinary properties, which arise from the synergy between the properties of the respective components. They comprise inorganic networks, homogenously dispersed in organic polymer matrix. The hybrid materials have gained much interest in recent years because of the remarkable changes in mechanical properties [15]. Composites have been prepared by the mechanical blending of polymers and glass fibers or other inorganic nanomaterials to reinforce unfilled polymers. If the dispersion is homogeneous with a narrow size distribution of the filler, the mechanical

properties would be expected to be further improved and/or new unexpected features might appear [16].

1.1.5 Electronic components

High performance and smaller electronic components can be achieved by means of nanoparticles: (**i**) capacitors for small consumer devices such as mobile phones. Nanodielectrics is an emerging field with applications in capacitors, gate dielectrics, energy storage, alternatives to Li-ion batteries, and frequency modulation in communications devices. Self-assembly of high k dielectric nanoparticles is a highly attractive means to produce nanostructured films with improved performance (namely dielectric tunability, low leakage, and low loss) as a function of size, composition, and structure. One of the major challenges is conversion of the nanoparticle building block into a reliable thin film device at conditions consistent with integrated device manufacturing or plastic electronics. The development of $BaTiO_3$ and $(Ba,Sr)TiO_3$ superparaelectric uniform nanocrystal (8–12 nm) films prepared at room temperature by evaporative driven assembly with no annealing step has been reported by Limin Huang et al [17]. Thin film inorganic and polymer composite capacitors show dielectric constants in the tunable range of 10÷30, dependent on composition, and are confirmed to be superparaelectric. Organic thin film transistor (TFT) devices on flexible substrates demonstrate the readiness of nanoparticle-assembled films as gate dielectrics in device fabrication. (**ii**) Displays that are cheaper, larger, brighter, and more efficient can be produced by using nanoparticles. For example, efficient electron injection is an important issue in the bottom-emission inverted OLED (Organic Light-Emitting Diode) structure because there are few proper cathode materials. In the Hyunkoo Lee's work [10.1063/1.3400224] has been reported how a zinc oxide nanoparticles layer lowered the turn-on voltage by about 4 V and significantly enhanced the efficiency. The device with ZnO nanoparticles showed peak efficiencies of 16.5 cd/A and 8.2%, about three times higher than those of the device without ZnO nanoparticles. Since the ZnO nanoparticles layer has a wide band gap, good electron transporting properties and low work function, it can be utilized as an effective electron injection layer with good transparency. (**iii**) Components using high conductivity materials. The conductive fillers used mostly were metallic powders [18,19], carbon black and graphite [20] usually incorporated into insulating polymers to produce electrical conducting composites. Carbon black has already been widely used to fabricate conducting composite in industry. Graphite has been attracting

considerable research interest due to its good electrical conductivity at room temperature (10^6 S m^{-1}). Each of the fillers mentioned above can achieve satisfying electrical conductivity by adding rather high loadings of fillers into insulating polymers (about 20 wt%), but this would lead to processing difficulties and result in mechanical redundancy of composites. Another conductive filler that has been used is carbon nanotubes which exhibit very low electrical percolation threshold in matrix (~0.3÷0.5 phr) and at the same time are more costly as compared with expanded graphite. (**iv**) Computer circuits, radio transmitters, electric motors, overhead power lines and others electronic devices interferes in the radio frequency range (10^4÷10^{12} Hz) with the function of electronic circuits of many components because of Electromagnetic Interference (EMI). Preventing it is in increasing demand due to the increasing abundance and sensitivity of electronics, particularly radio frequency devices, which tend to interfere with digital devices. Polymer compounds containing EMI shielding additives have several advantages over metals and conductive coatings. Compared to metals, conductive polymer nanocomposites have well-known advantages of lighter weight, greater design freedom, corrosion resistance, and cost-effectiveness. A novel polyvinyl chloride reinforced graphite/copper nanoparticles to provide enhanced electromagnetic interference shielding performance within the frequency range from 1 GHz to 20 GHz was successfully fabricated [21].

1.1.6 Energy development

Energy development, a very frequent topic, is the effort to provide sufficient primary energy sources and secondary energy forms for supply, cost, impact on air pollution and water pollution, mitigation of climate change with renewable energy. The energy development is highly affected by the progress in nanoparticles research. (**i**) For example, a thin film of gold nanoparticles (GNPs) is a promising anode buffer layer to replace the role of poly(3,4-ethylene dioxythiophene):poly(styrene sulfonate) PEDOT:PSS film in organic solar cells. The GNPs are selected because of their inert and conducting behavior. Efficient charge collection of the GNPs coated ITO anode in the solar cells is attributed to its good conductivity, high work function (~5.1 eV) and smooth morphology [22]. (**ii**) The efforts to improve the energy density of batteries and them durableness. $LiFePO_4$ (LFP) has been extensively studied owing to its use as the active cathode element in a new-generation of lithium-ion batteries [23]. This success is due to its environmental compatibility, thermal stability, and long cycling

life [24]. The LFP nanoparticles have very small electronic conductivity, but it is a common practice in the production of Li-ion battery cathodes to add carbon either to the $LiFePO_4$ matrix or by surface coating the $LiFePO_4$ particles with thin layers of carbon. (**iii**) The continued and significant interest in novel light element solid-state hydrogen (H) storage media has triggered the investigation of an impressively rich diversity of candidate materials. The nanoscale materials engineering has been proposed to make H-sorption reactions reversible at practical temperature and pressure because it offers a high number of interacting effects: microstructure refinement down to the nanometer range, reduced dimensionality, addition of nanocatalysts, synergy, and physical coupling among complementary phases. Small magnesium nanoparticles display interesting desorption/absorption kinetic performances [25], even if suffer from a low gravimetric capacity due to high oxide content. (**iv**) Proton exchange membrane fuel cells (PEMFC) employing hydrogen as a fuel cell provide an efficient and clean alternative to the presently used internal combustion engines. PEMFC converts the chemical energy of hydrogen fuel directly into electrical energy, thereby offering high efficiency with little pollution. The operating characteristics of PEMFC including the low temperature of operation are particularly attractive for transportation applications. Considerable worldwide research is being undertaken for the commercialization of the PEMFC technology. However, the cost and durability issues are major barriers for large-scale manufacturing and deployment of PEMFC. A novel class of nanostructured Pt-Cu alloy particle materials for use as oxygen reduction electrocatalyst in polymer electrolyte membrane fuel cells has been proposed [26,27]. (**v**) The efficiency improving of catalysts for emissions of the combustion engines can be supplied by using the nanoparticles. Nanometer zinc oxide supported colloidal gold catalysts with self-designed equipment has been proposed and evaluated for benzene catalytic oxidation and it has been proved that benzene has been completely oxidized into CO_2 and H_2O over this Au/ZnO catalyst at low temperature [28].

1.1.7 Biomedical applications

The nanoparticles are of interest because of their many potential biomedical applications: (**i**) The calcium ion is the most abundant cation in the body, and participates in various biological activities such as skeletal mineralization, blood coagulation, neurotransmission, excitation of skeletal and cardiac muscle, and stimulus-mediated hormone secretion.

Calsequestrin functionalized gold nanoparticles undergo calcium-dependent calsequestrin polymerization, which results in a clear color change together with precipitation. The sensing system is specific for Ca^{2+} ions and the differences between normal and disease-associated abnormal (hypercalcemia) Ca^{2+} ion levels in serum can be distinguished with the naked eye. (**ii**) Bioactive glasses of silicate composition, which were first developed by Hench and co-workers in 1969 [29], represent a group of surface reactive materials which are able to bond to bone in physiological environment. Bioactive glasses most widely used in biomedical applications consist of a silicate network incorporating sodium, calcium and phosphorus in different relative proportions. The classical 45S5 bioactive glass composition universally known as Bioglass®, for example, has a composition in wt.% of 45% SiO_2, 24.5% Na_2O, 24.5% CaO and 6% P_2O_5. Early applications of bioactive glasses were in the form of solid pieces for small bone replacement, i.e. in middle ear surgery. More recently, great potential has been attributed to the application of bioactive glasses in tissue engineering and regenerative medicine. Bone tissue engineering is one of the possible most exciting future clinical applications of bioactive glasses, e.g. to fabricate optimal scaffolds with osteogenic and angiogenic potential. A reduction in size to the nanometer scale of bioactive glass particles (or fibres) leads to a new family of nanostructured biomaterials which, combined with polymer matrices to form composites, are expected to exhibit enhanced performance in existing biomedical applications, leading also to new application opportunities. There is evidence in the literature that faster deposition or mineralization of tissues such as bone or teeth is possible when these tissues are in contact with nanoscale particles, as opposed to micron-sized particles, considering that the bone structure exhibits nanoscale features consisting of a tailored mixture of collagen fibrils and hydroxyapatite nanocrystals. For bone tissue engineering purposes, where polymer/bioactive glass composite scaffolds are of great interest, the use of nanoscale bioactive glasses is expected to improve both mechanical and biological properties of scaffolds. Not only the surface bioreactivity of nanoparticles is higher than that of μm-size particles but also bioactive glass nanoparticles will induce nanostructured features on scaffold surfaces, which are likely to improve osteoblast cell attachment and subsequent cell behavior. Other advantages of the reduced size of the inorganic particles include the possibility to use them to reinforce polymeric nanofibers, to process thin bioactive coatings or in injectable systems. (**iii**) Contact lenses often get infected with bacteria, and prolonged usage of such lenses leads to microbial keratitis in eye. Bacteria [30]

frequently adhere to the surface of the lens through a biofilm matrix, a three-dimensional, gel-like, highly hydrated and locally charged environment, and using such lens can cause infections in eye. The silver nanoparticles composing gel may be used as a safe biocide for destroying different bacterial biofilms [31]. (**iv**) Since their discovery, lipid vesicles have attracted growing interest for their potential applications as drug delivery vectors. One of the major features of a drug carrier is the release of the encapsulated drug selectively at the target site with an efficient rate. This can be obtained through the destabilization of the delivery system by an external *stimulus*. A way to tune the permeability is the encapsulation of superparamagnetic nanoparticles into the aqueous pool of liposomes and the modulation of the trans-membranal drug diffusion by applying an external alternating magnetic field.

1.1.8 Environmental applications

The nanoparticles are of interest because of their many potential environmental applications: (**i**) the zero-valent iron nanoparticles are characterized by high surface areas and reactivity and an important application of these particles is subsurface injection for the remediation of groundwater contaminated with chlorinated aliphatic hydrocarbons [32]. The employment of iron nanoparticles for waste water disinfection has also been proposed. Unlike many other nanomaterials, which may accidentally enter the environment, large concentrations of iron nanoparticles may be intentionally released [33]. (**ii**) Trinitroglycerin is an industrial chemical mostly known for its clinical use in treating angina and manufacturing dynamite. The wide manufacture and application of trinitroglycerin has led to contamination of vast areas of soil and water. The iron nanoparticles can lead to degradation of trinitroglycerin, transforming it to two benign products, ammonium cation and glycerol [34]. (**iii**) Metal oxide nanocatalysts are being developed for the prevention of pollution due to industrial emissions and the photocatalytic properties of titanium dioxide nanoparticles can be exploited to create self-cleaning surfaces that reduce existing pollution. Titanium dioxide is a potent oxidising agent when exposed to UV radiation and is able to break down VOCs, nitrous oxides and other pollutants into less harmful species. Irradiation with photons of energy >3.2 eV generates electron pairs and hole pairs that cause redox actions with oxygen and water molecules, forming oxygenated free radicals that react with the compounds adsorbed on the surface, leading to their degradation [35].

1.1.9 Cultural heritage preservation

Nanoparticles provide new concepts and materials for the cultural heritage preservation: (**i**) calcium and barium hydroxide nanoparticles offer a versatile and highly efficient tool to combat the main degradation processes altering wall paintings. Clear example of the efficacy and potentiality of nanotechnology is represented by the conservation in situ of Maya wall paintings in the archaeological area in Calakmul (Mexico) [36]. (**ii**) Surfaces that interact with the environment are the most prone to aging and decay; accordingly, soiling is a prime factor in the degradation of surfaces and the disfigurement of a piece. Polymers coatings that were originally intended to protect or contribute aesthetically to an artwork should be removed if they begin to have a destructive impact on its appearance or surface chemistry. Since the mid-19th century, organic solvents have been the method of choice for cleaning painted surfaces and removing degraded coatings but often the surface of wall paintings have been damaged and compromised by using "free" solvents. The use of gels and poultices helps localizing the solvent and, in some cases, reducing solvent permeation into underlying paint layers. Unfortunately, it is not always easy to remove gels and their residues from a paint surface. Incorporation of magnetic, coated-ferrite nanoparticles into polyacrylamide gels adds functionality to a versatile system comprising oil-in-water microemulsions, aqueous micellar solutions, or xerogels that act as sponges. The ferrite particles allow the use of magnets both to place the gels precisely on a surface and to lift them from it after cleaning [37]. (**iii**) Magnesium hydroxide nanoparticles dispersed in alcohols inhibit two different and synergistic degradation processes usually affecting historically valuable manuscripts and, more in general, paper documents: acid hydrolysis and oxidative ink corrosion [38].

The nanoparticles application is, however, an extremely broad topic and is beyond the purpose of this dissertation, the main subject of which is the development and the synthesis of novel nanoparticles and innovative polymer nanocomposites.

1.2 Syntheses of Nanoparticles

Ever since Faraday reported in 1857 the preparation of gold sols of different colors [39], scientists have been fascinated by monodispersed colloids. However, systematic studies of the synthesis, properties, and mechanisms of formation of such colloids have been initiated only a quarter of a century ago. Since then, a large number of uniform dispersions of particles of simple and mixed chemical compositions and various shapes, ranging in modal size from several nanometers to several micrometers, have been described in the literature. The method of choice has been precipitation from homogeneous solutions, either directly or via gel/sol or sol/gel routes. Numerous books [40] and review articles [41,42] cover the theory of coprecipitation.

Although precipitation can be induced in a number of ways, chemical reactions are the most common method for the synthesis of nanoparticles. Generally, chemical reactions are chosen so that the result is a low solubility product, so that the solution quickly reaches supersaturation. The chemical reactions used to induce coprecipitation are numerous. For illustrative purposes, we consider the case of a simple addition reaction for the formation of an electrolyte, A_xB_y:

$$xA^{+y}\,(aq) + yB^{-x}\,(aq) \Leftrightarrow A_xB_y\,(s)$$

The equilibrium relationship between the product and its reactants is expressed as the solubility product constant, K_{sp}:

$$K_{sp}=[a_A]^x[a_B]^y$$

where a_A and a_B are the activities of cation A and anion B in aqueous solution. K_{sp} values tend to be very low for many hydroxides, carbonates, oxalates, and chalcogenides in aqueous solutions.

1.2.1 Precipitation parameters

Beyond simple addition/exchange reactions, precipitation can be induced by numerous other methods, such as chemical reduction, photoreduction, oxidation, and hydrolysis. Alternatively, precipitation can be induced by altering other parameters related to solubility, like temperature and

concentration. When the product contains only one or two elements (e.g. a metal, binary oxide, etc.), precipitation reactions are relatively simple. However, in ternary and quarternary systems, the process becomes more complex, as multiple species must be precipitated simultaneously (hence, the term *coprecipitation*). The precipitation of a compound does not guarantee that the product will be nanoparticulate and/or monodispersed. The processes of nucleation and growth govern the particle size and morphology of products in precipitation reactions. When precipitation begins, numerous small crystallites initially form (nucleation), but they tend to quickly aggregate together to form larger, more thermodynamically stable particles (growth). From a quick analysis of the equations descripting these two phenomena, the temperature plays a fundamental role.

$$R_N = A\exp\left(\frac{-16\pi\sigma_{SL}^3 v^2}{3k^3T^3\ln^2 S}\right) \qquad G = k_G S^g$$

where R_N is the homogeneous nucleation rate, N the number of nuclei formed per unit time per unit volume, A a pre-exponential factor (typically ranging from 10^{25} to 10^{56} $s^{-1}m^{-3}$), σ_{SL} the surface tension at the solid-liquid interface, v the atomic volume of solute, k the Boltzmann constant, T is temperature, and S the supersaturation as defined by $S = C/C_{eq}$, where C and C_{eq} are the solute concentrations at saturation and at equilibrium, respectively; and the rate of growth, G, where k_G is the growth rate constant and g is the growth order.

High temperature guarantees a higher homogeneous nucleation rate R_N than the growth one, preventing the growth of the particles.

Since the thermodynamics of precipitation promotes the maximization of the surface/volume ratio, the agglomeration of small particles precipitated from solutions is practically inevitable without a stabilizer. There are generally two approaches to nanoparticle stabilization: (**i**) steric repulsion between particles caused by surfactants, polymers, or other organic species bound to the nanoparticles surfaces (generically referred to as capping ligands) and (**ii**) electrostatic repulsions resulting from the chemisorption of charged species at the surfaces (peptizing).

1.2.2 Chemical reductions: metal nanoparticles

Due to their widespread application as catalysts, metals precipitated from aqueous solutions continue to be a thoroughly investigated subject. The precipitation of metals from aqueous or nonaqueous solutions typically requires the chemical reduction of a metal cation. Reducing agents take many forms, the most common of which are gaseous H_2, solvated sodium or potassium borohydride ($NaBH_4$ or KBH_4), hydrazine hydrate ($N_2H_4 \cdot H_2O$) and hydrazine dihydrochloride ($N_2H_4 \cdot 2HCl$).

Hydrazine hydrate is freely soluble in water, but since N_2H_4 is basic, the chemically active free-ion is normally represented as $N_2H_5^+$:

$$N_2H_4 + H_2O \Leftrightarrow N_2H_5^+ + OH^-$$

The standard reduction potential for the hydrazinium ion is E^0=-0.23V.

$$N_2 + 5H^+ + 4e^- \Leftrightarrow N_2H_5^+$$

In theory, the reduction of any metal with an E^0 more positive than -0.23 V, should be possible at room temperature, given a sufficient excess of reducing agent and proper control of pH. With respect to precipitating metals from solution, this would obviously include many first-row transition metal ions, such as Fe^{2+}, Fe^{3+}, Co^{2+}, Ni^{2+}, and Cu^{2+}, but also many second- and third-row transition metals, as well as most post-transition elements and a few nonmetals. In practice, the reduction of some metal ions with $E^0 > -0.23$ V is either not feasible or extremely difficult, but this is usually due to the instability of the cation in aqueous environments. In some instances, transition metal cations, such as Rh^{3+}, form stable complexes with hydrazine, thereby greatly limiting the available options for carrying out a reduction. In many cases, an organic capping agent that is normally used to prevent agglomeration, can also serve as the reducing agent. This is the case in the well-known Turkevich process for the synthesis of gold colloids [43] prepared by boiling a mixture of dilute $HAuCl_4$ and sodium citrate.

1.2.3 Meatl oxide nanoparticles

The precipitation of oxides, from both aqueous and nonaqueous solutions, is somewhat less straightforward than the precipitation of metals. Reactions for the synthesis of oxides fall into two categories: those that produce an oxide directly and those that produce a precursor that must be further processed (drying, calcination, etc.). In either case, monodispersed nanoparticles of oxides, like those of metals, frequently require a capping ligand or other surface-bound stabilizer to prevent agglomeration of the particles. In those cases where calcination or annealing of the samples is necessary, some agglomeration will be unavoidable. Nanoparticles can nonetheless be so obtained, but there is little chance of the particles being monodispersed. For many of the reported syntheses of oxides, monodispersity of the products was neither a requirement nor a priority for the researchers involved. Chinnasamy et al. reported an extensive series of experiments for the spinel-structured $CoFe_2O_4$ designed to determine the influence of reaction temperature, reactant concentration and reactant addition rate on the size of the products [44]. In each case, aqueous solutions of Fe^{3+} and Co^{2+} were precipitated with dilute NaOH. NaOH concentrations of 1.5 M or greater resulted in the formation of a secondary FeOOH phase, and slowing the NaOH addition rate appeared to broaden the particle size distribution.

1.2.4 Sonochemical reactions

In sonochemistry, an acoustic cavitation process (the implosive collapse of bubbles) can generate a transient localized hot zone with extremely high temperature gradient and pressure. The sonication creates localized “hot spots” with effective temperatures of 5000 K and lifetimes on the order of a few nanoseconds or less [45]. Such sudden changes in temperature and pressure assist the destruction of the sonochemical precursor (e.g. organometallic solution) and the formation of nanoparticles. The technique can be used to produce a large volume of material for industrial applications. Many of the methods reported in the literature for sonochemical syntheses of nanoparticles involve the decomposition of carbonyl precursors, e.g. the nanoparticles of Fe, Co, and several Fe-Co alloys have been produced with this route. Typically, the corresponding metal carbonyls were dissolved in decane and irradiated at 20 kHz for 3 h under an inert atmosphere to produce well-dispersed 8 nm particles. Other

methods involve the reduction of a metal with a liquid reducing alloy of sodium and potassium [46]. For example, titanium metal powder has been produced through low intensity ultrasound in a hydrocarbon solvent at near-ambient temperatures. At first, the ultrasounds created a colloidal suspension of liquid sodium-potassium alloy in the solvent and then reduced liquid titanium tetrachloride to titanium metal under cavitation conditions.

1.2.5 Reactions in microemulsions

Hoar and Schulman noted in 1943 that certain combinations of water, oil, surfactant, and an alcohol- or amine-based cosurfactant produced clear, seemingly homogeneous solutions that Schulman termed "micro emulsions." Schulman used the cetyltrimethylammonium bromide (CTAB), which is still used extensively today. The amphiphilic nature of the surfactants such as CTAB makes them miscible in both hydrocarbons and water, but when the surfactant is mixed with a hydrocarbon, the resulting mixture, although optically isotropic, cannot be properly described as a solution. As noted by Schulman, the orientation of the surfactant molecules is not random. Instead, the surfactant, through ion-dipole interactions with the polar cosurfactant, forms spherical aggregates in which the polar heads of the surfactant molecules orient toward the center. The cosurfactant acts as an electronegative "spacer" that minimizes repulsions between the positively charged surfactant heads. The addition of water to the system will cause the aggregates to expand from the center as the water molecules (again as a result of ion-dipole and dipole-dipole interactions) situate at the center of the sphere. The small size of reverse micelles subjects them to continuous Brownian motion, even at room temperature. Collisions between micelles are frequent, and approximately one collision in every thousand results in the formation of a short-lived dimer, formed by the expulsion of some surfactant molecules into the bulk oil phase. During the lifetime of the dimer, two reverse micelles will exchange the contents of their aqueous cores before decoalescing, resulting in the eventual equilibrium distribution of all contents. Given the above model of reverse micelle interaction, the suitability of reverse micelles as nanoreactors becomes evident. Microemulsions have been used for synthesis of metallic, semiconductor,

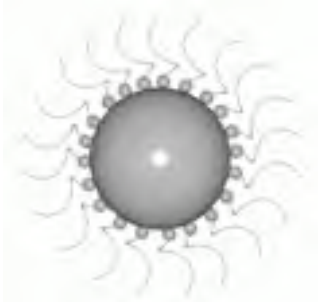

silica, barium sulfate, magnetic, and superconductor nanoparticles. By controlling the very low interfacial tension (~10^{-3} mN/m) through the addition of a cosurfactant (e.g., an alcohol of intermediate chain length), these microemulsions are produced spontaneously without the need for significant mechanical agitation. The technique is useful for large-scale production of nanoparticles using relatively simple and inexpensive hardware.

1.2.6 Sol-gel processing

The versatility and general usefulness of modern sol-gel processing is reflected in the sheer volume of available literature. The sol-gel process can be characterized by a series of distinct steps. Initially, a formation of stable solutions of the alkoxide or solvated metal precursor (the sol). After that, an increase in the viscosity of the solution lead to gelation resulting from the formation of a network (the gel) by a polycondensation or polyesterification reaction. Successively the aging of the gel (syneresis) starts: the polycondensation reactions continue until the gel transforms into a solid mass, accompanied by contraction of the gel network and expulsion of solvent from the gel pores. Ostwald ripening (the phenomenon by which smaller particles are essentially consumed by larger particles during the growth process) and phase transformations may occur concurrently with syneresis. The aging process of gels can exceed 7 days and is critical to the prevention of cracks in gels that have been cast. Drying of the gel is the following step, when water and other volatile liquids are removed from the gel network. This process is complicated due to fundamental changes in the structure of the gel. If isolated by thermal evaporation, the resulting monolith is called xerogel. If the solvent is extracted under supercritical or near-supercritical conditions, the product is an aerogel. The final step is the dehydration, during which surface-bound M-OH groups are removed, thereby stabilizing the gel against rehydration. This is normally achieved by calcining the monolith at temperatures up to 800 °C. If the sol-gel process is used to the preparation of dense ceramics or glasses, a further step above 800 °C is made to densify and decompose the gel. The pores of the gel network are collapsed, and remaining organic species are volatilized. In any event, experimental evidence suggests that precursor structure is at least as important as control of pH in directing the size and morphology of sol-gel products. For the purpose of preparing nanoparticles, base-catalyzed hydrolysis is preferred, though not always necessary.

1.2.7 Solvothermal processing

In a sealed vessel (high pressure reactor, autoclave, bomb), solvents can be brought to temperatures above their boiling points by the increase in pressures resulting from heating. A chemical reaction under such conditions is called solvothermal processing or, in the case of water as solvent, hydrothermal processing. The critical point for water lies at 374 °C and 218 atm. Above this temperature and pressure, water is said to be supercritical. Supercritical fluids exhibit characteristics of both a liquid and a gas: the interfaces of solids and supercritical fluids lack surface tension, yet supercritical fluids exhibit high viscosities and easily dissolve chemical compounds that would otherwise exhibit very low solubilities under ambient conditions. Even though some solvothermal processes involve supercritical solvents, most simply take advantage of the increased solubility and reactivity of metal salts and complexes at elevated temperatures and pressures without bringing the solvent to its critical point. In any event, solvothermal processing allows many inorganic materials to be prepared at temperatures substantially below those required by traditional solid-state reactions. Unlike the cases of coprecipitation and sol-gel methods, which also allow for substantially reduced reaction temperatures, the products of solvothermal reactions are usually crystalline and do not require postannealing treatments.
Microwave-assisted solvothermal methods are somewhat less commonly encountered in the literature. Although these methods were originally developed in the interest of reducing reaction times, in the last years particle sizes was reduced by using microwave to reach high temperature and pressure.

1.3 Nanocomposites

The use of organic or inorganic fillers has become fundamental in polymeric systems. Polymer composites are manufactured commercially for many diverse applications such as sporting goods, aerospace components, automobiles, etc. In the last decades, there has been a strong emphasis on the development of polymeric nanocomposites, where at least one of the dimensions of the filler material is of the order of a nanometer. In general, the unique combination of the nanomaterial's characteristics, such as size, mechanical properties, and low concentrations necessary to change the

polymer matrix, coupled with the advanced characterization and simulation techniques now available, have generated a great amount of interest in the field of nanocomposites. In addition, many polymer nanocomposites can be fabricated and processed in ways similar to that of conventional polymer composites, making them particularly attractive from a manufacturing point of view. Nature has mastered the use of nanocomposites, and researchers, as usual, are learning from their natural surroundings.

Figure 1. The wood structure on the left from the macroscale to the molecular structure. On the righ, a section of a seashell.

Using natural reagents and polymers such as carbohydrates, lipids, and proteins, nature makes strong composites such as bones, shells [47], and wood. These are examples of nanocomposites, made by mixing two or more phases such as particles, layers or fibers, where at least one of the phases is in the nanometer size range. In the early 1990s, Toyota Central Research Laboratories in Japan reported work on a Nylon-6 nanocomposite, for which a very small amount of nano filler loading caused a pronounced improvement of thermal and mechanical properties. The properties of nanocomposite materials depend not only on the properties of their individual parents (nano filler and nylon, in this case), but also on their morphology and interfacial characteristics. The properties of a nanocomposite are greatly influenced by the size scale of its component phases and the degree of mixing between the two phases. Depending on the nature of the components used (layered silicate or nanofiber, cation exchange capacity, and polymer matrix) and the method of preparation,

significant differences in composite properties may be obtained [49].

Properties	Feature size (nm) at which changes might be expected
Catalytic activity	<5
Making hard magnetic materials soft	<20
Producing refractive index changes	<50
Producing super paramagnetism and others electromagnetic phenomena	<100
Producing strengthening and toughening	<100
Modifying hardness and plasticity	<100

Table 1. Feature sizes for significant changes in properties reported in nanocomposite systems [48].

For example, figure 2 represents three main types of composites for layered silicate materials. When the polymer is unable to intercalate (or penetrate) between the silicate sheets, a phase-separated composite is obtained, and the properties remain in the same range as those for traditional microcomposites.

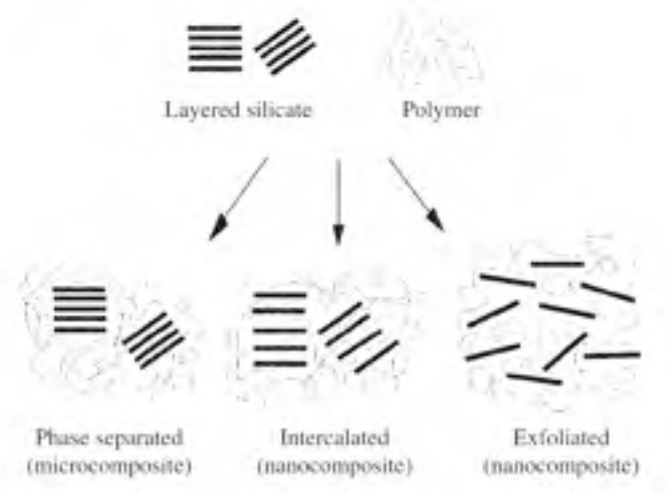

Figure 2. Scheme of three main types of layered silicates in polymer matrix [50].

In an intercalated structure, where a single extended polymer chain can penetrate between the silicate layers, a well-ordered multilayer morphology results with alternating polymeric and inorganic layers. When the silicate layers are completely and uniformly dispersed in a continuous polymer

matrix, an exfoliated or delaminated structure is obtained. In each case, the physical and mechanical properties of the resultant composite are significantly different. Without proper dispersion, the nanomaterial will not offer improved mechanical properties over that of conventional composites, in fact, a poorly dispersed nanomaterial may degrade the mechanical properties. By optimizing the interfacial bond between the particle and the matrix, one can tailor the properties of the overall composite, similar to what is done in macrocomposites. For example, good adhesion at the interface will improve properties such as interlaminar shear strength, delamination resistance, fatigue and corrosion resistance. Flammability is another important issue for many applications. Nanocomposites prepared from the nylon family, epoxy, polystyrene or vinyl ester, exhibit reduced flammability compared to pure polymers.

Two principal factors cause the properties of nanomaterials to differ significantly from other materials: increased relative surface area and quantum effects. Some nanocomposites may show properties predominated by the interfacial interactions and others may exhibit the quantum effects associated with nanodimensional structures.

For preparing polymer nanocomposites, the interaction mechanism (pressure drop into the nano gallery, miscibility between polymer and filler, hydrogen bonding, electrostatic, coordination, etc.) of the polymer and filler depends on the polarity, molecular weight, hydrophobicity, reactive groups, etc. of the polymer, and the type of solvent, i.e., water, polar, or nonpolar organic liquids and filler type. Using the *in situ* intercalative polymerization technique, polymer formation can occur in between the nanoparticle clusters (or intercalated sheets). In situ polymerization is based on the following procedure: swelling of the clusters (or layered filler) within the liquid monomer and the polymerization can be initiated either by heat or radiation, by the diffusion of a suitable initiator, or by an organic initiator [52,53]. At first this approach was successfully applied in manufacturing of nylon nanocomposite, and later it was extended to other thermoplastics [54].

One obvious advantage of in situ polymerization is the tethering effect, which, in the case of Montmorillonite as filler for example [51], enables the nanoclay's surface organic chemical, such as 12-aminododecanoic acid

(ADA), to link with nylon-6 polymer chains during polymerization, as illustrated in figure 3.

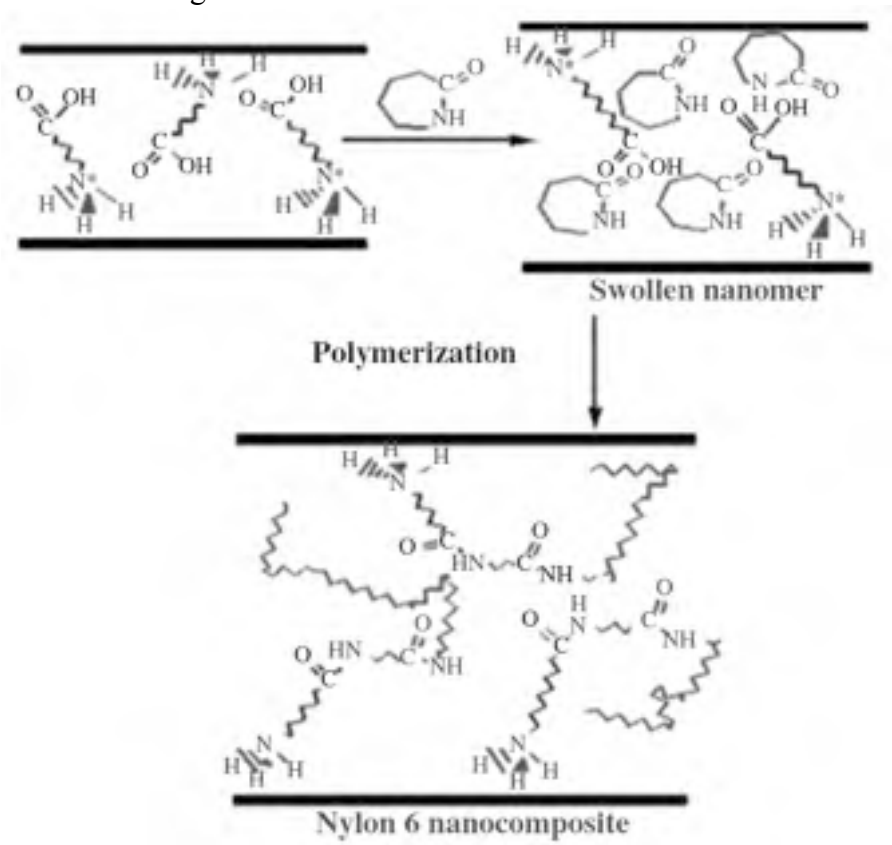

Figure 3. Nylon-6 nanocomposite formed through in situ polymerization with ADA-Montmorillonite [51].

Organically modified clays dispersed in a nylon-6 matrix greatly improved the dimensional stability. Improvement in resistance in nanocomposites plays an important role in beverage applications [55]. When the layers are delaminated, it increases the effective path length for molecular diffusion and the path becomes highly tortuous to reduce the effect of gas and moisture transmission through the film. When nano- rather than micro-particles are used, the glass transition temperature (T_g) of the nanocomposites shifts to lower values.

Nanocomposite materials hold the potential to redefine the field of traditional composite materials both in terms of performance and potential applications. There is little doubt that polymer nanocomposites have

tremendous market potential both as replacements for current composites and in the creation of new markets through their outstanding properties. But developing the processing-manufacturing technologies in terms of quantity and value for commercialization will be one of the biggest challenges. For example, dispersion of nanoparticles or chemical compatibility with matrix materials is the important issue. A homogeneous dispersion of nanoparticles in a polymer by using existing/traditional compounding techniques is very difficult due to the strong tendency of fine particles to agglomerate. At the same time if stress is applied, there is the possibility for the agglomerate nanoparticles to split. The alignment of nanoparticles in the composite matrix can be critical to maximize unidirectional properties such as strength, modulus, and toughness. As in the case of traditional composites, it is even more challenging to determine the strength, composition and functionality of the interfacial region. Moreover, scaling up is needed to produce large quantities of nanomaterials for manufacturing purposes. The commercial impact of nanocomposites may include inkjet markets, nanoparticles in cosmetics, and automotive applications such as body moldings, engine covers and catalytic converts, batteries, computer chips, memory devices, biosensors for diagnostics, advances in lighting are all possible.

1.4 Cultural Heritage: degradation problems

1.4.1 Wall painting consolidation

A large part of the artistic cultural heritage from the past is related to wall paintings performed on plaster (also named fresco paintings). Salt contamination in wall paintings is a challenge for their conservation. The paint layer is at the interface between the wall and the surrounding environment and it is strongly susceptible to degradation due to the mechanical stresses following salt crystallization, usually occurring at the surface. Saline solutions eventually impregnate the porous network of the wall and move through a capillarity mechanism. Crystallization takes place when ionic concentration exceeds saturation, often due to water evaporation at the interface. This process is generally accompanied by volume expansion; the formation of new crystals inside the pores and/or at the interface between the paint layer and the plaster generates mechanical stress and results either into lifting and detachment of the paint layer, or into

cracks and fissuring of the plaster [56]. Sulfates are commonly found as contaminant of wall paintings, since they result from the chemical degradation of calcium carbonate due to acid pollutants.

Figure 4. A detail of a *fresco* situated in Calakmul. On the left, before the restoration, the salt efflorescence damaged the wall-painting. On the right, the restored image.

As mentioned above, besides representing a symptom of an already happened chemical degradation process, sulfates favor further deterioration because of the mechanical stresses resulting from the crystallization cycles triggered by fluctuations of thermohygrometric parameters. The effects of salt crystallization are usually strongly amplified if any protective coating, possibly applied in previous restoration treatments, is present. Polymers, mainly acrylic and vynil resins, have been widely used to consolidate wall paintings and to confer to the painted layer protection and hydrorepellency [57]. Formulation based on acrylate/methacrylate and acrylate/vynilacetate co-polymers have been extensively used for decades; unfortunately they threaten the survival itself of works of art and can now be considered as one of the most dangerous sources of degradation. In the presence of polymer film, salt crystallization processes involve deeper areas with stronger decohesion and to the complete powdering of the painting. The polymer closes the surface pores generating mechanical stresses towards the paint layer. These polymers have been considered perfectly reversible materials for a long time. Unfortunately, their reversibility, i.e. the possibility to solubilize them by using the same solvent used for the application, has been

proved to be unworkable. In fact, polymer resins degrade quickly with drastic variation of their physico-chemical properties. In summary, contrary to the expectations, polymeric materials used for the protection of wall paintings have induced further degradation and their chemical modifications, such as cross-linking, strongly hampers their removal.

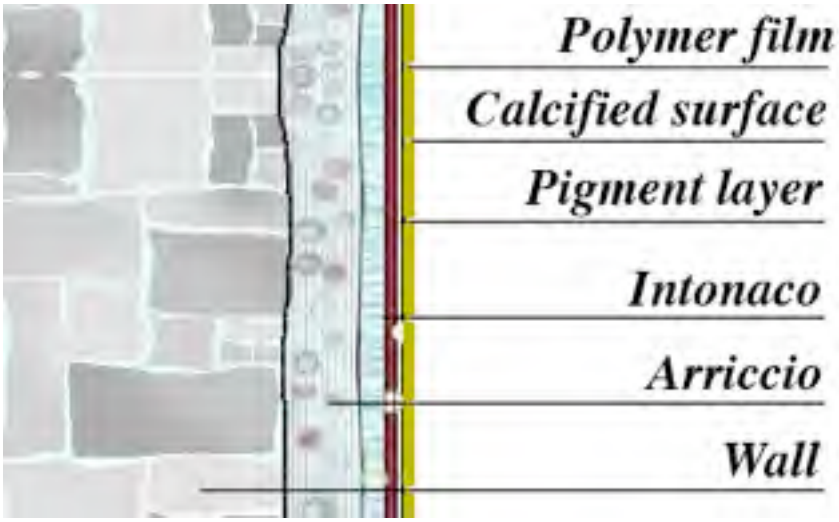

Figure 5. The cross-section of a wall supporting a *fresco*. In some cases, the surface of *frescos* is covered by a polymer film, remnant of the past restoration.

For the above reasons, the use of inorganic materials, which are compatible with wall paintings (possibly the same materials used for the artifact), minimizes the aforementioned risks and prevents from unexpected side effects. Inorganic consolidants are highly chemically stable and preserve the wall painting porosity ensuring long-lasting consolidation effects (see chapter 4).

1.4.2 Paper deacidification

Paper also deteriorates rapidly, and a full understanding of the chemical degradation mechanisms is necessary in order to develop appropriate methodologies for a long-term conservation. The main cellulose degradation pathways are the acid hydrolysis of glycosidic bonds and oxidation. Low pH values can lead to cellulose depolymerization even at room temperature. Protons hydrolyze the β (1,4)-glycosidic bond of the cellulose leading to a decrease of the chain length at the microscopic scale and to a loss of

mechanical resistance at the macroscopic scale. It is well known that during the making of iron-gall inks, gallic acid, formed by hydrolysis of tannins extracted from gall-nuts, reacts with iron (II) sulfate (i.e. *vitriol,* as reported in old recipes) to give a pyrogallate complex of iron (III) and sulfuric acid.

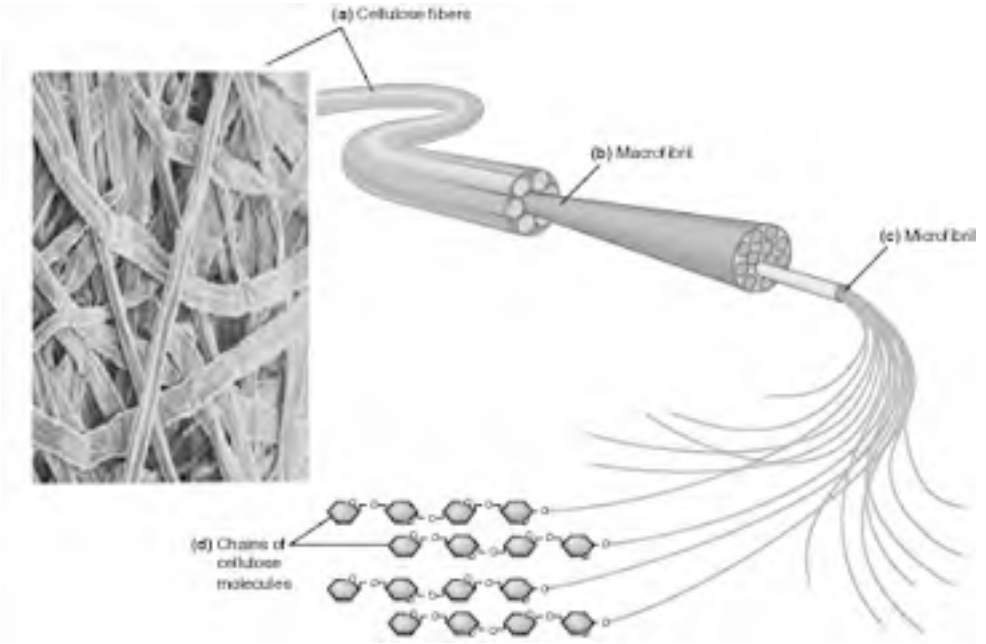

Figure 6. Stucture of cellulose. (a) Cellulose fibers from a ponderosa pine. (b) Macrofibrils compose each fiber. (c) Each macrofibril is composed of bundles of microfibrils. (d) Microfibrils, in turn, are composed of bundles of cellulose chains. Cellulose fibers can be very strong; this is one reason why wood is such a good building material.

Iron-gall ink was commonly used in ancient manuscripts that are contaminated by acids especially in the capital letters where a high amount of ink was used. A variant of iron-gall ink, widely used in Europe for a long time, contains copper salts (called metal-gall inks) and produces similar degradation mechanisms shown by iron inks. However, sulfuric acid-catalyzed hydrolysis of cellulose is not the only paper degradation pathway due to the presence of iron-gall ink. Transition metal ions usually catalyze cellulose oxidation through a free radical mechanism known as Fenton reaction which involves iron ions (in the presence of copper the reaction is called Fenton-like reaction) and hydrogen peroxide formed *in situ* according to the following relationships:

1) formation of peroxides in acidic medium:

$$Fe^{2+} + O_2 + H^+ \rightarrow Fe^{3+} + HOO\cdot$$

$$Fe^{2+} + HOO\cdot + H^+ \rightarrow Fe^{3+} + H_2O_2$$

2) homolytic decomposition of peroxides by transition metal ions:

$$Fe^{2+} + H_2O_2 \rightarrow Fe^{3+} + OH^- + OH\cdot \quad \textit{Fenton reaction}$$

$$Cu^+ + H_2O_2 \rightarrow Cu^{2+} + OH^- + OH\cdot \textit{Fenton-like reaction}$$

These processes can produce severe degradation of paper as the perforation of the inked areas or a general loss of the typical mechanical properties of paper, i.e. elasticity and tensile strength. As a consequent effect of paper degradation it is not rare to see portions of documents from 16th, 17th and 18th centuries completely corroded by inks. A deacidification treatment based on magnesium hydroxide nanoparticles in alcohol dispersion (see chapter 4) is able to preserve paper, with a single treatment, from both acid hydrolysis and oxidative ink corrosion simply controlling the final pH of deacidified paper to 6.5-7.5, opening new perspectives in the conservation of cellulose based documents and artifacts.

1.4.3 Wood preservation

The Vasa is probably the most well preserved warship recovered from the sea; in spite of its aspects, many interventions are probably still required to ensure her a long life. The Vasa sunk in Stockholm harbor during her maiden voyage on August 10, 1628, when a gust of wind caught the sails making the ship list to port and letting the water inside the open gun ports. Early attempts to raise the ship failed and after the recovering of the bronze cannons (1664-1665), the hull was left on the seabed until its salvage on 1961. After the sinking, the wetting of fresh wood of the hull began and we can assume that it took more than ten years for the brackish Baltic Sea water to fill the wood cells lumina. Together with water, salts penetrated into the Vasa; sodium, chlorine, potassium, calcium, magnesium and sulphates are the most common ions that can be found in the inner part of the Vasa wood. On the other diffusion direction, water soluble compounds migrated from the wood to the seawater. High concentrations of iron are found both in the

surface and in the inner regions of the Vasa wood. The hull components were held together by about 5500 iron bolts, of which no traces were found after the salvage; seawater corroded those bolts and the cannon balls and allowed the diffusion of iron inside the cells lumina.

Figure 7. The warship Vasa in her actual location inside the VasaMuseet.

The total amount of iron, in its two common oxidation states (II and III), inside the Vasa wood can be estimated in 5t. Also the sulfur is largely present inside the wood; in the polluted water of Stockholm's harbor the dissolved oxygen level was very low and such anoxic conditions favored the bacteria that use sulfate ions (the concentration of sulfate is about 0.3 g/l in the Baltic sea) as an oxygen source to metabolize the organic compounds. The end product of this reaction is hydrogen sulfide. Fortunately, The anoxic conditions and the high concentration of hydrogen sulfide made the environment around the Vasa inhospitable to fungi, rot and other wood degrading microorganisms. Because of the low solubility of iron sulfides, the diffusion of these two products inside the wood must have followed two independent and separated pathways. In particular, we can assume that the corrosion of iron bolts happened before the diffusion of the hydrogen sulfide inside the wood; then, it probably reacted both with iron and with lignin forming iron sulfides and reduced organic sulfur compounds.

In order to prevent the dramatic effect of dimensional changes of the waterlogged wood cells, as shrinkage or collapse, after the drying, fillers

must be used. Polyethylene glycol (PEG) is still the most diffused product in the conservation of waterlogged wood, because is an inert, water-soluble polymer with low vapor pressure and low hygroscopicity. For this reason, from 1962 to 1979, the hull of Vasa was treated with different aqueous solution of polyethylene glycol [58]. It must be underline that in fifteen year, about 400 tons of PEG have been sprayed inside the hull and that, before the treatment, none of the water soluble components, as, for example, salts, were removed. Nowadays, the Vasa is much more similar to a wax copy of the original than a real wooden warship; and, furthermore, she carries in her inside a dangerous chemical mixture that is deteriorating the structure. It is now clear that the formation of sulfates is due to the oxidation of elemental sulfur by atmospheric oxygen and that sulfuric acid and hydrogen sulfide are responsible for the low pH values of the Vasa wood. As above stated, cellulosic material are very sensitive to the acid catalyzed hydrolysis of glycosidic bonds. The scientific committee, responsible for the conservation of the Vasa, started in 2003 a cooperation with CSGI and Chemistry Department of Florence's University to study a deacidification procedure to neutralize wood acidity. Interesting results were obtained in the first years of this collaboration [59,60] and these were the starting point for new application of nanoparticles on original Vasa wooden pieces. Moreover, the role of the iron ions inside the wood, must be considered; as already stated, transition metal ions can induce cellulose oxidation through radical reactions. These degradation mechanisms are pH dependent. Once again, as in the case of metal gall inks containing paper, deacidification and antioxidant treatments are both required.

1.4.4 Stone restoration

The stones used for ornamental and covering ends suffer natural and artificial degradation, that become causes of consuming, loss of mechanic resistance, fissuration, spotting, fading, formation of crusts (efflorescence of salts) and changes in coloration. The natural degradation is related to the geologic exposure, deformation (tectonic and non tectonic) and erosion. The artificial degradation are due to mining, processing, handling, applications and use. As for coverings, the processes of degradation of the applied materials result from the action of physical, chemical and biological agents. The most important alterations occur by physical and chemical attack of the rock constituent minerals, some of the well known parameters as follows:

- The alkalies, for example, under the caustic soda form, attack silicate minerals present within granitoid and granitic rocks in general;

- Calcite and dolomite, which are carbonates and main marble constituents, suffer the attack from all the acidic solutions;

- Oligoclase, silicate of the calcium-alkaline feldspars family, and nephelinite, also a silicate of the feldspars type, is sensible to chloride acid;

- Mafic minerals (dark) are more alterable by oxidation than felsite minerals (light), and it is noticeable that the hypersthenes, mafic mineral of the pyroxenes family and constituent of the charnockits (green granites, Ubatuba type), are principally degraded by insolation which modifies the stone chromatic standard;

- Sulphides, metallic minerals that occur as accessories in marbles and granites, serpentinites and quartzites, oxidize very fast when exposed to atmospheric conditions, becoming one of the main problems for their use of covering stones.

Restoration of stones can start only after specific analysis about the problem. The most common procedures for removal of spots and other alterations, include new polishing, application of oxalic acid (solution of 10% in volume), application of oxygenated water (20 volumes), sand blasting (for non reflecting surfaces) and application of hot water and/or water value under pressure. For chips and cracks, the fulfilling with plastic mass, white cement or plaster, mixed to the powder of the affected rock, is used. However, there are some degradation phenomena such as the powdering of the surface and the formation of salts crusts for efflorescence, which are not eliminated with these common procedures. Nanoparticles of alkalin earth metal hydroxides developed by us, can solve some of these deteriorations and offer some interesting treatment simplifications (see chapter 4).

1.5 References

[1] E.P.K. Currie, M. Tilley, Hybrid nanocoatings in the display industry, Journal of the Society for Information Display. 13 (2005) 773-780.

[2] A. Chiappini, C. Armellini, A. Chiasera, M. Ferrari, R. Guider, Y. Jestin, et al., Preparation and characterization of ZnO particles embedded in organic–inorganic planar waveguide by sol–gel route, Journal of Non-Crystalline Solids. 355 (2009) 1132-1135.

[3] G. De Filpo, S. Mormile, F.P. Nicoletta, G. Chidichimo, Fast, self-supplied, all-solid photoelectrochromic film, Journal of Power Sources. 195 (2010) 4365-4369.

[4] M. Mandal, B. Das, K. Mandal, Synthesis of CoxPt1−x alloy nanoparticles of different phase by micellar technique and their properties study, Journal of Colloid and Interface Science. 335 (2009) 40-43.

[5] K. Morishige, D.F. Kacher, P. Libby, L. Josephson, P. Ganz, R. Weissleder, et al., High-Resolution Magnetic Resonance Imaging Enhanced With Superparamagnetic Nanoparticles Measures Macrophage Burden in Atherosclerosis, Circulation. 122 (2010) 1707-1715.

[6] T. Bui, J. Stevenson, J. Hoekman, S. Zhang, K. Maravilla, R.J.Y. Ho, Novel Gd Nanoparticles Enhance Vascular Contrast for High-Resolution Magnetic Resonance Imaging, PLoS ONE. 5 (2010) e13082.

[7] S. Etienne, C. Becker, D. Ruch, B. Grignard, G. Cartigny, C. Detrembleur, et al., Effects of incorporation of modified silica nanoparticles on the mechanical and thermal properties of PMMA, J Therm Anal Calorim. 87 (2007) 101-104.

[8] B. Jo, D. Banerjee, STUDY OF HIGH TEMPERATURE NANOFLUIDS USING CARBON NANOTUBES (CNT) FOR SOLAR THERMAL STORAGE APPLICATIONS, in: Es2010: Proceedings of Asme 4th International Conference on Energy Sustainability, Vol 2, AMER SOC MECHANICAL ENGINEERS, THREE PARK AVENUE, NEW YORK, NY 10016-5990 USA, 2010: pagg. 741-748.

[9] C. Choi, H. Yoo, J. Oh, Preparation and heat transfer properties of nanoparticle-in-transformer oil dispersions as advanced energy-efficient coolants, Current Applied Physics. 8 (2008) 710-712.

[10] D. Siginer, American Society of Mechanical Engineers.;American Society of Mechanical Engineers., Developments and applications of non-Newtonian flows, 1995 : presented at the 1995 ASME International Mechanical Engineering Congress and Exposition, November 12-17, 1995, San Francisco, California, American Society of Mechanical Engineers, New York, 1995.
[11] I. Garcia, J. Fransaer, J. Celis, Electrodeposition and sliding wear resistance of nickel composite coatings containing micron and submicron SiC particles, Surface and Coatings Technology. 148 (2001) 171-178.
[12] L. Settineri, M. Faga, Laboratory tests for performance evaluation of nanocomposite coatings for cutting tools, Wear. 260 (2006) 326-332.
[13] N. Dahotre, Symposium: High Temperature Coatings., Science and technology II : proceedings of a symposium held during the TMS Annual Meeting '96 in Anaheim, California, February 4-8, 1996, The Minerals Metals & Materials Society, Warrendale PA, 1996.
[14] A. Sohrabi, A. Dolati, M. Ghorbani, A. Monfared, P. Stroeve, Nanomechanical properties of functionally graded composite coatings: Electrodeposited nickel dispersions containing silicon micro- and nanoparticles, Materials Chemistry and Physics. 121 (2010) 497-505.
[15] A. Bandyopadhyay, A.K. Bhowmick, M. De Sarkar, Synthesis and characterization of acrylic rubber/silica hybrid composites prepared by sol-gel technique, J. Appl. Polym. Sci. 93 (2004) 2579-2589.
[16] A. Okada, The chemistry of polymer-clay hybrids, Materials Science and Engineering: C. 3 (1995) 109-115.
[17] L. Huang, Z. Jia, I. Kymissis, S. O'Brien, Capacitors and OFET Gate Dielectrics from Self-Assembled BaTiO and (Ba,Sr)TiO Nanocrystals in the Superparaelectric Limit, Adv. Funct. Mater. 20 (2010) 554-560.
[18] G. Pinto, A. Jiménez-Martìn, Conducting aluminum-filled nylon 6 composites, Polym. Compos. 22 (2001) 65-70.
[19] L. Flandin, J.Y. Cavaillé, G. Bidan, Y. Brechet, New nanocomposite materials made of an insulating matrix and conducting fillers: Processing and properties, Polym. Compos. 21 (2000) 165-174.
[20] D. Saunders, S. Galea, G. Deirmendjian, The development of fatigue damage around fastener holes in thick graphite/epoxy composite laminates, Composites. 24 (1993) 309-321.
[21] A. Al-Ghamdi, F. El-Tantawy, New electromagnetic wave shielding effectiveness at microwave frequency of polyvinyl chloride reinforced graphite/copper nanoparticles, Composites Part A: Applied Science and Manufacturing. 41 (2010) 1693-1701.

[22] S. Tong, C. Zhang, C. Jiang, G. Liu, Q. Ling, E. Kang, et al., Improvement in the hole collection of polymer solar cells by utilizing gold nanoparticle buffer layer, Chemical Physics Letters. 453 (2008) 73-76.
[23] A.K. Padhi, Phospho-olivines as Positive-Electrode Materials for Rechargeable Lithium Batteries, J. Electrochem. Soc. 144 (1997) 1188.
[24] K. Zaghib, A. Mauger, F. Gendron, C. Julien, J. Goodenough, Encyclopedia of Electrochemical Power Sources, Elsevier, 2009.
[25] L. Pasquini, E. Callini, E. Piscopiello, A. Montone, M.V. Antisari, E. Bonetti, Metal-hydride transformation kinetics in Mg nanoparticles, Appl. Phys. Lett. 94 (2009) 041918.
[26] P. Mani, R. Srivastava, P. Strasser, Dealloyed Pt-Cu Core-Shell Nanoparticle Electrocatalysts for Use in PEM Fuel Cell Cathodes, J. Phys. Chem. C. 112 (2008) 2770-2778.
[27] A. Sarkar, A. Manthiram, Synthesis of Pt@Cu Core−Shell Nanoparticles by Galvanic Displacement of Cu by Pt Ions and Their Application as Electrocatalysts for Oxygen Reduction Reaction in Fuel Cells, J. Phys. Chem. C. 114 (2010) 4725-4732.
[28] H.J. Wu, Q. Shuai, Z.L. Zhu, S.H. Hu, Complete Benzene Oxidation over Colloidal Gold Catalysts Supported on Nanostructure Zinc Oxide, Amr. 96 (2010) 21-27.
[29] L.L. Hench, R.J. Splinter, W.C. Allen, T.K. Greenlee, Bonding mechanisms at the interface of ceramic prosthetic materials, J. Biomed. Mater. Res. 5 (1971) 117-141.
[30] V. Edwards-Jones, The benefits of silver in hygiene, personal care and healthcare, Letters in Applied Microbiology. 49 (2009) 147-152.
[31] K. Kalishwaralal, S. BarathManiKanth, S.R.K. Pandian, V. Deepak, S. Gurunathan, Silver nanoparticles impede the biofilm formation by Pseudomonas aeruginosa and Staphylococcus epidermidis, Colloids and Surfaces B: Biointerfaces. 79 (2010) 340-344.
[32] D.W. Elliott, W. Zhang, Field Assessment of Nanoscale Bimetallic Particles for Groundwater Treatment, Environ. Sci. Technol. 35 (2001) 4922-4926.
[33] R.J. Barnes, C.J. van der Gast, O. Riba, L.E. Lehtovirta, J.I. Prosser, P.J. Dobson, et al., The impact of zero-valent iron nanoparticles on a river water bacterial community, Journal of Hazardous Materials. 184 (2010) 73-80.
[34] R. Saad, S. Thiboutot, G. Ampleman, W. Dashan, J. Hawari, Degradation of trinitroglycerin (TNG) using zero-valent iron nanoparticles/nanosilica SBA-15 composite (ZVINs/SBA-15),

Chemosphere. 81 (2010) 853-858.
[35] D. Rickerby, M. Morrison, Nanotechnology and the environment: A European perspective, Sci. Technol. Adv. Mater. 8 (2007) 19-24.
[36] R. Giorgi, M. Ambrosi, N. Toccafondi, P. Baglioni, Nanoparticles for Cultural Heritage Conservation: Calcium and Barium Hydroxide Nanoparticles for Wall Painting Consolidation, Chem. Eur. J. 16 (2010) 9374-9382.
[37] E. Carretti, M. Bonini, L. Dei, B.H. Berrie, L.V. Angelova, P. Baglioni, et al., New Frontiers in Materials Science for Art Conservation: Responsive Gels and Beyond, Acc. Chem. Res. 43 (2010) 751-760.
[38] G. Poggi, R. Giorgi, N. Toccafondi, V. Katzur, P. Baglioni, Hydroxide Nanoparticles for Deacidification and Concomitant Inhibition of Iron-Gall Ink Corrosion of Paper, Langmuir. (2010) 101129093906029.
[39] Faraday, M., Philos. Trans. R. Soc. London Ser. A. 145 (1857) 147.
[40] T. Ring, Fundamentals of ceramic powder processing and synthesis, Academic Press, San Diego, 1996.
[41] V. Privman, Mechanism of Formation of Monodispersed Colloids by Aggregation of Nanosize Precursors, Journal of Colloid and Interface Science. 213 (1999) 36-45.
[42] B.L. Cushing, V.L. Kolesnichenko, C.J. O'Connor, Recent Advances in the Liquid-Phase Syntheses of Inorganic Nanoparticles, Chem. Rev. 104 (2004) 3893-3946.
[43] B.V. Enustun, J. Turkevich, J. Am. Chem. Soc. 85 (1963) 3317-3328.
[44] C. Chinnasamy, B. Jeyadevan, O. Perales-Perez, K. Shinoda, K. Tohji, A. Kasuya, Growth dominant co-precipitation process to achieve high coercivity at room temperature in CoFe/sub 2/O/sub 4/ nanoparticles, IEEE Trans. Magn. 38 (2002) 2640-2642.
[45] K.S. Suslick, Sonochemistry, Science. 247 (1990) 1439-1445.
[46] I. Halalay, M. Balogh, Sonochemical method for producing titanium metal powder, Ultrasonics Sonochemistry. 15 (2008) 684-688.
[47] F. Zhou, Z. Wu, M. Wang, K. Chen, Structure and mechanical properties of pincers of lobster (Procambarus clarkii) and crab (Eriocheir Sinensis), Journal of the Mechanical Behavior of Biomedical Materials. 3 (2010) 454-463.
[48] M. Jose-Yacaman, L. Rendon, J. Arenas, M.C. Serra Puche, Maya Blue Paint: An Ancient Nanostructured Material, Science. 273 (1996) 223-225.
[49] C.I. Park, O.O. Park, J.G. Lim, H.J. Kim, The fabrication of syndiotactic polystyrene/organophilic clay nanocomposites and their

properties, Polymer. 42 (2001) 7465-7475.
[50] M. Alexandre, Polymer-layered silicate nanocomposites: preparation, properties and uses of a new class of materials, Materials Science and Engineering: R: Reports. 28 (2000) 1-63.
[51] P.B. Messersmith, E.P. Giannelis, Synthesis and Characterization of Layered Silicate-Epoxy Nanocomposites, Chem. Mater. 6 (1994) 1719-1725.
[52] A. Rehab, N. Salahuddin, Nanocomposite materials based on polyurethane intercalated into montmorillonite clay, Materials Science and Engineering: A. 399 (2005) 368-376.
[53] P. LeBaron, Polymer-layered silicate nanocomposites: an overview, Applied Clay Science. 15 (1999) 11-29.
[54] N. Hasegawa, M. Kawasumi, M. Kato, A. Usuki, A. Okada, Preparation and mechanical properties of polypropylene-clay hybrids using a maleic anhydride-modified polypropylene oligomer, J. Appl. Polym. Sci. 67 (1998) 87-92.
[55] F. Gao, Clay/polymer composites: the story, Materials Today. 7 (2004) 50-55.
[56] Ferroni and P. Baglioni, in: Scientific Methodologies Applied to Works of Art, Florence, 1984.
[57] C. Horie, Materials for conservation: organic consolidants, adhesives and coatings, 1° ed., Butterworths-Heinemann, Oxford [u.a.], 2006.
[58] J. Walker, Primary wood processing: principles and practice, 2° ed., Springer, Dordrecht the Netherlands, 2006.
[59] R. Giorgi, D. Chelazzi, P. Baglioni, Conservation of acid waterlogged shipwrecks: nanotechnologies for de-acidification, Appl. Phys. A. 83 (2006) 567-571.
[60] D. Chelazzi, R. Giorgi, P. Baglioni, Nanotechnology for Vasa Wood De-Acidification, Macromol. Symp. 238 (2006) 30-36.

Chapter 2 – Methods and Instruments

2.1 SAXS and WAXS measurements

SAXS measurements were carried out with a HECUS SWAX-camera (Kratky) equipped with a position-sensitive detector (OED 50M) containing 1024 channels of width 54 μm. Cu K_α radiation of wavelength 1.542 Å was provided by a Seifert ID-3003 X-ray generator (sealed-tube type), operating at a maximum power of 2 kW. A 10-μm thick nickel filter was used to remove the CuK_β radiation. The sample-to-detector distance was 281 mm. The scattering path between the sample and the detector was kept under vacuum (P < 1 mBar) during the measurements to minimize scattering from the air. The Kratky camera was calibrated using silver behenate, which is known to have a well defined lamellar structure (d = 58.48 Å) [1]. Scattering curves were recorded in a Q-range, $Q=4\pi \sin\theta/\lambda$, between 0.01 and 0.55 $Å^{-1}$. The liquid samples were filled into 1 mm quartz capillary using a syringe. Measurements were done at 25 °C, controlled by a Peltier element, with an accuracy of ±0.1 °C. All scattering curves (slit smeared data) were corrected for the cell contribution (capillary) containing the correspondent solvent. Data were iteratively desmeared using the procedure reported by Lake [2]. In the case of a monodisperse system constituted by spherical and homogeneous particles with radius R, electron density ρ and scattering vector, Q, smaller than the reciprocal value of the particles' radius, F(Q,R) can be approximated by the Guinier formula:

$$F(Q,R) = \exp\left(-\frac{Q^2R_g^2}{3}\right)$$

where R_g is the radius of gyration, which, for spherical particles, is defined as:

$$R_g^2 = \frac{3}{5}R^2$$

However most cases of examined colloidal suspensions consist of polydisperse particles, so that the measured scattering intensity represents the sum of the scattering intensities of spherical particles with different size, as shown in the following equation:

$$I(Q) = \left(\frac{4\pi}{3}\right)^2 N_0 \Delta\rho^2 \int_0^\infty f(R) R^6 F^2(QR) dR$$

SAXS profiles were fitted with a polydisperse Schulz sphere model. This includes an asymmetric size distribution and the polydispersity P is calculated from the half width at half height (HWHH).
The (normalized) Schulz distribution is given by:

$$f(R) = (z+1)^{z+1} x^z \frac{\exp[-(z+1)x]}{R_{avg}\Gamma(z+1)}$$

where R_{avg} is the mean radius, $x = R/R_{avg}$, z is related to the polydispersity, $P = \sigma/R_{avg}$, by $z = 1/P^2 - 1$; σ^2 is the variance of the distribution.
When the polydispersity was too high and two size populations were present, a model composed of the sum of two Schulz sphere functions was used.
Small angle X-ray scattering analysis on concentrated and diluted samples was performed; the effects of the concentration on the structure factor as well as on the form factor was investigated.

2.2 Dynamic light scattering

DLS analysis was performed by a Plus90 nanoparticles size analyzer of Brookhaven Instruments Corporation, equipped with a Peltier temperature

control system. The temperature was 25 °C and the solvents were filtered immediately before dilution. The cuvette was put into sample case and allowed a 10 minutes temperature equilibration, after which the DLS measurement was promptly started. Data analyses were performed using BIC software, which converted autocorrelation functions into size distributions. For each measurement, the intensity weighted effective diameter, the relative particle size distribution and the polydispersity index were determined. The refractive index and viscosity for each solvent were introduced manually in the BIC software.
The DLS method correlates the fluctuations of scattered light intensity over time with the size of particles in suspension. The quantity measured is the translational diffusion coefficient *D*, which defines the apparent particle diameter *d* by means of Stokes-Einstein equation:

$$D = \frac{k_b T}{3\pi\eta(T)d}$$

where k_bT is the thermal energy and $\eta(T)$ is viscosity. To avoid secondary scattering, each dispersion was diluted to very low concentration, typically in the range of 1mg/L.

2.3 Carbonatation kinetics

Hydroxide carbonatation kinetics were followed by FTIR using a Thermo Nicolet Nexus 870 instrument. A drop of dispersion was put onto a horizontal KBr pellet and analyzed, after drying, by transmission infrared spectroscopy. For every spectrum, the peak area was calculated after subtraction of the baseline passing through 1554 and 1168 cm^{-1},. Spectra were collected every 5 s, with an acquisition time of 4 s, until an asymptotic value of the peak area of carbonate is reach.

2.4 Mechanical properties

The pellets of thermoplastic polymer were melted at 220°C and injected at 800 bar: ISO/R 527 standardised samples for tensile tests were obtained. A MTS Insight Electromechanical Testing Systems was used with an elongation extensometer to estimate Young's modulus *E*. The starting elongation speed was 1 mm/min but, after an elongation of 7.5%, the speed was increased to 50mm/min. In fact, nylon-6 and its composites have a high elongation capability (300 ÷ 400%) so it is necessary to speed up the process in order to reduce measurement times.

2.5 Transmission electron microscopy

TEM specimens were prepared by cryoultramicrotomy of the nanocomposite as it is, i.e. with no embedding. Slices with a nominal thickness of 50 nm were obtained.
TEM observations were carried out with a JEOL JEM-3010 operated at 300 kV. In order to keep the specimen stable under such an enegetic beam a cryogenic holder was used, cooled with liquid nitrogen. The nature of nanoparticles dispersed into the polymer matrix was ascertained with EDS measurements, carried out with an Oxford Instruments Link ISIS series 300 spectrometer.

2.6 Thermal conductivity measurement

Thermal conductivity measurements were performed with a low-power dilution refrigerator (17μW a 100mK) in the 100mK-4K temperature range [3], and with a pulse-tube cooler from 4 up to 35K. The thermometry was different in two cases: we employed a calibrated ruthenium bioxide resistor at low temperature and CERNOX thermometer over 4K. To supply thermal power we used NiCr resistance and the electrical connections to the heater and to the thermometer were made with NbTi wires to minimize power

losses. We used the integrate conductivity approach in the longitudinal flow hypothesis [4-6].

2.7 Differential scanning calorimetry

About ten milligrams of the sample were closely capped in a steel hermetic pan, and analyzed with the differential scanning calorimeter (DSC). The DSC program of this "rapid scan" was as follows: equilibration at 20 °C; ramp 5 °C/min to 250 °C. The thermal capacity was calculated with respect to the sapphire one and the melting point was obtained from the position of the melting peak.

2.8 Thermogravimetric analysis

Thermogravimetric analysis (TGA) was performed under airflow (50 $mlmin^{-1}$) using a TA instrument SDT Q600 and the temperature program was set as: 20 °$Cmin^{-1}$ from ambient to 500 °C and isotherm at 500 °C for 1h. The pure nylon-6 pyrolized and its weight decreased to 0%. In this way, the filler concentration of a composite of nylon-6 was obtained by means of the weight of the remains.

2.9 References

[1] T.N. Blanton, C.L. Barnes, M. Lelental, Preparation of silver behenate coatings to provide low- to mid-angle diffraction calibration, J Appl Crystallogr. 33 (2000) 172-173.
[2] J.A. Lake, An iterative method of slit-correcting small angle X-ray data, Acta Cryst. 23 (1967) 191-194.
[3] G. Ventura, The art of cryogenics : low-temperature experimental techniques, 1° ed., Elsevier, Amsterdam ;;Boston, 2008.
[4] A.L. Woodcraft, M. Barucci, P.R. Hastings, L. Lolli, V. Martelli, L. Risegari, et al., Thermal conductivity measurements of pitch-bonded graphites at millikelvin temperatures: Finding a replacement for AGOT

graphite, Cryogenics. 49 (2009) 159-164.
[5] G. Ventura, V. Martelli, Very low temperature thermal conductivity of Kevlar 49, Cryogenics. 49 (2009) 376-377.
[6] A.L. Woodcraft, V. Martelli, G. Ventura, Thermal conductivity of ME771 glass–epoxy laminate from millikelvin temperatures to 4K, Cryogenics. 50 (2010) 52-54.

Chapter 3 - Nylon-6 nanocomposites for industrial application

Nylon-6 is a high-performance semi-crystalline polymer. The crystal structure and polymorphism of nylon-6 have been extensively investigated by various groups, and there have been a considerable number of articles published in the literature in recent years on the subject of the microstructural characterization of nylon-6 by various characterization techniques. Nylon-6 has a polymorphic structure that exhibits two major crystalline forms: a stable α form and a meso-stable γ form. A partially disordered structure of nylon-6, a β form, is also meso-stable just like the γ form.

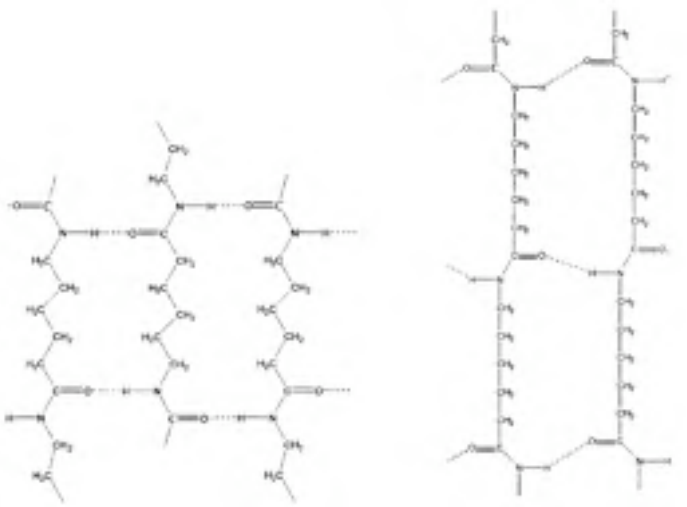

Figure 3.1. Hydrogen bonding in α- (on the left) and γ-crystalline (on the right) forms of nylon-6.

The γ form leads to improved mechanical properties and is favored by the dispersion of nanoparticles [1]. Further, nanoparticles can provide high durability for treated polymers, with respect to conventional materials,

because they possess large surface area and high surface energy that ensure better affinity for the matrix and lead to an increase in its durability.

The aim of this study is to produce organic matrix composites of nylon-6 with new or different properties from the pure polymer using nanotechnologies.

A thermoplastic composite with different thermal properties would give some benefits if compared to metal alloy, that include improved resistance to corrosion, lighter weight and the ability to adapt the conductivity properties to suit the application needs by changing the amount of filler. Both aviation and aerospace industries already use these materials, whose application in advanced technologies is increasing more and more. Although the thermal properties increase by increasing the filler concentration, we kept it low to avoid the worsening of other properties, like mechanical resistance or elasticity.

The magneto-responsive thermoplastic composites could open new frontiers in the research and development of new applications. Generally, inorganic magnetic nanoparticles are physically entrapped within or covalently immobilized to a three-dimensional cross-linked network [2,3], leading to materials with shape and size distortion that occurs reversibly and instantaneously in the presence of a non-uniform magnetic field [4,5]. In this case, the magnetophoretic force [4] conferred to the polymeric material as a result of the magnetic susceptibility of the particles has led to such materials receiving significant attention for use as soft biomimetic actuators, sensors, cancer therapy agents, artificial muscles, switches, separation media, membranes, and drug delivery systems. In uniform magnetic fields, a different phenomenon occurs. In this case, there is a lack of magnetic field–particle interactions, but particle–particle interactions arise from the creation of induced magnetic dipoles. Particle assembly within the surrounding polymer matrix can lead to dramatic transformations in material properties.

Silver nanoparticles has been used for imparting antibacterial properties [6,7], nano-TiO_2 for UV-blocking and self-cleaning properties [8-10] and ZnO nanoparticles for antibacterial and UV-blocking properties [11-13]. Inorganic UV blockers are more preferable than organic UV blockers [14,15]. In fact, zinc oxide and titanium dioxide are non-toxic and chemically stable under exposure to both high temperatures and UV.

Furthermore, nanoparticles have a large surface area-to-volume ratio that results in a significant increasing of the effectiveness in blocking UV radiation when compared to bulk materials [12]. The use of nanoparticles in the composites for the textile industry has increased rapidly. This is mainly due to the fact that conventional methods used to add different properties to fabrics often do not lead to permanent effects, and will lose their functions after laundering or wearing.

At this point we need to make a remark about the synthesis process. We can go through two different ways to obtain a composite of nylon-6 with inorganic nanoparticles: the first approach, the most used to date, consists of blending the melted polymer with nanoparticles; the second approach requires the nanoparticles to be mixed - in the form of powder or dispersed in organic solvent - with the monomer, followed by the polymerization. This method cannot be used in every situation because of the catalytic properties some substances have: the reaction between monomers could be affected by the presence of inorganic material. Moreover, the small size of nanoparticles increases this disadvantage in case there is catalytic activity because it is a typical surface property, which increases as the size decreases. Besides this drawback, this method leads to better finished product than material thermoplastic and nanoparticles blending: firstly it is not simple to disperse clusters into a polymer that normally has a high viscosity; secondly, melting must occur in strict conditions for some polymers (among which nylon-6) because just some ppms of oxigen are able to brown it; finally, it is not possible to create chemical bonds between particles and polymer chains like in the polymerization case (whenever the filler has undergone preliminary treatments which makes the surface able to link the matrix).

3.1 ZnO nanoparticles in nylon-6

Zinc oxide is widely used in different areas because of its unique photocatalytic, thermal, electrical, electronic, optical, dermatological, and antibacterial properties [16-23]. For these applications, the nanoparticles need to be dispersed homogeneously in the different matrices, and a number of new synthetic strategies have been developed in order to prevent particles agglomeration, and increase the stability of ZnO nanoparticles dispersions.

Chemical methods give the ability to produce powders with an exceptionally small size in the nanometer range [24]. Many authors already reported the production of some powders via different synthesis routes: precipitation routes [25], micelles or micro-emulsion [26], a combustion synthesis route, an adapted Pechini process [27], a carboxylate gelation method, etc.

3.1.1 Synthesis of the filler

Homogeneous precipitation

$Zn(OH)_2$ nanoparticles were synthesized by precipitation with ammonia of a zinc acetate solution. The nucleation reaction can be written as

$$Zn(CH_3CO_2)_2 + 2NH_4OH \longrightarrow Zn(OH)_2 + 2NH_4CH_3CO_2$$

For a typical synthesis, 0.5 mol of zinc acetate dihydrate was dissolved in 1 L of water under constant stirring at 90 °C. A concentrated solution of ammonia (0.5 L) was put into under constant stirring. The reaction flask was then kept at 90 °C for 1h. The resulting suspension was left to settle over night. The supernatant was removed and the precipitated was dried at 60 °C under nitrogen atmosphere. Thermal treatment of the particles at 500 °C for 3 h led to the formation of ZnO nanoparticles with a polydispersed size distribution and removed the co-product through thermal decomposition.
Although the aim is often to find a synthetic route that produces a monodispersed size distribution to improve the mechanical properties (larger particles could cause a fracture), a polydispersed one is acceptable whenever it is needed to increase other properties.
The thermal conductivity of a composite is affected by the number of particles chains that are formed into the polymeric matrix [28]. It was found that the formation of the thermal conductive chains mainly depends on the total volume of the conductive filler. The more the conductive particles, the more conductive chains can be formed. But if we can obtain more thermal conductive chains with the same particles content, i.e. get higher thermal conductivity with a lower total volume of filler, the compromise between high thermal conductivity and good processing behavior can be somewhat bypassed. In fact, when the concentration of the filler is too high, the composite becomes brittle. For this reason, we opted

for hybrid filler with nano, submicro and micro particles of zinc oxide to increase also the thermal properties of the composite.

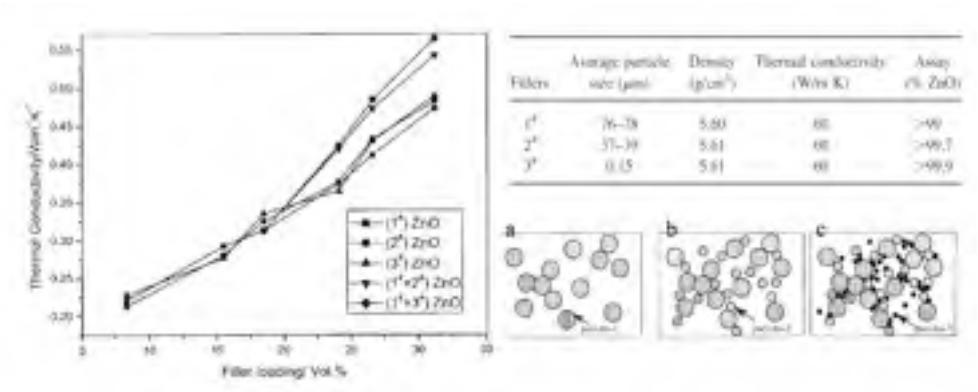

Figure 3.2. Pictures reproduced from the Qiuhong's work. On the left, thermal conductivity of silicone rubber filled with hybrid ZnO particles. On the right, the properties of the particles reported in the table above and a sketch maps of thermal conduction models below: a) single filled particles; b) two hybrid filled particles; c)three hybrid filled particles. Size: particle-1 > particle-2 > particle-3.

The synthesized particles were characterized thorugh XRD and SEM analysis.

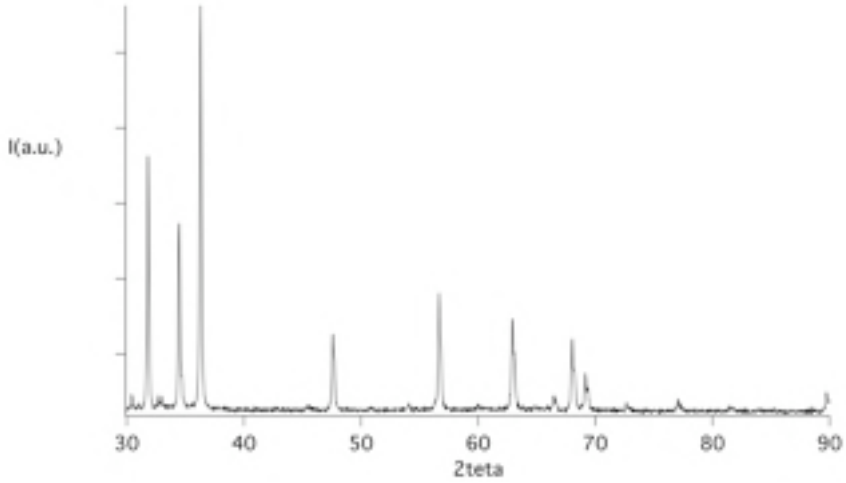

Figure 3.3. XRD profile of zinc oxide nanoparticles.

An approximate size valuation was made with the Scherrer's equation

$$D = \frac{0.94 \cdot \lambda}{B \cdot \cos\theta}$$

from which we obtained a mean diameter D of 42 nm. 0.94 is the shape factor K for a sphere, λ is the x-ray wavelength, B is the line broadening at half the maximum intensity (FWHM) in radians, and θ is the Bragg angle. D is the mean size of the ordered (crystalline) domains, which may be smaller or equal to the grain size. The Scherrer equation is limited to nano-scale particles. It is not applicable to grains larger than about 0.1 μm.

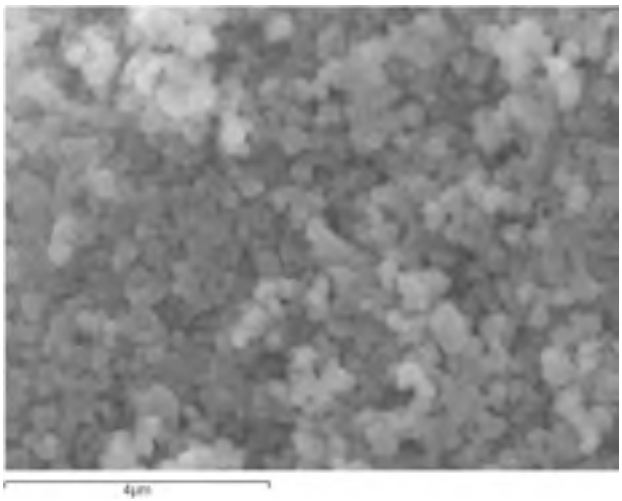

Figure 3.4. A SEM image of the clustered particles used to charge the polymer.

Although in this case our aim was to obtain a polydispersed size distribution, whenever it is needed to produce the oxide nanoparticles with a unimodal size distribution, the gelation method is suitable. In fact, precipitation during gelation is not allowed since different phases decompose at different temperatures, resulting in different particle shapes and sizes (a large size distribution is needed to improve the thermal properties, see figure 3.2). Therefore, the optimal conditions for the gelation process (pH, complexing reagents, temperature and time reaction) and the thermal treatment of the precursor are determined in order to produce nanosized ZnO particles with a well-controlled particle size and a unimodal size distribution.

Synthesis with citric acid
(The gelation method)

Zinc acetate was dissolved in water, then a hydroxy carboxylic acid (citric acid) was added in order to coordinate the metal ions present. The molar ratio of the acid to the metal concentration was 1:1. The pH of the solution was increased up to 8.5 by addition of a concentrated ammonia solution. Finally, water was added to get a start concentration of 0.5 M Zn-precursor. For gel preparation approximately 20 mL of this precursor solution was poured in a Petri dish. After solvent evaporation and further drying at 60°C, a solid precursor gel forms. The conversion of the gel into the oxidized product was carried out in a furnace by heating the samples up to 500°C, and then keeping the temperature constant for 1h under inert atmosphere [25].

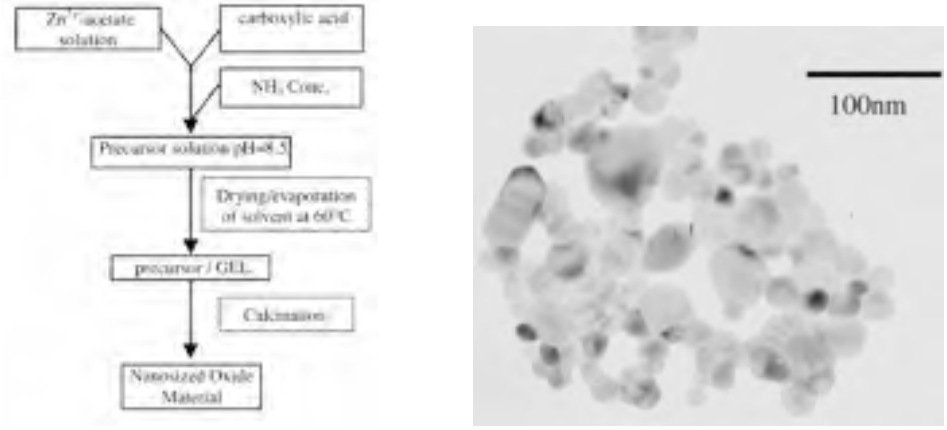

Figure 3.5. Schematic overview of the synthesis procedure on the left and TEM BF-image of ZnO nanopowder reproduced from Mondelaers's work [25].

Mondelaers et al. observed that oxide formation coincides with the breaking up of the α-C-OH bond of citric acid between 340 and 390°C, it was assumed that the α-hydroxy group was oxygen donating. During the sample calcination the organic phase was oxidized to carbon dioxide and carbon oxide and the residual ammonia was evaporated.

Synthesis with surfactant

This synthesis was based on the use of the cationic surfactant (CTAB) and simple chemical materials (zinc acetate and NH_4OH) as inorganic

precursors. The reaction was performed at room temperature. To prepare ZnO particles, the CTAB was dissolved in deionized water heating and stirring until a homogenous solution (0.08 M) was obtained. The solution of diluted NH_4OH (25 wt% solution) was then added into the cooled CTAB solution under stirring. When the mixing solution became homogenous, a solution of $Zn(CH_3CO_2)_2$ (0.40 M) was added under vigorous stirring. After stirring 4 h, the products were left at room temperature for 24 h. The resulting products were filtered, washed to remove surfactant, and then dried at 60 °C. Complete removing of the surfactant from the synthesized products was achieved through thermal treatment: 6 h at 500 °C under air flux [29].

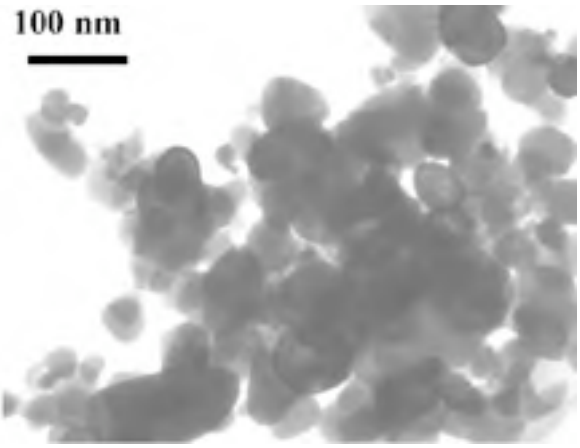

Figure 3.6. The TEM micrographs of nanocrystalline zinc oxides powders.

The advantage of this reaction is its lower temperature of exercise, but the use of surfactant causes a drastic increase of the calcination time. In fact, the powder after 3 h at 500 °C was grey because of unreacted carbonized residuals.

Synthesis with polyvinyl alcohol

PVOH, polyvinyl alcohol, (10 g, Mw 55.000) was dissolved in 200 mL of water and then $Zn(CH_3COO)_2$ (20 g) was slowly added to the solution. The resulting reaction mixture was stirred for several minutes, followed by the addition of concentrated ammonia solution. A turbid solution was formed during the stirring. After 4h, the products were left at room temperature for 24 h. The resulting products were filtered, washed to remove the polymer,

and then dried at 60 °C. Complete removal of the polymer from the synthesized products was achieved through thermal treatment: 6 h at 500 °C under air flux. This synthesis led to similar results as the one with CTAB.

3.1.2 Polymer compounding

We chose the zinc oxide powder obtained by the homogeneous synthesis in order to modify the properties of nylon-6 as much as we could. In fact, this powder was the most polydisperse and this favored a high increase of the thermal conductivity. The zinc oxide was dispersed into 200 mL of 2-propanol and heated at 60 °C for 12 hours under stirring with the goal to cover the surface of the nanoparticles with the aliphatic chains of the alcohol and to increase the interaction with the ε-caprolactam. This dispersion was mixed with melted ε-caprolactam (400g) and the 2-propanol was removed with a rotary evaporator at 40 °C under vacuum.
Melted ε-caprolactam containing the zinc oxide nanoparticles (5% w/w) was put into the vessel of a high-pressure reactor (Parr-Instruments) equipped with a mechanical stirrer. 12 mL of a 2% (w/w) acid acetic solution was added to catalyze the ring-opening polymerization. The temperature reaction was set at 260°C and the maximum pressure was ~5 bar.

t (min)	T_{set} (°C)	$T_{effective}$ (°C)	P (bar)
0	90	27	0
30	260	90	1.8
80	260	260	7.5
125	260	260	0
150	260	260	-0.4
330	0	260	0

Table 3.1. The conditions of polymerization.

After 125 minutes the pressure was reduced to allow the increase of polymeric chains length. The melted thermoplastic material was cast on a ceramic surface at room temperature. After cooling, the polymer was chopped and washed with water at reflux for 24h. Finally, the entire composite was filtered and dried at 40°C under vacuum.

3.1.3 Characterization

As reported in the work by Zheng et al. [1], the Young's moduli of the γ-phase are higher than the α-phase ones. Our samples showed an analogous behavior, as one can see in table 3.2.

	Peak Load (N)	Tensile strenght (MPa)	Elongation (%)	E modulus (MPa)
Nylon-6	389	46	355	460
Nylon-6/ZnO	389	46	264	493

Table 3.2. The mechanical properties of pure nylon-6 and of the composite with zinc oxide nanoparticles.

The mechanical properties of nylon-6 were improved also by using zinc oxide nanoparticles. We carried on a TEM study of the composite material: the material was homogeneous and this was probably due to the pre-activation of the nanoparticle surface with 2-propanol. During this step, the particle surface charge increases and the resulting electrostatic repulsion between the nanoparticles during the polymerization step leads to a more homogeneous material.

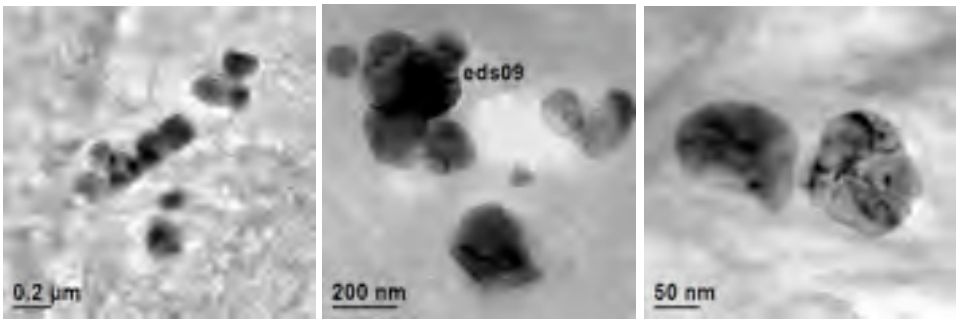

Figure 3.7. Three TEM images of the composite with zinc oxide nanoparticles.

The elected synthesis of zinc oxide nanoparticles led to a broad distribution size. We chose it in order to fill the polymer enough to modify the thermal properties other than the mechanical ones.

3.2 Cu nanoparticles in nylon-6

The copper work has roots in ancient civilizations that go back to 7000 years ago, who used it as an alternative material to stone, that it is undoubtedly difficult to work, and to clay whose fragility makes it unsuitable for any use that involves mechanical stress. In all advanced civilizations we have discovered archeological copper finds; it slowly found its way into many fields of application, becoming necessary for technology developments. During the Renaissance at the end of 1500, reducing some copper salts into pottery glazes yielded the first metal nanoparticles [30]. It was only at the end of 1970s that these were produced using other methods, but not without difficulties. The strong reactivity of the copper nanoparticles with atmospheric oxygen is well known: the high superficial area, characteristic of nanometric systems, increases the metal oxidation that rapidly turns into CuO.

We have developed a synthesis method to produce the metallic copper nanoparticles with high yield and then we have synthesized composites with 5% w/w of nanoparticles measuring thermal, mechanical properties. Scanning and transmission electron microscopy studies and small angle x-ray scattering provided structural information, and measurements of specific heat and thermal conductivity gave us insights into the thermal properties of materials.

3.2.1 Synthesis of the filler

Synthesis with sodium oleate

Aqueous solutions containing 0.2 mol of sodium oleate were left at room temperature for 2 h and then a 0.1 mol copper chloride solution was added into the oleate solution. After filtering and drying, they were transferred into a ceramic crucible. The precipitated was kept under inert atmosphere and treated by heating to 290 °C for 4 h, and then cooled at room temperature and washed with diluted (1mM) hydrochloric acid to avoid the copper hydroxide formation. This synthesis was developed by Y.H. Kim et al. [31] and led to a size distribution of 15 nm in these reaction conditions. This synthetic route is quick, easy to perform, low-cost but does not allow access to gram-scale quantities in high yield. Moreover the nanoparticles undergo oxidation, aggregation and the purity is low because of the residuals of sodium oleate.

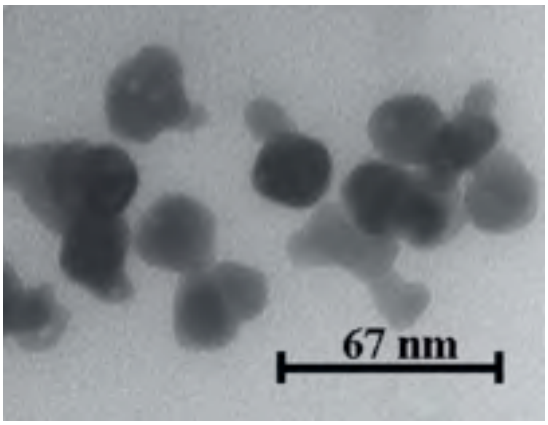

Figure 3.8. A TEM image of the copper nanoparticles produced through the synthesis of Y.H. Kim et al.

Synthesis with hydrazine

18.22 g of CTAB were added to 1 L of 0.8 M copper dichloride heated solution and put under vigorous stirring. Ammonia concentrated solution was added until the pH was above 10. In the meantime, we prepared 180 mL of an aqueous solution containing 2 moles of hydrazine and 0.01 mol of CTAB and we mixed it with the copper solution. During the copper reduction, nitrogen was released.

$$2Cu(NH_3)_2^{+2} + N_2H_4 + 4OH^- \rightarrow 2Cu + N_2 + 4NH_4OH$$

This interacted with aliphatic chains of surfactant molecules generating more than 3 L of foam per liter of copper solution (figure 3.9). An apt recovery system was developed to avoid the foam discharge. The reaction was carried out for two hours, even though the strong blue color of the copper solution disappeared in a few minutes. At the end of the reaction a brown precipitate was obtained and no foam was present. The flask was put into a glove-box with inert atmosphere. When all the precipitate was settled, we removed the liquid phase and washed 3 times with diluted hydrochloric acid. Using an acidic solution, we assured both a better removal of residual hydrazine and more reduced oxygen solubility than pure degassed water. In fact, after the first wash where a lot of hydrazine was removed, the copper nanoparticles surface was exposed and therefore highly susceptible to oxidation. Although the hydrochloric acid solution

had this advantage, its concentration was kept low to avoid etching of the copper surface.

Figure 3.9. The reaction flask during the hydrazine solution added. More than 3 L of foam were generating.

In order to make sure that the nanoparticles were not oxidized after washing, 20 mg of these were dispersed in 10 mL of degassed water and 10 mL of cyclohexane was added.

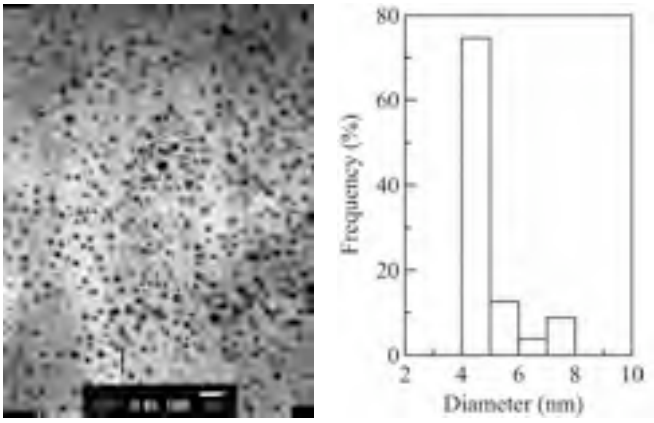

Figure 3.10. Pictures reproduced from the work of Wu and Chen [32]. Typical TEM micrograph and size distribution of Cu nanoparticles.

After sonication, all the particles remained in the aqueous phase, but the addition of 20 μL of dodecyl-1-thiol was followed by adsorption of all nanoparticles in the upper organic phase. This means that the surface of the particles was still metallic, because only the elemental copper is able to link the thiol groups with a sulfur-copper covalent bond.

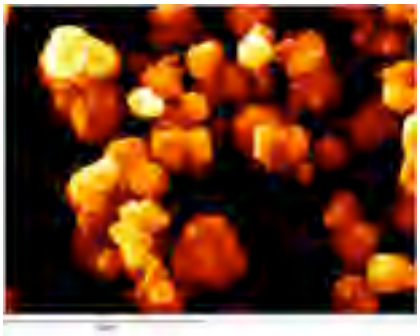

Figure 3.11. A SEM image of the metallic copper particles.

Finally, the particles were dried at 40°C under vacuum and kept under inert atmosphere. Apparently the precipitate had size distribution in the range of micrometers (fig. 3.11) but we could only see copper nanoparticle clusters the formation of which was promoted by the drying process of the precipitated.

Since CTAB is a cationic surfactant, Cu^{2+} ions would not be adsorbed on the micelles. Hence, it was suggested that Cu nanoparticles were capped by CTAB molecules after they were formed by the hydrazine. Further, since the product was present in the aqueous solution and the metal surface usually has negative charges, it could be suggested that a bilayer structure of CTAB was formed: the inner layer was linked to the Cu surface via the head groups and it was connected to the outer layer, whose head groups were in the aqueous solution, through hydrophobic interaction.

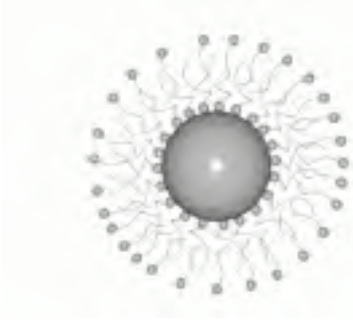

In the work of S. H. Wu [32], when CTAB concentration ranged from 0.3 mM to 0.1 M, it was found that the size of Cu nanoparticles was not significantly affected. Since the critical micellar concentration of CTAB in aqueous solution is 0.94 mM, this proved that CTAB indeed acted as a capping agent in controlling the size of Cu nanoparticles,

instead of forming micelles to limit the growth of Cu nanoparticles.

3.2.2 Characterization

Melted ε-caprolactam containing the copper nanoparticles (5% w/w) was put into the vessel of a High-Pressure Reactor (Parr-Instruments) and polymerized as reported for the preparation of zinc oxide nanocomposite.

The nanoparticles appeared well separated from each other, but not uniformly distributed: there were some regions where no particle was visible.

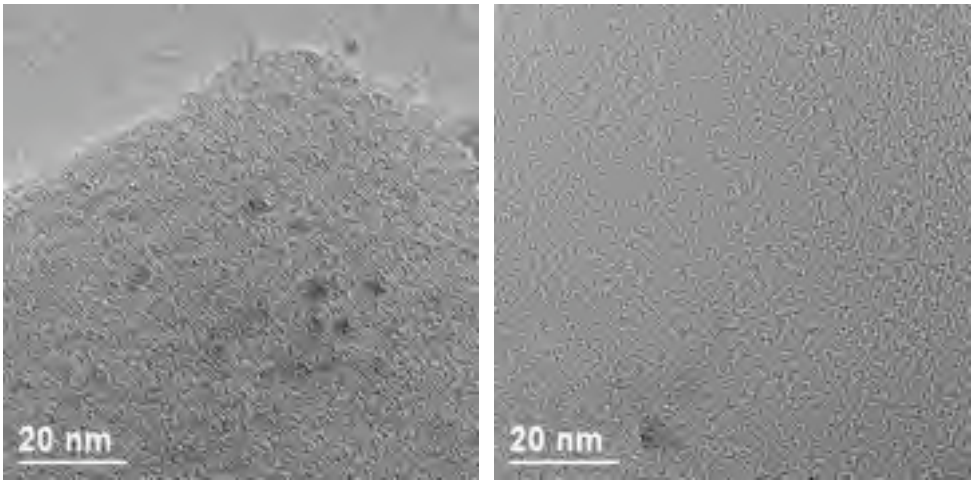

Figure 3.12. Copper/nylon-6 composite. Slices with a nominal thickness of 50 nm were observed with transmission electron microscopy.

In some cases we found particles totally isolated and from a size distribution analysis emerged that all the particles had size below 20 nm, and mainly 5 nm. The polymeric matrix gave a high contribution to the image noise, this explains the low contrast of the TEM photos. The nature of the dark spots appearing in the TEM images was established with EDS measurements, carried out with an Oxford Instruments Link ISIS series 300 spectrometer. The characteristic peak of copper appeared near these spots, confirming that these were actually copper nanoparticles.

SAXS measurements were performed on a thin film of composite. We used nylon-6 as background and fitted with sphere model [33]. We used a

contrast of 5.29×10^{-5} and obtained a radius of 3.6 nm, in agreement with TEM images.

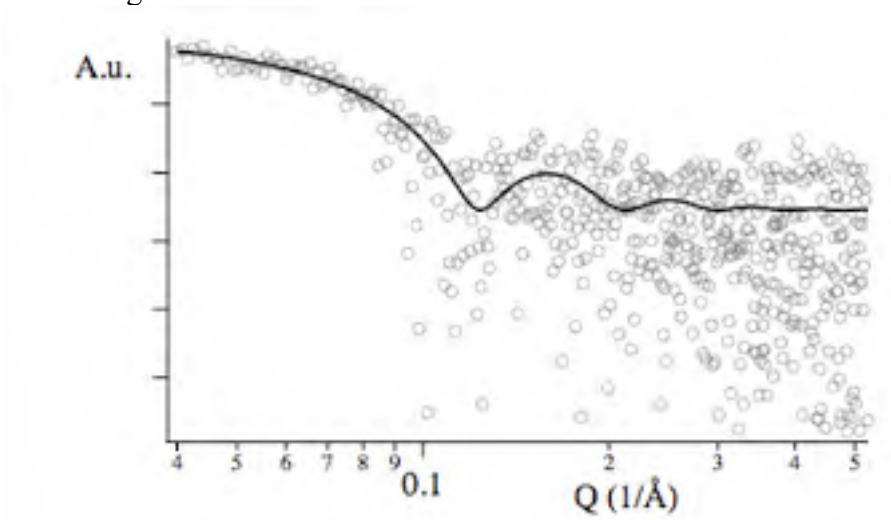

Figure 3.13. SAXS profile of Nylon-6/copper composite with the fitting.

Using the thermal capacity of sapphire as a standard we determined the one of our composite, which coincided with the theoretical thermal capacity Cp_{Th} calculated by:

$$Cp_{Th} = f_{w_1} \cdot Cp_{Ny} + f_{w_2} \cdot Cp_{Cu}$$

where f_{w1} and f_{w2} were the weight fractions of nylon-6 and copper respectively.

	Cp (36.86°C) (J/g.°C)	Cp (146.86°C) (J/g.°C)	Cp (25°C) (J/g.°C)	Cp_{Th} (25°C) (J/g.°C)
Nylon-6/Cu	1.697	2.4805	1.635	1.6827
Nylon-6	1.846	3.106	1.751	–
Copper	–	–	0.385	–

Table 3.3. Thermal capacity *Cp* ($^{J}/_{g.°C}$) at 25. 36.86 and 146.86 °C of Nylon-6 and composite. The value for copper was taken from Wikipedia [34].

A multipeak model reported in the literature [1,35] was used to fit the XRD peaks and to obtain the area under the curves, A_{α} , A_{γ} and A_{total}. Five

lorentzian functions represented the following five peaks: γ(020), α(200), β, γ(200) and α(002).

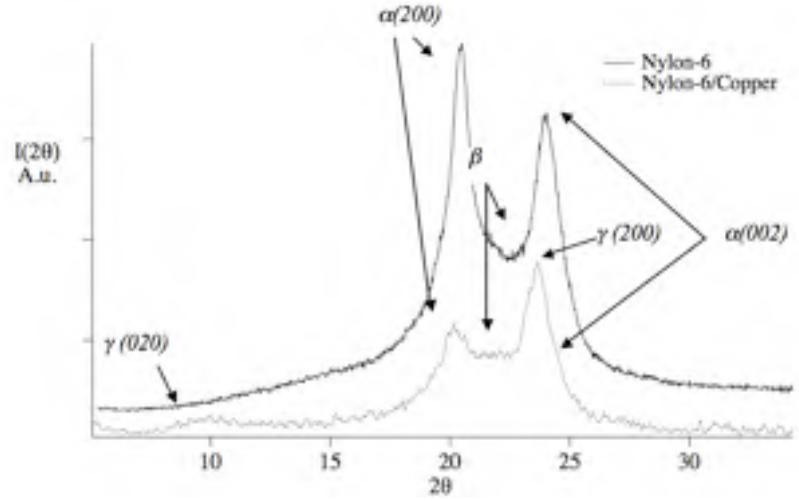

Figure 3.14. XRD spectra of nylon-6 (upper) and of the nylon-6/copper composite (lower). No peaks of γ-phase compared for nylon-6.

A_β stands for the area under the mesomorphic peak, also called the amorphous peak in other publications. This was used to calculate the relative crystallinity of the material.

$$CI_\alpha(\%) = \frac{\Sigma A_\alpha}{\Sigma(A_\alpha + A_\gamma) + A_\beta} \times 100 \quad (1)$$

$$CI_\gamma(\%) = \frac{\Sigma A_\gamma}{\Sigma(A_\alpha + A_\gamma) + A_\beta} \times 100 \quad (2)$$

$$CI_{total}(\%) = \frac{\Sigma A_\alpha + A_\gamma}{\Sigma(A_\alpha + A_\gamma) + A_\beta} \times 100 \quad (3)$$

The crystallinity index (CI) was defined as reported in the equations 1, 2, 3 (from an article by Ho and Wei [36]).

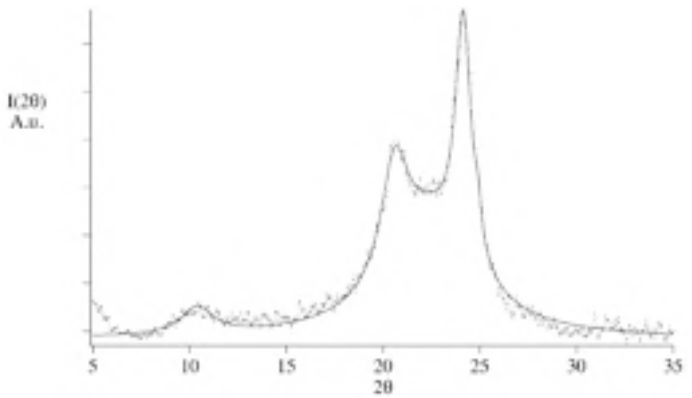

Figure 3.15. Lorentz multi-peak fitting of composite nylon-6/copper XRD spectrum. The γ-phase increased with the decreasing of α-phase: this is tipically due at the particles presence.

In table 3.4 we reported the value of CI both for nylon-6 and for nylon-6/copper composite.

	CI_{α} (%)	CI_{γ} (%)	CI_{Total} (%)
Nylon-6	54	-	54 ± 2
Nylon-6/Cu	19	29	48 ± 2

Table 3.4. The values of crystallinity index, *CI*, both for nylon-6 and for nylon-6/copper composite. CI_{α} is the amount of α-phase in the polymer, CI_{γ} of γ-phase and CI_{Total} the total crystallinity of the material.

The total crystallinity of the pure polymer was higher than the composite, but the nanoparticles induced the γ-phase, not present without them. As reported in the work by Zheng et al. [1], Young's moduli of γ-phase are higher than the α-phase ones. Our samples showed an analogous behavior, as one can see in table 3.5. The differences between their Young's moduli were lower than 5% as it was predictable by the low content of filler in the polymeric matrix. Nevertheless we chose an amount of nanoparticles that improved Young's modulus and changed thermal properties, but would leave the composite able to be spun.

	Peak Load (N)	Tensile strenght (MPa)	Elongation (%)	E modulus (MPa)
Nylon-6	389	46	355	460
Nylon-6/Cu	389	46	275	475

Table 3.5. The values of mechanical properties both for nylon-6 and for nylon-6/copper composite. The addition of nanoparticles increased the Young's modulus and reduced the percent elongation.

Thermal conductivity measurements

The thermal conductivity of the material was measured in the temperature range 400mK - 20K and its cryogenic properties were studied. This material showed an atypical behavior around 1K and 1.4K, where a sudden change in the conductivity appeared.
Low temperature thermal conductivity of pure Nylon has been measured by several authors:

- In 100-800 mK range by Anderson et al. [37];
- between 150 mK and 4 K by Scott et al. [38];
- between 1.4 K and 20 K by Reese et al. [39].

There is a substantial agreement among data of ref. [37-39]. Moreover NIST suggests a formula for the thermal conductivity of pure Nylon between 4 and 300K [40].

For the measurements below 3 K, the copper block at the bottom of the sample was screwed onto a copper sample holder in thermal contact with the mixing chamber of a conventional liquid helium cooled dilution refrigerator. A copper shield, in thermal contact with the mixing chamber of the dilution refrigerator surrounded the experiment. Power for the heater was supplied with a four NbTi wires and thermometers were electrically connected by tiny crimped Cu tubes. At the ends of the NbTi wires a four lead connection was adopted. The thermal conductivity was measured by the longitudinal steady heat flow method. A known power P was supplied to one end of the sample to establish a difference of temperature $T_1 - T_0$ along the sample. The thermal conductivity, k(T) was obtained by differentiation of the integrated power (at constant T_0)

$$P(T_1) = \frac{A}{L}\int_{T_0}^{T_1} k(T)dT$$

where A and L are the sample section and length respectively.

The measurements above 3 K were made in a cryostat based around a pulse tube cooler. The pressure in the vacuum vessel was maintained at about 10^{-4} Pa. As with the low temperature range, the thermal conductivity was measured by a steady state technique. However, instead of mounting the sample directly onto the cold head of the on a copper platform whose temperature could be controlled by a heater. The thermal conductivity was evaluated by the same method used for the low temperature range described in the previous section. There are three main contributions to the relative error in k(T):

- the power supplied to the sample: we estimate that the relative error of P is of the order of 0.1%;

- the measurement of the geometrical factor g = A/L. The error in the measurements of g is estimated to be less than 1%;

- the uncertainty in the temperature, dT, due to the accuracy of the thermometers in this temperature range. A conservative value of (dT)/T is ~2% for T > 1K and ~ 1% for T < 1K.

Taking into account these contributions, the maximum relative error in k(T) is 3%.

The measured conductivity k(T) is shown in figure 3.16. The measurements made in the two temperature ranges appear to be in good agreement.

In figure 3.16, the thermal conductivity data of pure Nylon are reported: we carried out exactly the same measurement with the Nylon-6 not filled with the Cu nanoparticles to rule out any possible error leading to the dip. Also data from ref [38] and values suggested by NIST [40] are reported for sake of comparison.

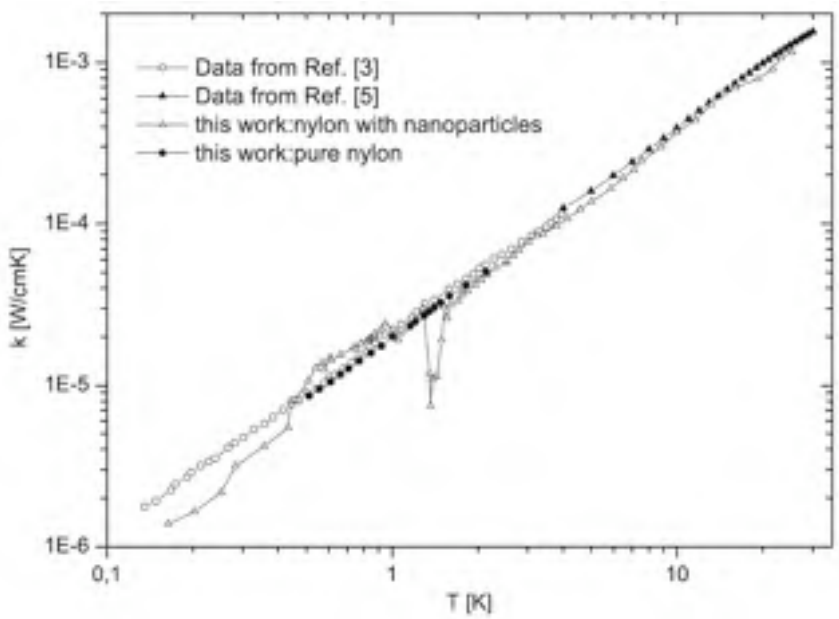

Figure 3.16. Low-temperature thermal conductivity of Nylon-6/Cu compared to pure nylon. Scott's data [38] and NIST suggested values are also reported [40].

Although nanoparticles may act as nucleation centers for the formation of additional (besides crystallinity of pure Nylon) crystalline zones, the total crystallinity compared to that of pure material is quite similar; in fact (fig. 3.16), above 4K, the two curves have the same slope (the slope should change with the degree of crystallinity). On the other hand, from figure 3.16 we immediately see that below 500 mK the material conductivity appreciably differs from that of pure Nylon. We shall now give a qualitative interpretation of this fact. We can evaluate the dimension of the inclusions, which produce additional scattering processes leading to a reduced conductivity. Using the dominant phonon wave-length [41] for Nylon at 450mK, we find that inclusion size is ~60nm, that is the size for crystallites in pure material. Therefore, since the scattering regions have the same dimensions and volume percentage of pure Nylon, this different behavior must be ascribed to the thermal contact resistance between Nylon and metallic nanoparticles: the thermal resistance is larger because it depends on the acoustic ratio between the two media [42]. The dip in thermal conductivity at ~1.4 K may be interpreted as a resonant scattering of phonons by Cu nanoparticles. We shall describe their motion using the 'elastic-string' model, that has been used also to describe the motion of

dislocations in crystals. Let us schematize nanoparticles as Cu strings, with blocked ends, in the hypothesis of only longitudinal deformation. The equation describing this vibration process is:

$$\frac{\partial^2 u}{\partial x^2} - \frac{1}{c^2} \cdot \frac{\partial^2 u}{\partial t^2} = 0$$

where u is the displacement from the equilibrium position, $c^2 = E/\rho$ with E longitudinal elastic modulus (Young modulus) and ρ is the copper density. The main frequency resonance is:

$$v_0 = \frac{1}{2L}\sqrt{\frac{E}{\rho}}$$

Where L is the string-length. In case of tangential strain the shear modulus G must be used. Of course, nanoparticles have not the shape of a string and we shall use a mean modulus M between E and G (G = E/1+v with v = Poisson ration):

$$M = \frac{E+G}{2} = \frac{E}{2} \cdot \frac{3+2v}{2(1+v)}$$

Assuming E = 120 GPa (for copper E is between 105 and 150 GPa and v = 0.34) we obtain M = 82.5 GPa. Hence we can calculate the temperature T at which phonon frequency equals nanoparticle resonant frequency:

$$T = \frac{\hbar v}{k_B} = \frac{\hbar}{2L}\sqrt{\frac{M}{\rho}}\frac{1}{k_B} = 1.44\,\mathrm{K}$$

Where L = 8nm is the peak of size distribution measured by SAXS method. Note that minimum of measured k is just at 1.4K. Even if a similar resonant scattering of phonons by crystal-dislocation has been reported for superconductors [43], the anomalous behavior like that around 1.4 K of figure 3.16 was never observed before for nanoparticles embedded in a polymer.

3.3 Core/shell copper-silica nanoparticles in nylon-6

The main difficulty for the use of Cu nanoparticles arises from their instability toward oxidation in air. Therefore, it is required to develop methods to improve the chemical stability of the particles. Different techniques have been proposed and applied to protect various metals from corrosion and, among them, coating techniques are very interesting. Various types of coatings have been tested; besides providing corrosion protection, an efficient coating should be also uniform, adhesive, flawless, and ecologically friendly. Since silanic films would seem to satisfy many of these demands, treatment with silanes to protect various metals or alloys (aluminium [44-46], copper [47,48], magnesium [49], iron [50]) from corrosion has been extensively studied. It was found that the method for direct deposition of silica on metal oxide (i.e. Cobalt ferrite) is not apt to metallic copper cores, because the metal oxide surface has a significant chemical and electrostatic affinity for silica, whereas some metals like gold, silver, iron, cobalt, copper [51], etc. have very little affinity for silica, which is the reason of the chemical mismatch between core and shell of the particles. Consequently, we used the silane coupling agents 3-mercaptopropyltrimethoxysilane (MPTS) as surface primers to modify the surfaces of the copper nanoparticles and facilitate the binding of silica.

3.3.1 Synthesis with MPTS

In a typical experiment, 25 g of Copper nanoparticles were dispersed in 400 mL anhydrous toluene containing 3 mL of MPTS at room temperature with a high-intensity ultrasonic bath. After 30 min of sonication, the suspension was obtained, which was then allowed to age for more than 6 h to ensure complete complexation of the thiol groups of MPTS with the Cu surface. The slurry (both MPTS and Cu-MPTS in an anhydrous toluene solution) was centrifuged (9000 rpm, 5 min) and washed with anhydrous ethanol. Centrifugation and washing were repeated at least three times to ensure the complete removal of the MPTS excess. Finally, the modified powder (Cu-MPTS) was dried under vacuum at 40 °C for 3 h.

The resulting core nanoparticles (modified powder, Cu-MPTS) were coated with uniform layers of silica with a method similar to a previously reported one by Stöber et al. [52]. The freshly prepared Cu-MPTS was placed into a 1 L three-necked flask with 500 mL ethanol, and then vigorously stirred for 30 min at 45 °C, and then 100 mL water and 22 mL (1.4 M) NH_4OH were

added to the above suspension. After the temperature was stabilized to 45 °C, 20 mL TEOS was rapidly injected into the reaction system and the reaction was continued. The powder was separated from the mother liquid after 4 hours and dried at 50 °C for 8 h in vacuum oven to obtain core–shell structure Cu/SiO_2 nanoparticles.

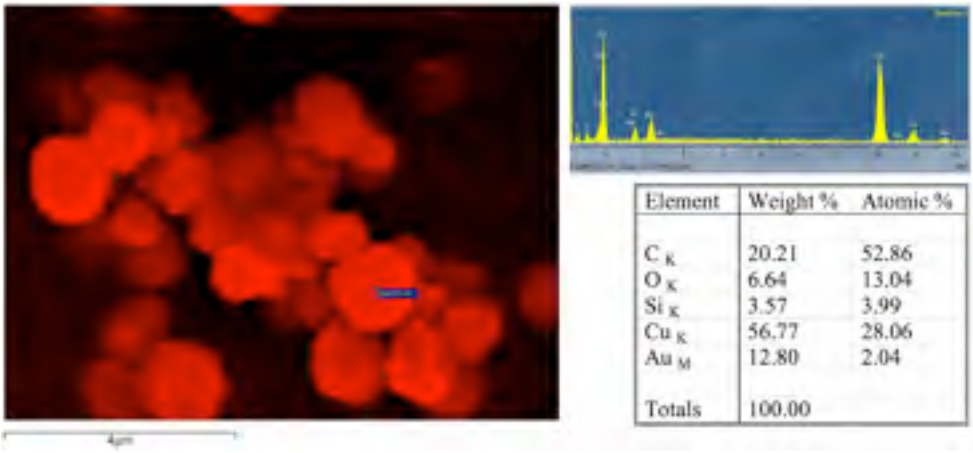

Element	Weight %	Atomic %
C K	20.21	52.86
O K	6.64	13.04
Si K	3.57	3.99
Cu K	56.77	28.06
Au M	12.80	2.04
Totals	100.00	

Figure 3.17. A SEM image of copper/silica core-shell particles. On the top right, the EDX spectrum measured in the indicated point and on the bottom left, the elements relative concentration.

Like the SEM images of the pure copper particles, the copper/silica ones were clustered and it was not possible to distinguish single nanoparticles. Figure 3.17 on the top-left shows XRD pattern of Cu nanoparticles uncoated with silica shell [53]. The pattern showed peaks at 43.6 and 74.2°, which were attributed to those of metallic Cu (JCPDS card No. 4-0836). Besides the metallic Cu peaks, several peaks, which were assigned to Cu_2O (JCPDS card No. 5-0667), were strongly detected at 36.7, 42.4 and 61.7°. This XRD result indicated that many Cu nanoparticles, which were stable in the colloid solution, were oxidized in air after sample preparation for XRD measurements by drying. Figure 3.17 shows also the XRD pattern of Cu/SiO_2 particles. The pattern showed clear peaks attributed to metallic Cu appeared at 43.3, 50.3 and 74.0° and small peaks due to Cu_2O at 36.7 and 61.7°. This XRD pattern did not change even 1 month after preparation. This indicated that the silica-coating prevented the Cu nanoparticles from being oxidized in air, as opposed to the uncoated Cu nanoparticles, which is an evidence of the protection that the silica exerts against oxidation of the Cu core.

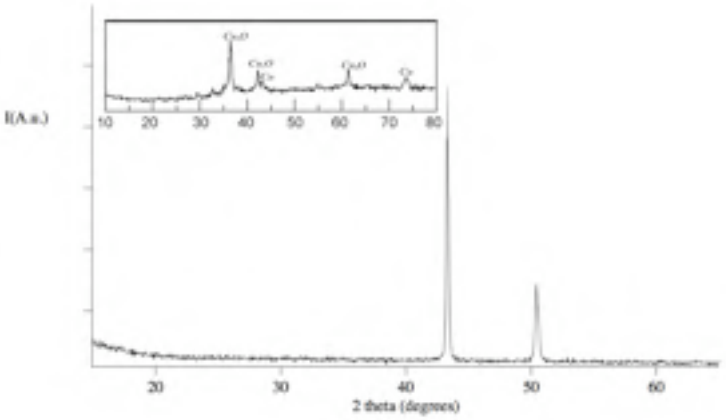

Figure 3.18. XRD patterns of Cu nanoparticles (exposed for 24h to the air) and Cu/SiO_2 particles (after one month).

Thus, quite stable Cu nanoparticles could be fabricated with silica-coating. Two possible products could have resulted from this synthetic route: separated and homogeneously dispersed nanoparticles or clusters coated by the silica layer, which could have clustered them irreversibly in micrometric aggregates.

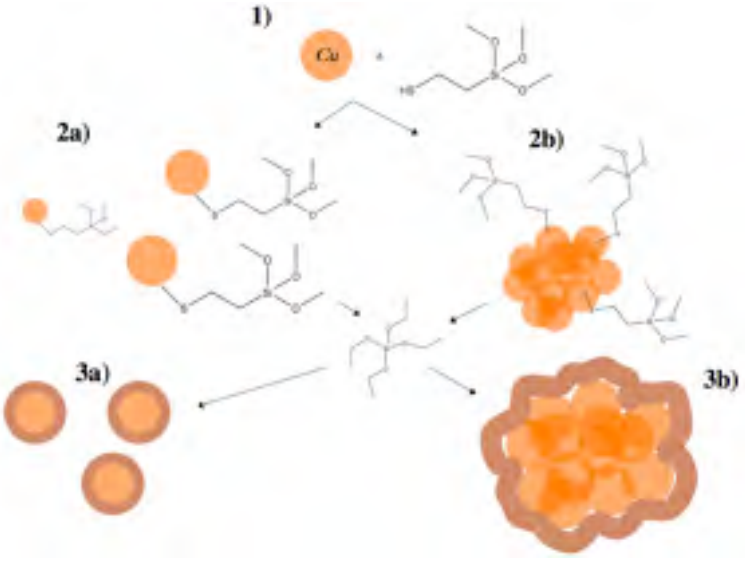

Figure 3.19. Two possible products along with each intermediate, of the coating reaction with MPTS and TEOS.

The cluster disruption, occurring during the polymerization of caprolactam, was inhibited by the silica shell surrounding the whole aggregate.

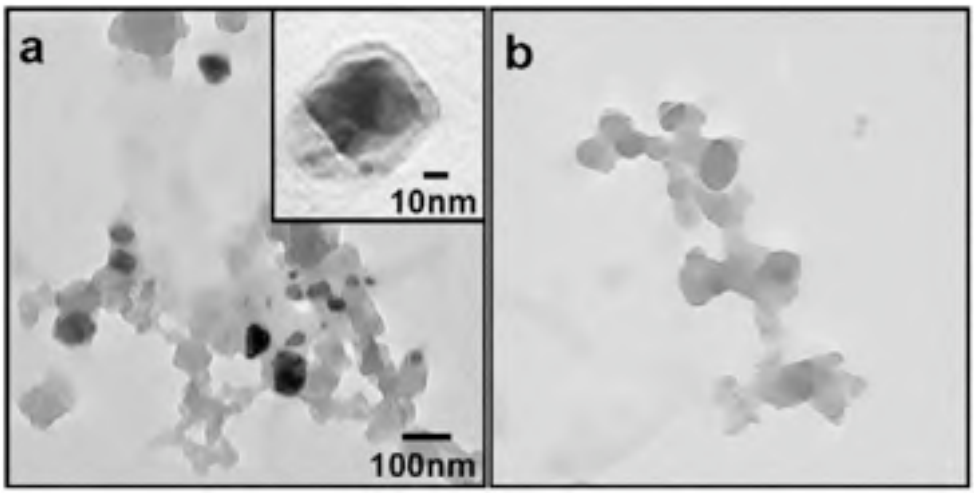

Figure 3.20. TEM images of Cu/SiO_2 particles prepared by Y. Kobayashi and T. Sakuraba [53]. Inset of the (a) shows high-magnification image of the particle.

3.3.2 Compounding

Molten ε-caprolactam containing the copper/silica core-shell nanoparticles (5% w/w) was put into the vessel of a High-Pressure Reactor (Parr-Instruments) and polymerized as reported for the preparation of zinc oxide nanocomposite.

Figure 3.21. The composite of nylon-6 containing the aggregated copper/silica core- shell particles.

In figure 3.21 we show the dramatic consequences achieved by the composite. The silica coating of the nanoparticles formed large clusters, which conferred heterogeneity to the material. We carried out some tests to find a dispersing solvent for the MPTS step more effective than toluene. We selected a few dispersing agent commonly used in colloidal chemistry. A turbidimetric measurement was performed for each one. In table 3.6 the settling times are reported.

Solvent	Settling Time (min.)
dimethyl sulfoxide	24
dichloro methane	19
ethanol	13
n-nonane	27
acetone	18
toluene	15
diethyl ether	14

Table 3.6. The settling time of the solvents used to disperse the copper nanoparticles during the MPTS coating step.

Although the n-nonane reduced the sedimentation rate (12 more minutes), the suspension was not enough dispersed and the particles kept aggregating in the coating step.

3.4 Cobalt Ferrite

Normally, any ferromagnetic material undergoes a transition to a paramagnetic state above its Curie temperature, T_C. Superparamagnetism is different from this standard transition since it occurs below the Curie temperature of the material. Superparamagnetism occurs in nanoparticles which are single-domain, i.e. composed of a single magnetic domain. This is possible when their diameter is below 3÷50 nm, depending on the material. This is what people working in the field of superparamagnetism call the “macro-spin approximation”. Because of the nanoparticle magnetic anisotropy, the magnetic moment has usually only two stable orientations antiparallel to each other, separated by an energy barrier. The stable orientations define the nanoparticle's so called “easy axis”. At finite

temperature, there is a finite probability for the magnetization to flip and reverse its direction. The mean time between two flips is called the Néel relaxation time τ_N and is given by the following Néel-Arrhenius equation:

$$\tau_N = \tau_0 \exp\left(\frac{KV}{k_B T}\right)$$

τ_N is thus the average length of time that it takes for the nanoparticle's magnetization to randomly flip as a result of thermal fluctuations; τ_0 is a length of time, characteristic of the material, called the attempt time or attempt period (its reciprocal is called the attempt frequency); its typical value is $10^{-9} \div 10^{-10}$ second; K is the nanoparticle's magnetic anisotropy energy density and V its volume. KV is therefore the energy barrier associated with the magnetization moving from its initial easy axis direction, through a "hard plane", to the other easy axis direction. This length of time can be anywhere from a few nanoseconds to years or much longer. In particular, it can be seen that the Néel relaxation time is an exponential function of the grain volume, which explains why the flipping probability becomes rapidly negligible for bulk materials or large nanoparticles. The temperature for which measurement time $\tau_m = \tau_N$ is called the blocking temperature. A transition between superparamagnetism and blocked state occurs when $\tau_m = \tau_N$.

The synthesis and organization of nanoparticles have generated considerable interest as an approach to prepare novel materials [54,55].. Magnetic assembly of dipolar colloids is an intriguing strategy for "bottom-up" materials synthesis, as the directionality of magnetic dipoles enables selective one-dimensional (1-D) organization of ferromagnetic nanoparticles. While this phenomenon has been used in the preparation of 1-D materials from iron-oxide-loaded latex particles, or emulsion droplets, similar approaches using nanoscale building blocks remain a difficult challenge. The organization of ferromagnetic nanoparticles into chains and flux-closure rings has been observed both on surfaces and in solution [56-58]. However, the use of functional dipolar nanoparticles has not been extensively investigated.

In a recent work of S. E. Bowles et al. [59] a 1-D materials was synthesized by pyrolyzing the polyacrylonitrile (PAN) coated on the surface of the ferromagnetic nanoparticles. The organization and alignment of ferromagnetic nanoparticles spanning microns in length were observed

under both zero field and field-induced assembly to form nanoparticle chains. Whenever the particles had a size large enough (e.g. 20 nm) to raise the blocking temperature over the experimental temperature, the particles had a ferromagnetic behavior. Smaller, superparamagnetic nanoparticles were undesirable for this synthetic approach, as these materials were not easily associated into long-range 1-D assemblies.

Polymers that respond to the presence or absence of magnetic fields can exist as free chains in solution, be immobilized to surfaces, or be cross-linked within networks. The majority of reports in the literature involves the latter and describes the rapid response of magneto-responsive gels swollen with complex fluids [60-62]. Generally, inorganic magnetic nanoparticles are physically entrapped within or covalently immobilized to a three-dimensional cross-linked network [2,3] leading to materials with shape and size distortion that occurs reversibly and instantaneously in the presence of a non-uniform magnetic field [5,63].
. In this case, the magnetophoretic force conferred to the polymeric material as a result of the magnetic susceptibility of the particles has led to such materials receiving significant attention for use as soft biomimetic actuators, sensors, artificial muscles, switches, separation media, membranes, and drug delivery systems [64-66].
Our goal was to produce a 3-D nanoparticles material by using a polyamidic matrix and cobalt ferrite nanoparticles. After polymerization, during the cooling of the composite, a magnetic field of 0.5 T was applied with the intent to align the magnetic dipole of the particles. Below the glass transition temperature the viscosity of the polymer increases, so if the blocking temperature of the particles is higher than the glass transition one of the nylon-6, the particles should be stuck and aligned, assuring the magnetic anisotropy of the material.

3.4.1 Massart's method

Cobalt Ferrite nanoparticles were prepared by the co-precipitation method, introducing minor modifications to the Massart's method. Briefly, aqueous solutions of 1 M $FeCl_3$ (64 mL) and $Co(NO_3)_2$ (32 mL) were added to concentrated nitric acid (2 mL). The mixture was heated to the boiling point and then, as fast as possible, mixed under vigorous agitation with 1 M NaOH solution (400 mL) warmed up till boiling. The boiling temperature and the stirring were maintained for 90 minutes. The particles obtained were separated by magnetic decantation, washed with water and added to 2

M HNO_3 (40 mL). The precipitate was again separated by magnetic decantation, dispersed in a boiling solution obtained by dissolving 0.5 M $FeCl_3$ (56 mL) and 0.5 M $Co(NO_3)_2$ (28 mL) and kept under vigorous agitation for 30 minutes. The precipitate obtained after this treatment was isolated and washed with water.

To prepare larger nanoparticles the same synthetic procedure was used, but the Co^{II}, Fe^{III}, NaOH mixture was kept to the boiling temperature during 120 minutes. For positively charged $CoFe_2O_4$ nanoparticles, the precipitate was washed with HNO_3 1 M (30 mL) and then dispersed in water.

3.4.2 Characterization

Melted ε-caprolactam containing the cobalt ferrite nanoparticles (5% w/w) was put into the vessel of a High-Pressure Reactor (Parr-Instruments) and polymerized as reported for the preparation of zinc oxide nanocomposite.

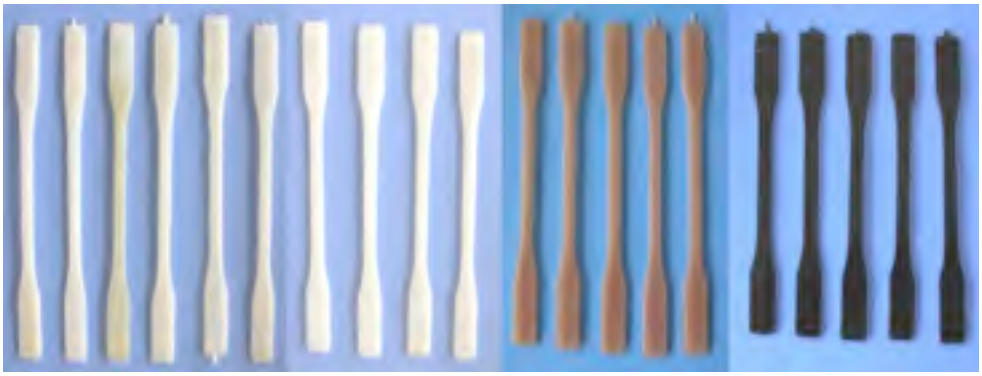

Figure 3.22. From left to right: the first six samples were made with pure nylon-6. The followed four ones were made with the zinc oxide nanocomposite and the pink others with the copper one. The last five black samples were made with the cobalt ferrite nanocomposite.

The composite was imprinted and the dumbbell-shaped specimens were used to measure the mechanical properties. The Young's module, the relative elongation and the ultimate tensile strength (shortened to tensile strength), i.e. the maximum stress that a material can withstand before necking, which is when the specimen's cross-section starts to significantly contract, were obtained and reported in table 3.7.

	Peak Load (N)	Tensile strenght (MPa)	Elongation (%)	E modulus (MPa)
Nylon-6	389	46	355	460
Nylon-6/$CoFe_2O_3$	389	46	271	489

Table 3.7. The values of mechanical properties both of nylon-6 and of nylon-6/cobalt ferrite composite. The addition of nanoparticles increased the Young's modulus and reduced the percent elongation.

The cobalt ferrite nanoparticles increased the Young's module and decreased the relative elongation of the material. We tried to produce nanoparticles large enough to assure a higher blocking temperature than the glass transition temperature of the polymer (50 °C). From a particle size analysis (of TEM images of the nanocomposite), the particle average diameter is 20 nm but to increase the blocking temperature above 323 K, the particle size must be larger.

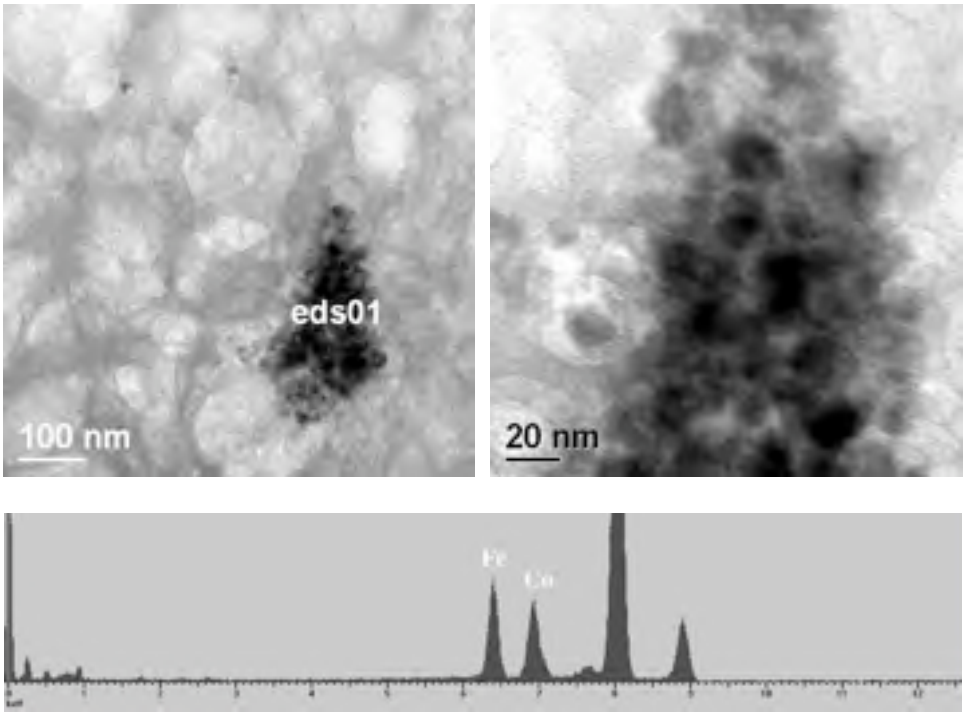

Figure 3.23. A cobalt ferrite cluster (on the top left) contained into the polymeric matrix with its magnification on the right. The EDS spectrum showed the its composition.

Therefore, the biggest difficulty was the synthesis of nanoparticles with single domain magnetic moment and average size of 40 nm.

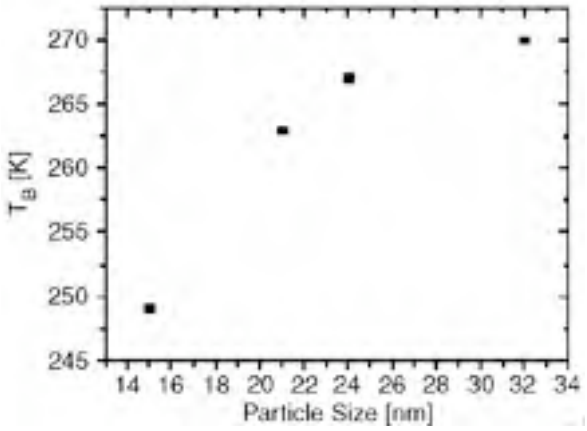

Figure 3.24. The dependence of blocking temperature (T_B) on $CoFe_2O_4$ particle size (nm). The measurements of magnetic susceptibility versus temperature for zero-field cooled (ZFC) had an applied field of 5 kOe [67].

In fact, as reported by K. Maaz [67], the blocking temperature increases above the room temperature when the nanoparticle size is higher than 40 nm, but the coercivity drastically decreases because it has a contribution from the development of domain walls in the nanoparticles.

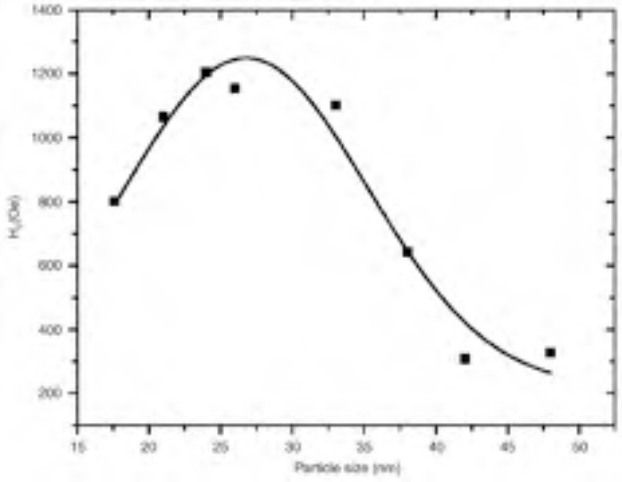

Figure 3.25. Correlation between the coercivity (H_C) and mean particle diameter (nm), at room temperature and applied field of 15 kOe [67].

Therefore, in order to magnetize the composite, the development of a novel synthetic method is needed, which would increase the particle average size but assuring a single domain. However, simply increasing the concentration of the nanoparticles in the organic matrix could have interesting effects. In fact, although the material loses its magnetization once the field is switched off, the particles chains are formed. During the solidification step, the external magnetic field could orient these chains making the material mechanically anisotropic.

3.5 References

[1] J. Zheng, R.W. Siegel, C.G. Toney, Polymer crystalline structure and morphology changes in nylon-6/ZnO nanocomposites, J. Polym. Sci. B Polym. Phys. 41 (2003) 1033-1050.

[2] D. Szabó, G. Szeghy, M. Zrínyi, Shape Transition of Magnetic Field Sensitive Polymer Gels, Macromolecules. 31 (1998) 6541-6548.

[3] D. Szabó, Magnetic and Mössbauer Studies of Magnetite-Loaded Polyvinyl Alcohol Hydrogels, Journal of Colloid and Interface Science. 221 (2000) 166-172.

[4] D. Roy, J.N. Cambre, B.S. Sumerlin, Future perspectives and recent advances in stimuli-responsive materials, Progress in Polymer Science. 35 (2010) 278-301.

[5] G. Wang, W.J. Tian, J.P. Huang, Response of Ferrogels Subjected to an AC Magnetic Field, J. Phys. Chem. B. 111 (2007) 1903-1904.

[6] N. Durán, P.D. Marcato, G.I.H. De Souza, O.L. Alves, E. Esposito, Antibacterial Effect of Silver Nanoparticles Produced by Fungal Process on Textile Fabrics and Their Effluent Treatment, Journal of Biomedical Nanotechnology. 3 (2007) 203-208.

[7] Yuan Gao, R. Cranston, Recent Advances in Antimicrobial Treatments of Textiles, Textile Research Journal. 78 (2008) 60-72.

[8] J. Xin, W. Daoud, Y. Kong, A New Approach to UV-Blocking Treatment for Cotton Fabrics, Textile Research Journal. 74 (2004) 97-100.

[9] B. Fei, Z. Deng, J.H. Xin, Y. Zhang, G. Pang, Room temperature synthesis of rutile nanorods and their applications on cloth, Nanotechnology. 17 (2006) 1927-1931.

[10] K. Qi, X. Chen, Y. Liu, J.H. Xin, C.L. Mak, W.A. Daoud, Facile preparation of anatase/SiO2 spherical nanocomposites and their

application in self-cleaning textiles, J. Mater. Chem. 17 (2007) 3504.
[11] R.H. Wang, J.H. Xin, X.M. Tao, UV-Blocking Property of Dumbbell-Shaped ZnO Crystallites on Cotton Fabrics, Inorg. Chem. 44 (2005) 3926-3930.
[12] N. Vigneshwaran, S. Kumar, A.A. Kathe, P.V. Varadarajan, V. Prasad, Functional finishing of cotton fabrics using zinc oxide–soluble starch nanocomposites, Nanotechnology. 17 (2006) 5087-5095.
[13] Baglioni P, Dei L, Fratoni L, Lo Nostro P, Moroni M, Preparation of nano- and micro-particles of group II and transition metals oxides and hydroxides and their use in the ceramic, textile and paper industries., U.S. Patent WO 2003082742, S.d.
[14] A. Riva, I.M. Algaba, M. Pepió, Action of a finishing product in the improvement of the ultraviolet protection provided by cotton fabrics. Modelisation of the effect, Cellulose. 13 (2006) 697-704.
[15] S. Scalia, R. Tursilli, A. Bianchi, P. Nostro, E. Bocci, F. Ridi, et al., Incorporation of the sunscreen agent, octyl methoxycinnamate in a cellulosic fabric grafted with β-cyclodextrin, International Journal of Pharmaceutics. 308 (2006) 155-159.
[16] M. TüRkoglu, S. Yener, Design and in vivo evaluation of ultrafine inorganic-oxide-containing-sunscreen formulations, Int J Cosmet Sci. 19 (1997) 193-201.
[17] Z.W. Pan, Nanobelts of Semiconducting Oxides, Science. 291 (2001) 1947-1949.
[18] M.S. Arnold, P. Avouris, Z.W. Pan, Z.L. Wang, Field-Effect Transistors Based on Single Semiconducting Oxide Nanobelts, J. Phys. Chem. B. 107 (2003) 659-663.
[19] J. Sawai, Quantitative evaluation of antibacterial activities of metallic oxide powders (ZnO, MgO and CaO) by conductimetric assay, Journal of Microbiological Methods. 54 (2003) 177-182.
[20] M. Xiong, G. Gu, B. You, L. Wu, Preparation and characterization of poly(styrene butylacrylate) latex/nano-ZnO nanocomposites, J. Appl. Polym. Sci. 90 (2003) 1923-1931.
[21] M. Behnajady, N. Modirshahla, R. Hamzavi, Kinetic study on photocatalytic degradation of C.I. Acid Yellow 23 by ZnO photocatalyst, Journal of Hazardous Materials. 133 (2006) 226-232.
[22] Y. Li, S. Fu, Y. Mai, Preparation and characterization of transparent ZnO/epoxy nanocomposites with high-UV shielding efficiency, Polymer. 47 (2006) 2127-2132.
[23] E. Tang, G. Cheng, X. Ma, Preparation of nano-ZnO/PMMA composite particles via grafting of the copolymer onto the surface of

zinc oxide nanoparticles, Powder Technology. 161 (2006) 209-214.
[24] D. Segal, Chemical synthesis of ceramic materials, J. Mater. Chem. 7 (1997) 1297-1305.
[25] D. Mondelaers, Synthesis of ZnO nanopowder via an aqueous acetate–citrate gelation method, Materials Research Bulletin. 37 (2002) 901-914.
[26] L. Chu, G. Hsiue, I. Lin, Ultra-Fine Ba2Ti9O20 Powders Synthesized by Inverse Microemulsion Processing and their Microwave Dielectric Properties, J American Ceramic Society. 88 (2005) 3405-3411.
[27] M. Thompson, G. Wiseman, Synthesis and microstructure of gel-derived varistor precursor powders, Ceramics International. 15 (1989) 281-288.
[28] Q. Mu, S. Feng, G. Diao, Thermal conductivity of silicone rubber filled with ZnO, Polym. Compos. 28 (2007) 125-130.
[29] Y. Wang, C. Ma, X. Sun, H. Li, Preparation of nanocrystalline metal oxide powders with the surfactant-mediated method, Inorganic Chemistry Communications. 5 (2002) 751-755.
[30] S. Padovani, C. Sada, P. Mazzoldi, B. Brunetti, I. Borgia, A. Sgamellotti, et al., Copper in glazes of Renaissance luster pottery: Nanoparticles, ions, and local environment, J. Appl. Phys. 93 (2003) 10058.
[31] Y.H. Kim, D.K. Lee, B.G. Jo, J.H. Jeong, Y.S. Kang, Synthesis of oleate capped Cu nanoparticles by thermal decomposition, Colloids and Surfaces A: Physicochemical and Engineering Aspects. 284-285 (2006) 364-368.
[32] S. Wu, D. Chen, Synthesis of high-concentration Cu nanoparticles in aqueous CTAB solutions, Journal of Colloid and Interface Science. 273 (2004) 165-169.
[33] S. Cotts, J. Compton, D. Kranbuehl, E. Espuche, L. David, G. Boiteux, In-Situ Formation of Silver Nanoparticles in PEI, Macromol. Symp. 286 (2009) 164-171.
[34] Copper - Wikipedia, the free encyclopedia, (S.d.).
[35] E. Martuscelli, F. Riva, C. Sellitti, C. Silvestre, Crystallization, morphology, structure and thermal behaviour of nylon-6/rubber blends, Polymer. 26 (1985) 270-282.
[36] J. Janicki, Time-resolved small-angle X-ray scattering and wide-angle X-ray diffraction studies on the nanostructure of melt-processable molecular composites, J Appl Crystallogr. 36 (2003) 986-990.
[37] A.C. Anderson, W. Reese, J.C. Wheatley, Thermal Conductivity of Some Amorphous Dielectric Solids Below 1°K, Rev. Sci. Instrum. 34

(1963) 1386.
[38] T.A. Scott, Low-temperature thermal properties of nylon and polyethylene, J. Appl. Phys. 44 (1973) 1212.
[39] W. Reese, J.E. Tucker, Thermal Conductivity and Specific Heat of Some Polymers between 4.5° and 1°K, J. Chem. Phys. 43 (1965) 105.
[40] E.D. Marquardt, J.P. Le, and R. Radebaugh, Cryogenic Material Properties Database, in: Keystone, Co, 2000.
[41] V. Martelli, N. Toccafondi, G. Ventura, Low-temperature thermal conductivity of Nylon-6/Cu nanoparticles, Physica B: Condensed Matter. 405 (2010) 4247-4249.
[42] R. Syme, The thermoelectric effect in silicon on sapphire inversion layers, Superlattices and Microstructures. 5 (1989) 103-107.
[43] S. O'Hara, A. Anderson, Scattering of thermal phonons by dislocations in superconducting lead and tantalum, Phys. Rev. B. 10 (1974) 574-579.
[44] J.S. Gandhi, W.J. van Ooij, Improved Corrosion Protection of Aluminum Alloys by Electrodeposited Silanes, Journal of Materials Engineering and Performance. 13 (2004) 475-480.
[45] W. Trabelsi, P. Cecilio, M. Ferreira, M. Montemor, Electrochemical assessment of the self-healing properties of Ce-doped silane solutions for the pre-treatment of galvanised steel substrates, Progress in Organic Coatings. 54 (2005) 276-284.
[46] L.E.M. Palomino, Z. Pászti, I.V. Aoki, H.G.D. Melo, Comparative investigation of the adhesion of Ce conversion layers and silane layers to a AA 2024-T3 substrate through mechanical and electrochemical tests, Mat. Res. 10 (2007).
[47] J. Shim, Copper corrosion in potable water distribution systems: influence of copper products on the corrosion behavior, Materials Letters. 58 (2004) 2002-2006.
[48] E. Hoque, J.A. DeRose, P. Hoffmann, H.J. Mathieu, Robust perfluorosilanized copper surfaces, Surf. Interface Anal. 38 (2006) 62-68.
[49] F. Zucchi, A. Frignani, V. Grassi, A. Balbo, G. Trabanelli, Organo-silane coatings for AZ31 magnesium alloy corrosion protection, Materials Chemistry and Physics. 110 (2008) 263-268.
[50] S. Kannan, The role of dihydroxybenzenes and oxygen on the corrosion of steel in black liquor, Corrosion Science. 38 (1996) 1051-1069.
[51] S. Palacin, C. Bureau, J. Charlier, G. Deniau, B. Mouanda, P. Viel, Molecule-to-Metal Bonds: Electrografting Polymers on Conducting

Surfaces, ChemPhysChem. 5 (2004) 1468-1481.
[52] W. Stöber, A. Fink, A. Bohm, J. Colloid Interface Sci. 26 (1967) 62.
[53] Y. Kobayashi, T. Sakuraba, Silica-coating of metallic copper nanoparticles in aqueous solution, Colloids and Surfaces A: Physicochemical and Engineering Aspects. 317 (2008) 756-759.
[54] F.X. Redl, K. Cho, C.B. Murray, S. O'Brien, Three-dimensional binary superlattices of magnetic nanocrystals and semiconductor quantum dots, Nature. 423 (2003) 968-971.
[55] G.A. DeVries, M. Brunnbauer, Y. Hu, A.M. Jackson, B. Long, B.T. Neltner, et al., Divalent Metal Nanoparticles, Science. 315 (2007) 358-361.
[56] V.F. Puntes, Colloidal Nanocrystal Shape and Size Control: The Case of Cobalt, Science. 291 (2001) 2115-2117.
[57] P.Y. Keng, I. Shim, B.D. Korth, J.F. Douglas, J. Pyun, Synthesis and Self-Assembly of Polymer-Coated Ferromagnetic Nanoparticles, ACS Nano. 1 (2007) 279-292.
[58] M. Klokkenburg, C. Vonk, E.M. Claesson, J.D. Meeldijk, B.H. Erné, A.P. Philipse, Direct Imaging of Zero-Field Dipolar Structures in Colloidal Dispersions of Synthetic Magnetite, J. Am. Chem. Soc. 126 (2004) 16706-16707.
[59] S.E. Bowles, W. Wu, T. Kowalewski, M.C. Schalnat, R.J. Davis, J.E. Pemberton, et al., Magnetic Assembly and Pyrolysis of Functional Ferromagnetic Colloids into One-Dimensional Carbon Nanostructures, J. Am. Chem. Soc. 129 (2007) 8694-8695.
[60] M. Zrínyi, Kinetics of the shape change of magnetic field sensitive polymer gels, Polymer Gels and Networks. 6 (1998) 441-454.
[61] M. Zrinyi, Intelligent polymer gels controlled by magnetic fields, Colloid and Polymer Science. 278 (2000) 98-103.
[62] G. Filipcsei, I. Csetneki, A. Szilagyi, M. Zrinyi, Magnetic field-responsive smart polymer composites, in: Oligomers Polymer Composties Molecular Imprinting, SPRINGER-VERLAG BERLIN, HEIDELBERGER PLATZ 3, D-14197 BERLIN, GERMANY, 2007: pagg. 137-189.
[63] M. Zŕinyi, L. Barsi, D. Szabó, H. Kilian, Direct observation of abrupt shape transition in ferrogels induced by nonuniform magnetic field, J. Chem. Phys. 106 (1997) 5685.
[64] M. Babincová, D. Leszczynska, P. Sourivong, P. Čičmanec, P. Babinec, Superparamagnetic gel as a novel material for electromagnetically induced hyperthermia, Journal of Magnetism and Magnetic Materials. 225 (2001) 109-112.

[65] S. Starodoubtsev, Poly(acrylamide) gels with embedded magnetite nanoparticles, Microelectronic Engineering. 69 (2003) 324-329.
[66] M.K. Sewell, K.D. Fugit, I. Ankareddi, C. Zhang, M.L. Hampel, D. Kim, et al., PMSE 391-Magnetothermally-triggered drug delivery using hydrogels with imbedded cobalt ferrite, iron platinum or manganese ferrite nanoparticles, Abstracts of Papers of the American Chemical Society. 235 (2008).
[67] K. Maaz, A. Mumtaz, S. Hasanain, A. Ceylan, Synthesis and magnetic properties of cobalt ferrite (CoFe2O4) nanoparticles prepared by wet chemical route, Journal of Magnetism and Magnetic Materials. 308 (2007) 289-295.

Chapter 4 - Alkaline earth metal hydroxides nanoparticles for cultural heritage preservation

4.1 Synthesis techniques

Sol-gel processing is a wet chemical synthesis approach that can be used to generate nanoparticles by gelation, precipitation, and hydrothermal treatment. The size distribution of metal, metal oxide and metal hydroxide nanoparticles can be adjusted by either chemical or heat treatment. A better control of their size and stability can be achieved through the use of inverted micelles, microemulsions and polymer matrix architecture based polymers.

Additional nanoparticle synthesis techniques include sonochemical processing, cavitation processing, microemulsion processing, and high-energy milling. The latter, the only top-down approach for nanoparticles synthesis, has been used for the generation of magnetic, catalytic, and structural nanoparticles. This technique, although already commercially available, it is considered "dirty" because of contamination problems from the milling process. Other common drawbacks include low surface area, high polydispersity, and the formation of a partially amorphous state of the as-prepared powders. Nevertheless, in some cases this approach is the only way to obtain a reasonable amount of nanoparticles.

The synthesis of moderately water soluble hydroxides (e.g. strontium and barium) with a sol-gel processing (i.e. microemulsions or precipitation) is extremely challenging. The high concentration necessary to reach supersaturation causes a remarkable decrease of reaction yield and increases the ionic strength to the extent that the w/o microemulsions may become unstable. Further problems arise with the synthesis of hydroxide nanoparticles because a high pH can lead to the hydrolysis of the surfactant and (again) destabilization of the w/o microemulsion or the reverse micelle system. For the above mentioned reasons, we chose to follow a top-down

approach to obtain these moderately water soluble inorganic nanomaterials. Magnesium and calcium hydroxide instead have a water solubility of 1.2 and 180 mg/L, respectively; this allowed us to synthesize them also through precipitation.

4.1.1 Magnesium hydroxide

Magnesium oxide hydration

We put 10 g of magnesium oxide in a mortar and we added 40 mL of water stirring with a pestle. The same reaction was carried on both with 40 mL of a 1M solution of potassium hydroxide and with 40 mL of a 1M solution of potassium nitrate. The sample formed a white paste when mixed with water, and even though the reaction was rather slow it displayed a similar behavior to the slaking of calcium oxide. The sample with caustic potassa led to a less viscous, light yellow suspension. Both precipitates were purified using dialysis tube. We kept the tube under a flow of 5 mL/s deionized water for 2 days, to bring the concentration of potassium salts below 10^{-6} M. The reaction with water was performed at 170°C. The grade of reaction was analyzed with a differential scanning calorimeter (*DSC*). The sample was then brought at high temperature to spot possible residues of oxide.

Homogeneous precipitation

350 mL of NaOH solution (4 M) and 1 L of $MgCl_2$ solution (1 M) were separately heated at 90 °C. Keeping a high temperature during the synthesis of nanoparticles leads in fact to smaller-sized particles, as showed by T.F. Tadros *et al.* in *solid/liquid dispersions* [1]. At the desired temperature, the two solutions were rapidly mixed under stirring while the temperature of the mixture was kept within ±1°C. We synthesized the nanoparticles both keeping the molar ratio between Mg^{2+} and OH^- in the reaction (x) at the stoichiometric value (0.5), and increasing at 0.7 to raise the surface charge of the particles. As a consequence, we kept the solution under stirring for 2h in order to peptize the precipitated particles. The $Mg(OH)_2$ suspension was allowed to gradually reach room temperature, and it was then purified in a 80cm dialysis tube. We kept the tube under a flow of 5 mL/s of deionized water for 2 days to reduce NaCl concentration below 10^{-6} M. The complete removal of NaCl from the suspension was checked with $AgNO_3$ tests. The suspension was centrifuged and a part of the precipitate from cation-excess synthesis was dried in vacuum at 50 °C. All the following measurements

were carried out both on this powder and on the precipitate, according to different procedures that shall be illustrated in the next sections.

4.1.2 Calcium hydroxide

The slaking of lime

We put 50 g of calcium oxide (*quicklime*) in a mortar and we added 100 ml of water stirring with a pestle. The same reaction was made both with 100 ml of a 1M solution of potassium hydroxide and with 100 ml of a 1M solution of potassium nitrate. The sample with caustic potassa led to a less viscous, light yellow suspension. No significant differences were noticed between the sample with nitrate and the one with water: both led to a white paste, called *slaked lime*.
The grade of reaction was analyzed with a differential scanning calorimeter (*DSC*). The sample was then brought at high temperature to spot possible residues of oxide.
The solution properties of the calcium hydroxide particles were studied by dynamic light scattering. The samples were diluted with 2-propanol to disperse the agglomerated particles and sonicated for 10 minutes for the same purpose.

Homogeneous precipitation

100 mL of 2M NaOH solution and 100 mL of 1M CaCl2 solution were separately heated at 90 °C. At the desired temperature, the two solutions were rapidly mixed under stirring while the temperature of the mixture was kept within ±1°C. The supersaturation degree, defined as the ratio $[Ca^{2+}]/[Ca^{2+}]_{sat}$ where $[Ca^{2+}]_{sat}$ is the concentration of Ca^{2+} cations in the $Ca(OH)_2$ saturated solution, was kept in the range 2-10. The $Ca(OH)_2$ suspension was allowed to gradually reach room temperature and then the remaining suspension was purified using a 80 cm dialysis tube. We kept the tube under a flow of 5 mL/s of deionized water for 2 days to reduce NaCl concentration below 10^{-6} M. The complete removal of NaCl from the suspension was checked with $AgNO_3$ tests. The suspension was dried in vacuum at 40 °C and the powder was dispersed in 2-propanol.

4.1.3 Strontium hydroxide

Homogeneous precipitation

Strontium is the alkaline earth metal with the highest atomic number between the chemical elements for which it is possible to obtain the hydroxide with this method. Strontium hydroxide is quite water soluble (17.7 g/L) [2] and to synthesize just few grams of nanoparticles, a large quantity of reagents is needed because of the low yield. Barium hydroxide, instead, has a water solubility too high to precipitate by supersaturation (39 g/L), and only a top-down approach was effective in yielding particles with nanometric size. For this reason, we used a top-down method also for strontium hydroxide, in order to obtain a sufficient amount of nanoparticles for the application. Moreover, the homogeneous precipitation for strontium hydroxide leads to another problem: the cooling step after the reaction causes the precipitation of the dissolved hydroxide, so that large crystals get mixed with nanoparticles. Although some of these are redissolved to give a supersaturated solution, the particle size distribution is affected by this phenomenon. After the precipitation we kept the resulting suspension at the reaction temperature, without stirring in order to let the particles deposit, and then we quickly removed the supernatant. The leftover was separated by hot filtering under vacuum. The nanoparticles did not pass through the cellulose filter because of their massive aggregation in water, so the oversized clusters remained on the filter. We changed the reaction condition in order to understand how the temperature and the concentration affected the particle size. The precipitate was washed five times with a saturated solution of strontium hydroxide to reduce NaCl concentration below 10^{-6} M. Each time, the volume ratio between the precipitate and the washing solution was about 1:10. The complete removal of NaCl from the suspension was checked with $AgNO_3$ tests.

4.1.4 Barium hydroxide

Barium oxide hydration

The alkaline earth oxides hydration is an exothermic reaction highly influenced by its own released heat. The enthalpy of reaction increases with the atomic number of the metal and this makes the hydration more or less vigorous (even violent). In the following table we calculate the enthalpy of reaction for every alkaline-earth. The barium oxide hydration is the most exothermic reaction, as shown in table 4.1. Furthermore, the reaction time is

lower than the calcium oxide hydration for example, and the added water, even if in stoichiometric excess, quickly evaporates. This leads to a hard phase of barium hydroxide, a behavior very different from magnesium and calcium.

Species	$\Delta_f H^o$(kJ/mol)	Species	$\Delta_f H^o$(kJ/mol)	$\Delta_h H^o$(kJ/mol)
BeO	-599 [3]	$Be(OH)_2$	-902	-303
MgO	-601	$Mg(OH)_2$	-927	-326
CaO	-635	$Ca(OH)_2$	-1002	-367
SrO	-591 [4]	$Sr(OH)_2$ [5]	-964	-373
BaO	-548	$Ba(OH)_2$ [5]	-940	-392

Table 4.1. The standard enthalpy of formation of alkaline-earth oxides and hydroxides and the enthalpy of reaction $\Delta_h H^o$ released during the oxide hydration. Published data were collected from NIST libraries and NIST Chemistry WebBook unless specified elsewhere.

We tried to synthesize the barium hydroxide with this method, changing both the molar ratio between water and oxide and the temperature, but every time the hard phase of hydroxide was not dispersible.

4.2 Dispersions formulation

Even though there are no chemical reactions involved, there are many aspects of chemistry present in a formulation. Some of the chemistry involved is thermodynamics of mixing, phase equilibria, solutions, surface chemistry, colloids, emulsions and suspensions. Even more important is how these principles are connected to stability, weather and temperature resistance, toxicity, and many other properties.

4.2.1 Magnesium hydroxide

Alcohol dispersions

The properties of the magnesium hydroxide particles were studied by dynamic light scattering. The measurements were carried out on the precipitate from the homogeneous synthesis and on the magnesium hydroxide obtained by hydration of the oxide. We investigated the cation-excess effect during the syntheses with molar ratio 0.5 and 0.7 by

comparing the DLS size distributions. Furthermore, we measured both the samples as they were and the dried ones to understand the role of water during the aggregation and settling phenomena in the alcoholic phase. The samples were dispersed with an ultra-homogenizer system (Ultraturrax T50) and by a sonication treatment.

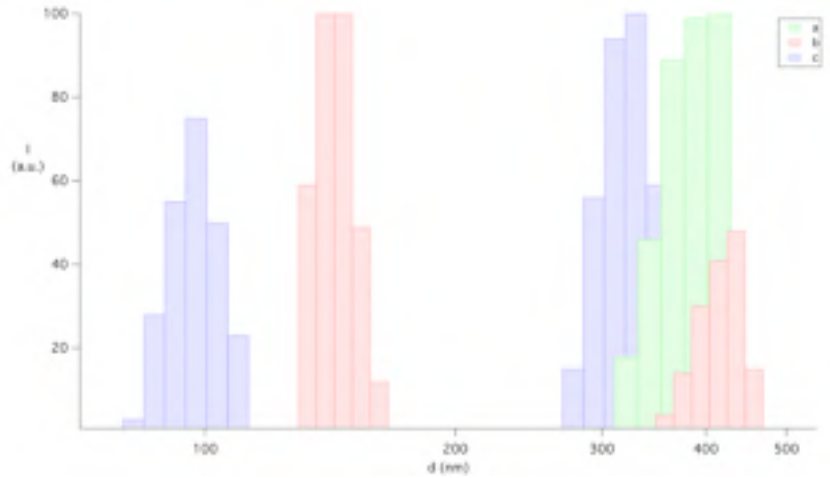

Figure 4.1. Histograms representing the size distribution: **a)** $Mg(OH)_2$ 1:2 wet, **b)** $Mg(OH)_2$ 1:2 dried and **c)** $Mg(OH)_2$ 1:1.4 dried nanoparticles dispersions obtained by analysis of the DLS measurements.

For the magnesium case, the drying leads to an increased stability of the dispersions. In fact, the water in the wet precipitate increases the amount of dissolved hydroxide: these charges are adsorbed on the particle surface but if on the one hand few ions increase the particle repulsion and stability, on the other a large number of ions promotes further solvation of the double layer. After the double layer solvation of the particles is saturated, the remaining ions are set free in the bulk phase, causing the aggregation. Dispersion of the wet precipitate of the 1:2 salt ratio preparation showed a unimodal particle size distribution centered at 350-400 nm; this size distribution is acceptable for a deacidification treatment, tough smaller particles are preferable to avoid whitening of inked paper and for a better homogeneity of particles distribution within the cellulose fibers. On the other hand, dispersion of dried particles of 1:2 ratio preparation re-dispersed in isopropyl alcohol showed a bimodal size distribution with the first distribution centered at around 140 nm and a second one centered at about 350-400 nm. For this reason, the dispersions used for applications on paper were prepared with dried magnesium hydroxide. Moreover, the cation-

excess synthesized particles lead to more stable dispersions with lower size distribution. During the synthesis of magnesium hydroxide, we used a slightly larger amount of magnesium with respect to the co-precipitating ions (1:1.4 molar ratio) producing smaller particles as shown in figure 4.1. DLS analysis of the dispersion obtained from the dried nanoparticles showed a bimodal size distribution with one particle population centered at 90 nm and the second one centered at 300 nm. The presence of free magnesium ions seems to inhibit nanoparticles clustering, suggesting the possible charging of particle surfaces with the Mg^{2+} excess, which partly inhibits aggregation without saturating the particle double layer.

Magnesium hydroxide obtained by oxide hydration was also investigated by light scattering.

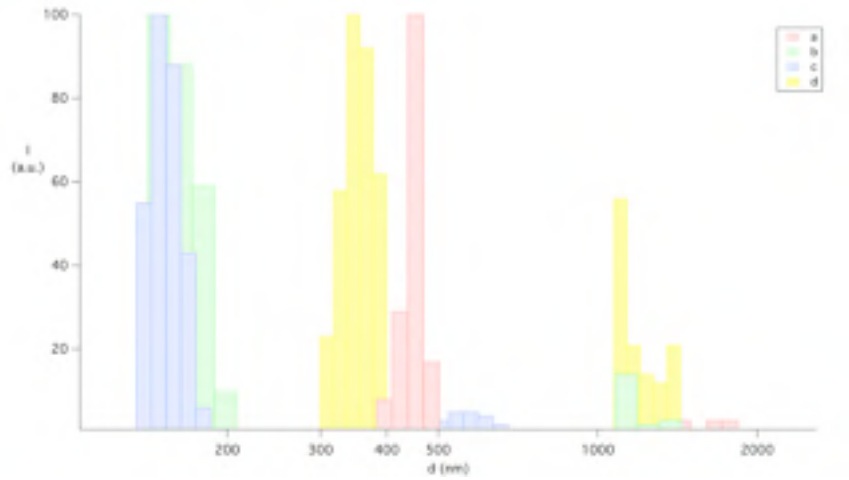

Figure 4.2. Histograms obtained by analysis of the DLS measurements representing the size distribution of $Mg(OH)_2$ obtained by the oxide hydration and dispersed in 2-Propanol: **a)** $Mg(OH)_2$ from MgO and H_2O, **b)** $Mg(OH)_2$ from MgO and KNO_3, **c)** $Mg(OH)_2$ from MgO and KOH, and **d)** $Mg(OH)_2$ from MgO and H_2O at 170°C for 12h.

The hydroxide obtained from magnesium oxide and water at room temperature showed a bimodal distribution of particle size centered at 450 nm and at 1.5 µm. Its 2-propanol dispersions were instable and aggregation phenomena were observed. When we used the 1M potassium nitrate solution, the particles were significantly smaller but a bimodal size distribution was still present. The histogram has the first maximum at 140 nm and the other at 1.1 µm and, although the larger particles could give whitening effect, this sample may be suitable for the paper application. The

best magnesium hydroxide nanoparticles were produced by reaction with potassium hydroxide. In this case, the size of the larger particles was reduced. The histogram showed a bimodal distribution of particle size centered at 140 nm and 550 nm. The reaction temperature, although to a minor extent, affected the particles size as well, as suggested by the shift of the first maximum at 350 nm.

If all these results are taken together, we can conclude that the most suitable dispersion for the deacidification of inked samples is the one obtained from dried particles of 1:1.4 salt ratio. Using smaller particles for paper treatment is preferred, aside for aesthetic reasons, because of their higher chemical reactivity. This plays a really important role in neutralizing acidity and in the carbonation process that provides the paper with an alkaline reserve of carbonate, essential to achieve a long-lasting deacidification.

Fluorinated fluid dispersions

A deacidification treatment based on magnesium hydroxide nanoparticles in alcohol dispersion is able to preserve paper, with a single treatment, from both acid hydrolysis and oxidative ink corrosion simply adjusting the final pH of deacidified paper to 6.5-7.5. In some cases however the polarity of the alcohols, as with aqueous treatments to a smaller extent, can cause modern ink loss (aniline-based), which is a problem with manuscripts or other valuable papers. It is therefore essential to choose fluids the nature of which is quite different from aniline-based inks: a fluorinated fluid meets these requirements.

The so-called *Bookkeeper method* provides a good deacidification effect: it consists of applying magnesium oxide microparticles and a fluorinated fluid. A consistent amount of surfactant is needed to stabilize these microparticles, and the eventual side effects during the natural aging of paper have not yet been clarified. In order to reduce the amount of fluorinated surfactants, our idea was to use smaller particles. We chose to synthesize hydroxide instead oxide particles because they present some advantages: an easy precipitation synthesis, a one-step reaction from hydroxide to carbonate and a better interaction with the polar head of surfactant.

We prepared six different dispersions changing both the chain length of the fluid and the amount of surfactant. We used three perfluoropolyether solvents:

Galden® HT70
Galden® HT90
Galden® LS215

These fluids have a chemical structure as represented in the formula reported below, where the *n* and *m* index are different for each one.

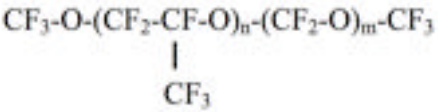

These solvents are clear and colorless so that the chromatic characteristics of the paper remain unchanged, they are inert, environmentally safe and non-toxic and they can penetrate paper easily because of their low surface tension, therefore carrying the nanoparticles with them into the paper.

In some formulations, we used a chloro-fluoropolyether surfactant to stabilize the dispersions (Fluorolink® 7800) with a chemical structure as represented in the formula reported below.

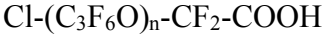

50 mg of dry $Mg(OH)_2$ synthesized by cation excess precipitation were dispersed in 10 mL of Galden LS215 and sonicated for 2h with a ELMASONIC S30H sonifer bath. After that, 7 mg of surfactant were added under stirring overnight. The resulting dispersion was unstable and flocculation phenomena occurred after 1h.

50 mg of dry $Mg(OH)_2$ synthesized by cation excess precipitation were dispersed in 10 mL of Galden LS215 with an ultra-homogenizer system (Ultraturrax T50) for 20 minutes and sonicated for 1h with a Branson 450 sonifier, without adding surfactant. The resulting dispersion was stable and no flocculation phenomena occurred within 12h, only a slow sedimentation.

In according with the results described above, the follow dispersions were produced using the 450 sonifer. With the same procedure, we prepared two dispersions with 50 mg of magnesium hydroxide in 10 mL of Galden HT90.

In the first one we added fluorolink one drop at a time, up to 30 mg, and then we performed the ultrasonic treatment, while the other was sonicated as it was. Both the dispersions were not stable, probably due to a lower viscosity then the galden LS215, which slowed down the sedimentation.

Although the LS215 dispersion was stable, homogeneous and did not contain surfactant that could have unknown side effects during the natural aging of paper, it had a high time of evaporation (the "215" refers in fact to the boiling point in °C) that led to a slow paper application.

The galden HT70 had a boiling point similar to the alcohols and it was suitable for paper treatments. Our aim was to obtain a dispersion that was as stable and homogeneous as the LS215 one and that contained the minimum amount of surfactant. We prepared two dispersions with 50 mg of magnesium hydroxide in 10 mL of Galden HT70. In the first one we added fluorolink one drop at a time, up to 50 mg and, before the ultrasonic treatment, we performed a further milling with the ultra-homogenizer. The other dispersion was sonicated as it was, without surfactant added. As the other fluorinated fluids, it was not sufficiently stable for the application.

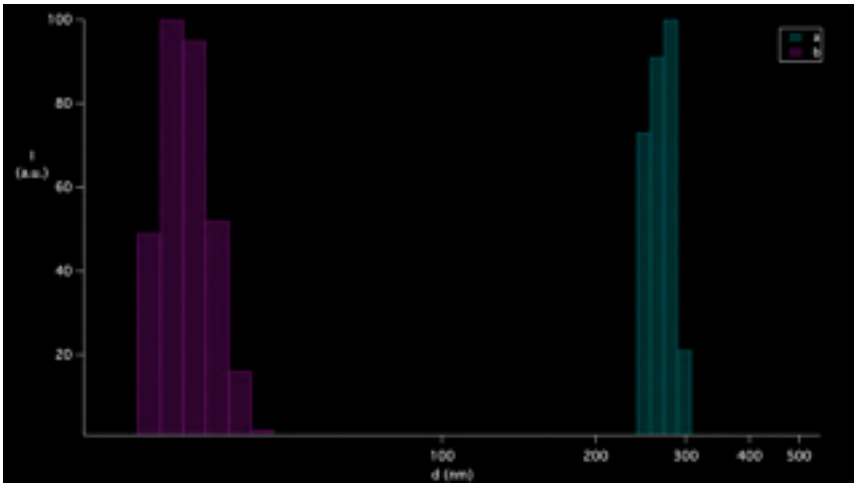

Figure 4.3. Histograms representing the size distribution: a) $Mg(OH)_2$ dispersed in LS215, b) $Mg(OH)_2$ dispersed in HT70 with surfactant, obtained by analysis of the DLS measurements. The LS215 had a viscosity of 6.840 cp and a refrative index of 1.281, while the HT70 had 0.840 cp and 1.280.

DLS size distributions show how the disaggregation phenomena were affected by the surfactant effect. Although the galden LS215 led to very stable dispersions without flourolink, the magnesium hydroxide

nanoparticles (270 nm) were considerably larger than the particles dispersed in galden HT70 with the surfactant (30 nm). However these dispersions were likewise stable because on the one hand the high viscosity of galden LS215 slowed down the sedimentation and on the other hand the fluorolink covered the particle surface, making it more similar to the fluorinated fluid.

Both dispersions are suitable for the paper application, but they both have their own drawback: the galden LS215 has a long evaporation time which implies a long restoration; the galden HT70 needs to have a surfactant to disperse the particles, but this could have side effects during the natural aging of the paper. Therefore, a treatment with an alcoholic solvent is always the best compromise, except for very soluble inks like anilinic ones.

4.2.2 Calcium hydroxide

Alcohol dispersions

The calcium hydroxide alcohol dispersions give numerous formulation possibilities. We used (and in some cases developed) some methods by using i) commercial dehydrated calcium hydroxide, ii) nanoparticles obtained from homogeneous precipitation, iii) commercial slaked lime, or iv) slaked lime produced by oxide hydration with potassium salt solutions.

700 mg of commercial dehydrated calcium hydroxide were dispersed in 140 mL of 2-propanol. This dispersion was split in seven vials and we added a different additive in each one. We put 10 mg of oleic acid in the first one, in two more the same amount of stearic acid and acetic acid, 10 mg of ethylene glycol, glycerol and cetyl alcohol in the three other respectively, and we left one additive-free. The samples were vigorously agitated and sonicated for 30 minutes. Afterwards, a turbidimetric analysis was carried out to observe possible stabilizing effects. The substances with the carboxylic group and long aliphatic chains led to clearly visible aggregation phenomena, probably due to the low affinity with the short branched chain of 2-propanol. In the acetic acid case this effect was less pronounced even though the dispersion stability was reduced. Both the ethylene glycol and glycerol interacted with the particles improving the dispersions stability. We would have expected to have a destabilizing effect with n-octanol, however we observed a slowing down of the settling rate. This phenomenon could be explained with a different changing of the particle surface charge with a carboxylic group or an oxydrilic one. In fact, a carboxylic acid could react with the hydroxide surface forming an esteric bond, leading to immobilization and changing the

charge of the particle. When we used glycol and glycerol the hydrogen bond was the prevailing interaction, therefore the surface charge did not majorly change.

Therefore, from a first analysis the chain length and the polar head of the surfactant, the solvent and the surface charge of the particles represent the key factors in the stabilization of dispersions.

Although some kind of surfactants would improve the dispersion stability, it would be better to avoid their use for frescos consolidation. Typically they have a lower vapor pressure than the solvent, which would slow down the application, and they could remain on the surface of the painting, causing the fresco to age. In fact, both carboxylic acids and alcohols with long aliphatic chains undergo oxidation, which causes the yellowing of these substances and thus the yellowing of the fresco. Therefore to maximize the dispersion stability and to increase the surface permeation we needed to reduce the size of the particles.

The size distribution of calcium hydroxide dispersions was studied by dynamic light scattering. The measurements were carried out on the precipitate of the homogeneous synthesis, on calcium hydroxide by hydration of the oxide and on the dispersions prepared with slaked lime (see below).

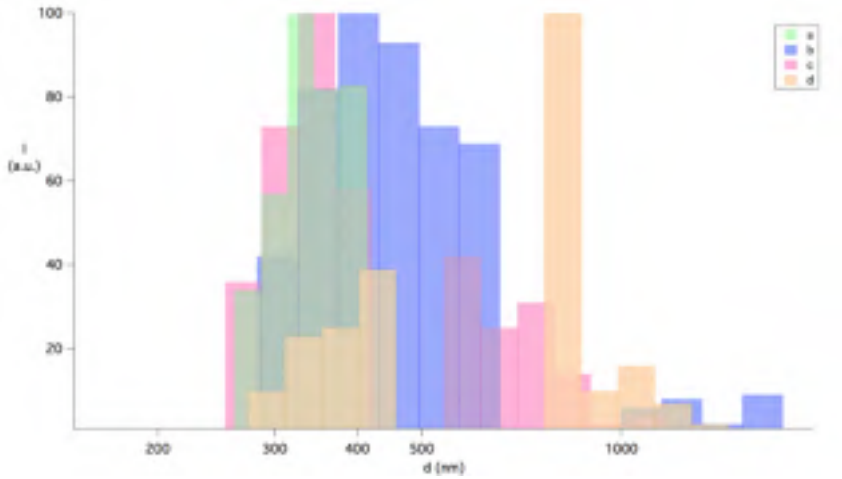

Figure 4.4. Histograms obtained by analysis of the DLS measurements, representing the size distribution of calcium hydroxide samples dispersed in 2-propanol: **a)** $Ca(OH)_2$ dispersion obtained by slaked lime dilution, **b)** $Ca(OH)_2$ yielded by calcium oxide hydration, **c)** and **d)** $Ca(OH)_2$ yielded by calcium oxide

hydration with 1M solution of KOH and KNO_3 respectively. The 2-propanol have a viscosity of 2.27 cp and a refrative index of 1.374.

Figure 4.4 shows the decrease in particle size as the water ionic strength used in the oxide hydration increased. As in the magnesium oxide case, the particles synthesized with the potassium hydroxide were smaller than the ones synthesized with the potassium nitrate (centered at 370 nm and at 1 μm). This is probably due to the high pH of the potassa solution: the high concentration of hydroxide groups could increase the amount of calcium oxide available to react, reducing the oxide core and increasing the surface charge. The difference from the magnesium oxide case was that the particles were more polydisperse in diameter, and two size distributions were observed (centered at 330 and at 700 nm). It is clear from the figure that the sample with the smallest size distribution is the one produced with the heat-treated slaked lime dispersion.

It has been shown that it is possible to obtain stable slaked lime/alcohol dispersions that can be used in wall painting conservation [6]. These dispersions were stable for many hours: this stability is particularly important for their possible application. In fact, the high kinetic stability of the dispersions is fundamental for avoiding lime deposition on the painted surfaces and consequent irreversible white glazing.

The slaked lime has a systematic presence of platelike nanoparticles that aggregate into micron-sized clusters [7]. Typically, the size of individual $Ca(OH)_2$ particles ranges from 30 up to 200 nm. However, a few micron-sized (1-3 μm) platelike particles were also observed. The nanosized platelike crystals are very similar to those obtained via homogeneous phase precipitation under highly supersaturated conditions. Furthermore, the cluster core can contain some remnants of calcium oxide. The water-dispersed slaked lime (1:1 w/w) under differential scanning calorimetric (DSC) measurements showed in fact an exothermic behavior, as follows

$$CaO + H_2O \rightarrow Ca(OH)_2 + 63.7kJ/mol$$

The temperature raises in the first step of the reaction because the surface of the calcium oxide powder transforms into hydroxide, quickly releasing heat. The calcium oxide in the core of the particle is entrapped, the amount of heat produced decreases as the reaction rate decreases and the heterogeneous mixture cools down until it reaches room temperature. For this reason, an aging of months is required to obtain a good slaked lime,

although a relevant amount of oxide is stuck in the core of the particles.

We dispersed the slaked lime in water and brought the mixture to high temperature to convert all the oxide into hydroxide. During this reaction, the core increases its volume, from a density of 3.345 to 2.23 g/cm^3 [8]. Probably this expansion breaks down the core into nanometric particles, improving the characteristics of calcium hydroxide whose size becomes now suitable for alcoholic dispersion and fresco application.

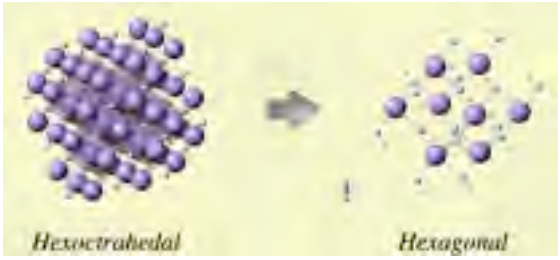

Figure 4.5. The calcium oxide (on the left) and hydroxide (on the right) structures.

After the reaction was completed, the platelike particles were highly aggregated and we needed an alcoholic solvent to dilute and disperse them.

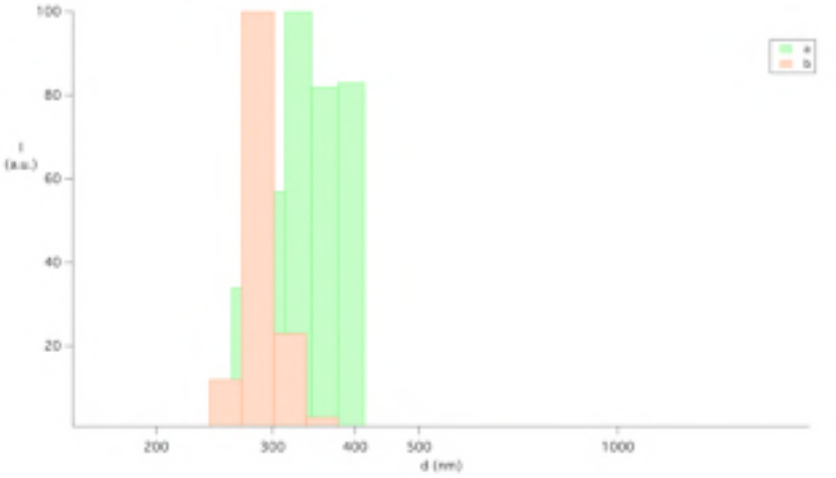

Figure 4.6. Histograms obtained by analysis of the DLS measurements, representing the size distribution of calcium hydroxide samples dispersed in 2-propanol: **a)** $Ca(OH)_2$ dispersion obtained by slaked lime dilution, **b)** $Ca(OH)_2$ yielded by homogeneous precipitation. The 2-propanol have a viscosity of 2.27 cp and a refrative index of 1.374.

We noticed that, in order to disperse calcium hydroxide, the best alcohol was the 2-propanol, according to the work of V. Daniele and G. Taglieri [9]. The alcoholic mixture was sonicated with a Branson 450 sonifier and studied by dynamic light scattering measurements.The differences between two sample in figure 4.6, i.e. the heat-treated slaked lime diluted in alcohol and the precipitate by homogeneous synthesis, were small and almost negligible for the wall-painting application. The size distributions are centered at 340 and at 290 nm, respectively.

4.2.3 Strontium hydroxide

Alcohol dispersions

We carried out four homogeneous syntheses (all starting from a 1M solution of chloride) of strontium hydroxide with different sodium hydroxide concentration (0.25 and 2 M) in order to change the molar ratio between reagents leaving a cation-excess 8:1, and at different temperatures (25 and 90 °C). We dispersed the dry powders in 2-propanol under sonication and analyzed the four suspensions with DLS. The particles synthesized at low temperature and without the cation-excess were polydisperse, unstable and they quickly settled. Under these conditions, the DLS measurement gives unreliable results since the autocorrelation function has a null baseline index (the relaxation rate Γ that is calculated to obtain the diffusion coefficient cannot be estimated without a linear baseline for whose the baseline index, introduced by Brookhaven Instrument, is 10).

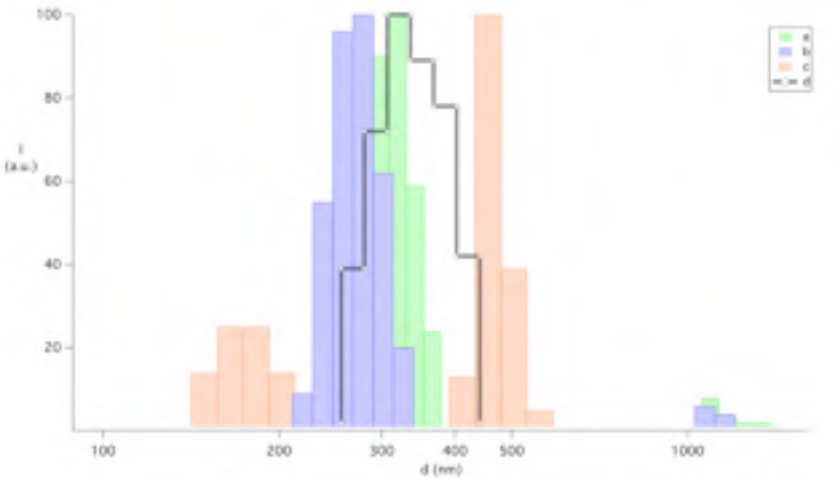

Figure 4.7. Histograms obtained by analysis of the DLS measurements, representing the size distribution of strontium hydroxide samples dispersed in 2-

propanol: **a)** $Sr(OH)_2$ obtained by cation-excess homogeneous synthesis at 25°C, **b)** and **c)** $Sr(OH)_2$ yielded by homogeneous precipitation at 90°C with and without the cation excess and **d)** $Sr(OH)_2 \cdot 6H_2O$ milled and sonicated in 2-propanol.

The cation-excess synthesis at 25°C led to particles with a multimodal size distribution. The smallest population size was centered at 335 nm and the other one at 1.05 μm. Even though the sample was stable enough to allow the DLS measurement, the largest population size was unsuitable for the paper application. The particles obtained from the high temperature synthesis (90°C) were slightly smaller than the ones synthesized at low temperature, thus they were not enough. The best synthesis to produce nanoparticles of strontium hydroxide was the one at 90°C with cation-excess. In this case we observed a two-modal size distribution, but with lower mean diameters. The smallest population had a mean diameter of 160 nm while the other of 430 nm.

In figure 4.7 we reported the three size distribution of the sample prepared with powders from homogenous synthesis (in green, blue and red) and the one of the sample prepared with a top-down approach, from the strontium hydroxide hexahydrate with the ultra-turrax homogenizer (the clear hystogram). We put 13g of $Sr(OH)_2 \cdot 6H_2O$ in 500 mL of 2-propanol and mixed with the homogenizer for 20 minutes. After that we poured the dispersion leaving at the bottom the strontium hydroxide remnants which had been not milled (~ 0.5g). Although the size distribution was larger than the smallest population of sample **(c)** (red hystogram), the milled strontium hydroxide was more monodisperse having only one size population. Moreover, the top-down approach had the advantage of reducing the reagent waste caused by the high solubility of this hydroxide. The population was centered at 330 nm and the dispersions did not give the whitening of the inked paper.

4.2.4 Barium hydroxide

Alcohol dispersions

In homogeneous precipitations, the low yield of the moderately soluble nanomaterials is even further reduced by the purification step, even if a saturated solution of the product is used for washing. Therefore, the synthesis of barium hydroxide nanoparticles must take place through a top-down approach. The preparation of barium hydroxide nanoparticles and the formulation of dispersions in aliphatic alcohols (ethanol, 1-propanol, 2-propanol and 1-butanol) were studied. In particular, the role of alcohol in

the de-aggregation of barium hydroxide powders during milling was investigated. A wide range of particle concentrations was considered with the twofold aim of collecting information about the specific interactions of the solvent with the particles and of determining the best concentration to be used for the application to wall paintings. Both 1- and 2-propanol show appropriate features for the application purposes: they are environmentally friendly and volatile, they possess low surface tension and low viscosity. Despite these similarities, the two solvents behave very differently. 1-propanol, in fact, gives more stable dispersions and fast de-aggregation. For the above mentioned reasons, this series of short chain aliphatic alcohols was investigated and the resulting dispersions were characterized by light scattering and small angle X-ray scattering (DLS and SAXS).

The "break-down process" of physically dividing powders into finer fragments by milling was used to prepare nanoparticles of barium hydroxide octahydrate. A high-performance treatment of commercially available barium hydroxide octahydrate powders allowed to obtain nanostructures and to formulate stable dispersions in alcohol. Nanoparticles were obtained by means of an ultra-homogenizer system (Ultraturrax T50) through thermo-mechanical action on the powder dispersed in a short-chain alcohol solvent. Grain particles were milled for 20 minutes at 15000 rpm to promote disaggregation and to reduce them to nanostructured units. Alcohols with aliphatic chain of different lengths were used in order to investigate the effects on the cluster milling process. The initial concentration was 1g/40 mL. Ethanol, 1-propanol, 2-propanol, and 1-butanol were selected for the experiments. These were labelled as EtOH, 1-PrOH, 2-PrOH, 1-BuOH, respectively.
Aggregation and dissociation phenomena caused quantifiable changes in particle size distribution and this affected the kinetic stability and other macroscopic properties of the colloidal dispersions. For example, by using 1-butanol, a very stable dispersion was obtained, while using 1-propanol led to a tixotropic gel. Gelling process was observed by adding concentrated particle dispersion (1g/40 mL) one drop at a time to pure 1-propanol. The added solid particles dispersed completely up to a certain point, giving a dispersion that, although containing scattering elements under laser irradiation, resulted almost totally clear to the naked eye; beyond this critical parameter the sample clouded. Further addition led to a complete gelling of the system.

SAXS analysis

Small angle X-ray scattering (SAXS) was used to characterize the size and the polydispersity of particles and to investigate the influence of the various alcohols on the structure factor as well as on the form factor of the diluted (1g/L) dispersions. Dilution was necessary to avoid sedimentation during SAXS acquisition (t=2h). In principle, a Schulz spheres' model or a sum model of two Schulz sphere functions were used to account for the presence of one or two size populations.

Table 4.2 reports the average particle sizes and the polydispersity of the four barium hydroxide/alcohol systems investigated.

Systems	Particle radius (nm)		Polydispersity	
EtOH	20	40	0.20	0.19
1-PrOH	12		0.59	
2-PrOH	3	47	0.48	0.24
1-BuOH	5.4	31	0.50	0.25

Table 4.2. Particle radius and polydispersity of the investigated systems, obtained by using a simple or a sum model of Schulz sphere functions.

Ethanol is the most polar among the solvents used and it partially dissolves barium hydroxide. This resulted into solvent degradation, due to hydroxide ions, that brought to yellowing, making ethanol dispersions unsuitable for cultural heritage applications.

SAXS profile was fitted with a sum of two Schulz sphere functions to obtain two populations with mean radii of 20 and 40 nanometers (see figure 4.8). The volume fraction ratio was 0.50, with the larger objects being the major component, and the polydispersity of both fractions was about 0.2. Unlike the 1-propanol dispersion, concentrated systems (1g/40mL) in ethanol did not form a gel. All solvents showed a rather similar behavior, i.e. a sharp decrease of the clusters' disaggregation capability beyond a defined particle concentration; below this critical concentration the optical density of the system remained almost constant and close to that of pure ethanol.

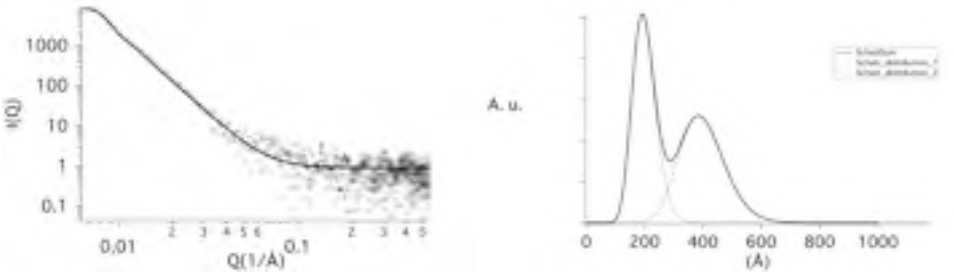

Figure 4.8. (a) SAXS profile of EtOH dispersion and fitting curve obtained by a sum model of two Schulz sphere functions. Barium hydroxide scattering length density (SLD) was $1.57 \cdot 10^{-5}$ Å^{-2} and ethanol SLD was $7.58 \cdot 10^{-6}$ Å^{-2}. (b) Normalized Schulz size distributions obtained by using the fitting results reported in Figure 4.8a. The volume fractions of the two populations were 0.039 and 0.079, respectively.

Dynamic light scattering measurements were performed on this system in order to investigate the size distribution of the scattering elements visible under laser radiation. Two diluted samples of different concentration, 0.15 and 0.3 g/L both below the critical concentration value, were analyzed in order to monitor size distribution changes during the addition of particles. It was so possible to follow the aggregation process, and the cluster formation that strongly modifies the optical density above the critical concentration.
Two measurement series were performed. An identical mean size distribution was hypothesized for both systems: in the case of no aggregation phenomena, the average dimension of the particles would result unaffected by the concentration of the diluted samples. Each series was composed of 6 and 7 measurements respectively to collect 10 runs of 30 s. One-way ANOVA analysis (analysis of variance) indicated that these values were not statistically different ($\alpha = 0.01$) and, therefore, it can be concluded that below a critical concentration cluster formation is strongly limited and polydispersity of the system depends only on the size of isolated objects. In fact, it is important to highlight that the hydrodynamic diameter of particles in the ethanol dispersion, obtained by Stokes-Einstein equation, was 258±55 nm.

The anomalous gelling characteristics of a 1g/40mL barium hydroxide dispersion in 1-propanol were investigated by SAXS (see figure 4.9). A set of samples with different concentration was prepared. Samples were labelled as 1-PrOH_5 (20 g/L), 1-PrOH_4 (22.5 g/L), 1-PrOH_3 (25 g/L), 1-PrOH_2 (28.5 g/L), and 1-PrOH_1 (33.3 g/L).

The amount of powder to be milled was increased up to 20 g/L. All the examined systems were observed for some hours after milling to check the kinetic stability of the dispersions. 1-propanol showed a unique behavior. In fact, by increasing the concentration, a gelling process was observed. At the concentration of 20 g/L, a tixotropic gel was formed in 24 hours after milling. This phenomenon was investigated in order to better understand the specific interaction of 1-propanol with barium hydroxide. SAXS experiments on dispersion with concentration ranging from 20 to 33.3 g/L were performed. Each sample was shaken before the measurement to homogenize the sample and to form a single phase; then it was poured into the capillary. Surprisingly, the sample with a concentration of 25g/L did not show phase separation as time went by.
SAXS profiles showed several Bragg peaks in the 0.1÷0.6 $Å^{-1}$ region. This suggested that nanoparticles were packed to form periodic structures, to give several peaks, corresponding to the inter-particle d-spacing within a chain of stacked discs.

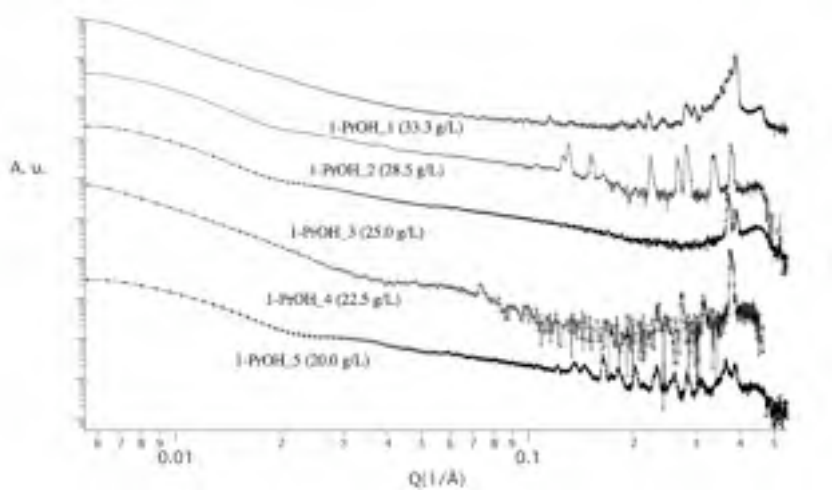

Figure 4.9. SAXS profiles of barium hydroxide dispersion in 1-propanol at different concentration. From top to bottom: 1-PrOH_1 is 33.3g/L; 1-PrOH_2 is 28.5g/L; 1-PrOH_3 is 25.0g/L; 1-PrOH_4 is 22.5g/L; 1-PrOH_5 is 20.0g/L.

SAXS patterns measured on the same samples after ten days showed fewer peaks as a result of the reorganization of the gel network during the phase separation (figure 4.10). By mixing the upper phase (solvent) with the lower one, the immediate swelling of the gel can be observed, with subsequent increase of the *d*-spacing among nanoparticles which gives more diffraction

peaks at lower *q*-values.

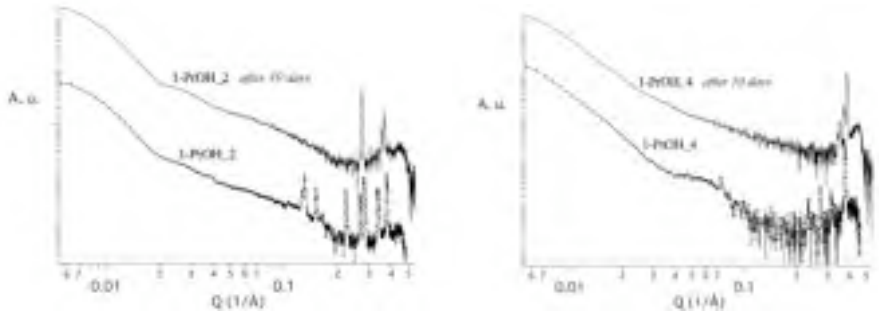

Figure 4.10. SAXS profiles of 1-PrOH_2 and 1-PrOH_4 dispersions collected after 10 days. The number of peaks reduced with time.

These *d*-spacings could correspond to metastable superstructures that slowly convert into stacked chains, where the discs are aligned one on top of each other. Equation (1) reproduced the Bragg's peaks of the curve with good approximation. It gives the total coherent scattered intensity from stacked discs with a core/layer structure.

(1) $$I(Q) = N\int_0^{\frac{\pi}{2}}\left[\Delta\rho_t\left(V_t f_t(Q) - V_c f_c(Q)\right) + \Delta\rho_c V_c f_c(Q)\right]^2 S(Q)\sin\varphi d\varphi + bkg$$

where N is the number of discs per unit volume, $\Delta\rho$ represents the scattering length density difference between the component of the system (core or layer) and the solvent, φ is the angle between q and the axis of the disc. V_t and V_c are the total volume and the core volume of a single disc, respectively. We assumed that the scattering length density (SLD) of the layer is the same as that of the solvent,

$$\Delta\rho_t = \rho_{layer} - \rho_{solvent} = \rho_{solvent} - \rho_{solvent}$$

thus the first part of the equation is zero. Equation (1) reduces therefore to equation (2):

(2) $$I(Q) = N\int_0^{\frac{\pi}{2}}\left[\Delta\rho_c V_c f_c(Q)\right]^2 S(Q)\sin\varphi d\varphi + bkg$$

The form factor is given by:

(3) $$\left\langle f_c^2(Q)\right\rangle_\varphi = \int_0^{\frac{\pi}{2}} \left[\left(\frac{\sin(Qh\cos\varphi)}{Qh\cos\varphi}\right)\left(\frac{2J_1(QR\sin\varphi)}{QR\sin\varphi}\right)\right]^2 \sin\varphi d\varphi$$

where $2h$ and R are the thickness and the radius of the disc (see figure 4.11), respectively and J_1 is the Bessel function.
The structure factor is given by:

(4) $$S(Q) = 1 + \frac{2}{n}\sum_{k=1}^{n}(n-k)\cos(kDq\cos\varphi)\exp\left[\frac{k(Q\cos\varphi)^2\sigma_D^2}{2}\right]$$

where n corresponds to the total number of stacked discs, D (see figure 4.11) and σ_D represent the next neighbor center-to-center distance (d-spacing) and its Gaussian standard deviation, respectively.

Figure 4.11. Schematic representation of the hypothesized structural organization of barium hydroxide particles in a concentrated system.

Since narrow peaks are present in the pattern (figure 4.12), the Gaussian function σ_D can be considered very narrow, which allows setting this parameter equal to zero, and therefore to assume that the d-spacing (D) between neighbor discs is always the same along the chain.

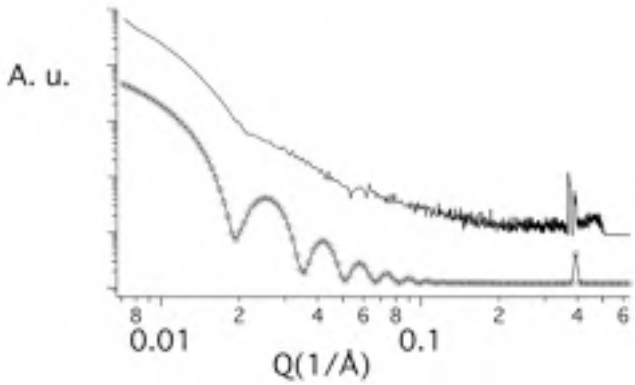

Figure 4.12. SAXS profile of 1-PrOH_3 system (top) and the theoretical stacked-discs model function showing the same peak at 0.39 $Å^{-1}$. The Bessel pattern, not

shown in the SAXS pattern, is probably due to the scattering contribution of the particles dispersed into the gel.

The curve in the lower part of figure 4.12 represents the model function used to fit our experimental data (at q-values over 0.1 $Å^{-1}$). It is obtained setting R = 200 Å and D = 16 Å, and the number of stacking discs, n, is 120. This latter affects the Bragg peak intensity but not its position: the q-value of the peak is determined by the height of the disc and by the thickness of the solvent layer, i.e. the next neighbor center-to-center distance, other than by the disc radius. The fitting function shows only one peak, at q=0.39 $Å^{-1}$: the other peak could be due to a metastable structure where the discs are not aligned completely and the next neighbor center-to-center distance increases shifting the peak at lower q-values. In fact, the SAXS profile after one month showed only the peak at 0.39 $Å^{-1}$. Since the chain length corresponds to the number of stacked discs n, and since n does not effect the q-value of the peak, the peak shifting can not be caused by the break of the chains but only by a swelling of them.

Electron scanning microscopy showed the presence of micron-sized particles and clusters, which presumably are not involved in the gel formation. This also implies that a major contribution to the SAXS curve could be given by their surface scattering. The presence of micro and sub-micrometric particles can be deduced by combining SAXS results and scanning electron microscopy, which completed the description of the size distribution. These particles may further contribute, through the interaction with the primary beam, to modify the gel SAXS profile.

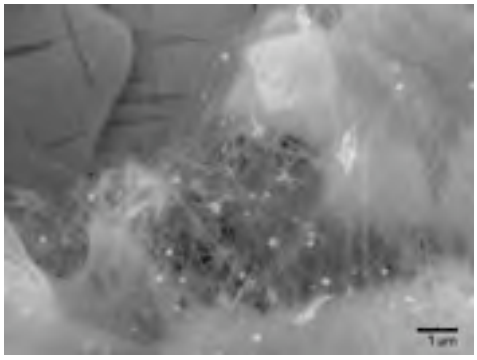

Figure 4.13. Scanning electron micrograph of a collection of micrometric, sub-micrometric, and fibrous tiny crystals of barium hydroxide in 1-PrOH_2 sample. The same sample observed in low vacuum conditions.

For this reason, even though the nanoparticles do not have a spherical shape, the Schulz sphere model represented a good approximation and it was the function that best fitted these spectra for *Q*-values lower than 0.1 $Å^{-1}$, as shown in figure 4.14. The micro and sub-micro particles were not taken in account: we eliminated them with a rapid sedimentation (10 minutes) after the sample dilution and then we used the dispersions for the fresco consolidation.

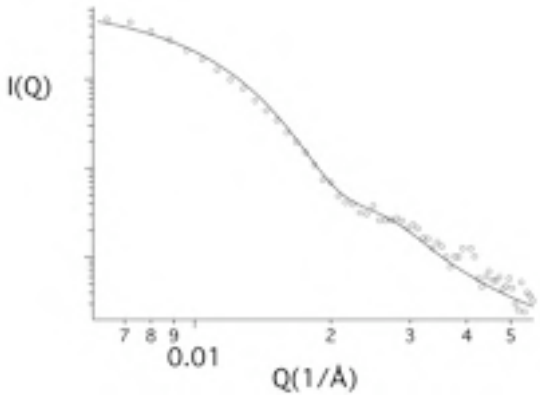

Figure 4.14. Low-Q region of SAXS profile (Q < 0.1 $Å^{-1}$) of 1-PrOH_2 system (28.5 g/L) and fitting curve obtained by Schulz spheres function (volume fraction 0.02, average radius 20 nm, and polydispersity 0.2).

Diluted 1-PrOH_2 dispersion (1g/L) did not show any Bragg peaks (figure 4.15). This means that the system loses its superstructure upon dilution and the nanoparticles are completely dispersed by the solvent.

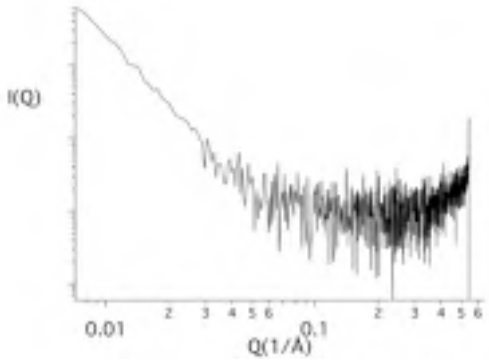

Figure 4.15. SAXS profile of 1-PrOH_2 after dilution to 1g/L. Below a critical concentration all the superstructures disappear.

The critical concentration above which periodic structures form is 2.8 g/L.

This value was measured stepwise by adding gel drops into pure 1-propanol, under vigorous stirring. The mean particle radius of 12 nm, with a unimodal size distribution, and 0.59 polydispersity was obtained by using a Schulz sphere model.
2-PrOH dilute dispersion (1g/L) is the least kinetically stable systems and particles showed high polydispersity. SAXS profile (figure 4.16) was fitted with a sum of two Schulz's sphere functions obtaining two populations with mean radius of about 3 nm and 47 nm, respectively (table 4.2).

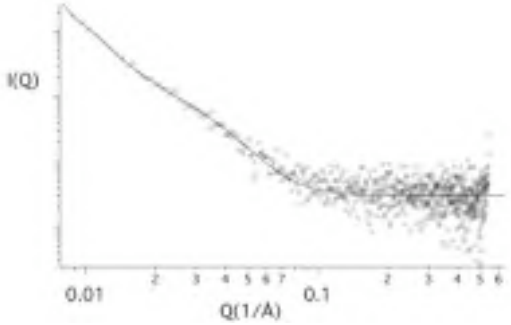

Figure 4.16. SAXS profile of 2-PrOH dispersion and fitting curve obtained by a sum-model of two Schulz sphere functions. Barium hydroxide scattering length density (SLD) was set at $1.57 \cdot 10^{-5}$ and 2-propanol SLD was $7.6 \cdot 10^{-6}$. The volume fractions of the smaller and larger population were 0.002 and 0.005, respectively.

It is interesting to note that a high dilution of 1-PrOH gel (25g/L), by using 2-propanol, did not induce any disaggregation of the fibril structures previously described. This proves the scarce affinity of barium hydroxide for 2-propanol, and its very high affinity for 1-propanol. This was also highlighted by the results obtained during the milling process.

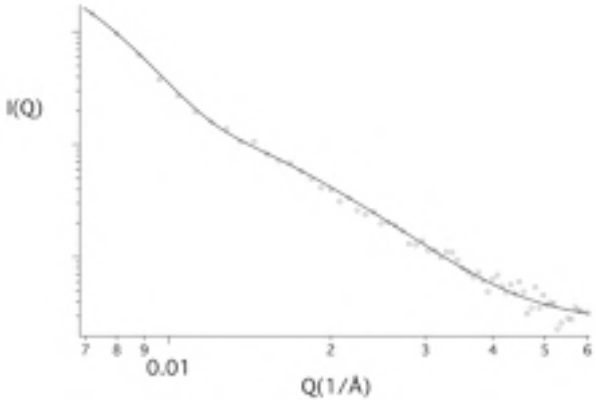

Figure 4.17. SAXS profile of 1-BuOH dispersion and fitting curve obtained by a sum-model of two Schulz sphere functions. Barium hydroxide scattering length

density (SLD) was set at $1.57 \cdot 10^{-5}$ and 1-butanol SLD was $7.81 \cdot 10^{-6}$. The volume fractions of the smaller and larger population were 0.001 and 0.002, respectively.

1-butanol, as well as 1-propanol, formed very stable dispersions. However, SAXS profile showed that milling in 1-butanol brought to more polydisperse suspensions (figure 4.17 and table 4.2). In fact, I(Q) was fitted with the sum of two Schulz sphere functions.

According to these results, dispersions of barium hydroxide nanoparticles in 1-propanol (1 g/L) looked more promising for the application because of the particle average size, which is compatible with the porosity of wall paintings, regardless of the painting technique. The use of particles instead of solutions promotes the deposition of the new binding material on the damaged paint layer, with a more efficient action in correspondence of powdering and flaking of color. 1-propanol forms dispersions with high kinetic stability; this means that solvent prevents nanoparticles from clustering and promotes the penetration of particles through the pores. In this sense, 1-propanol, as already demonstrated in a previous paper [10], is a very good solvent for application to wall paintings. 1-propanol should also be preferred to others (i.e. 1-butanol) because, in addiction to high dispersion stability, it is more volatile, it has a low surface tension, and it is environmentally friendly.

Carbonatation reaction

The carbonatation rate of $Ba(OH)_2$ nanoparticles is a key parameter to assess their reactivity and discuss their potential application in conservation of wall paintings. In this sense, XRD patterns of dry powders allow the determination of the size of crystalline domains, according to Scherrer equation, and to find correlations between reactivity and crystallinity of the small grains. Unfortunately, after the milling and freeze-drying necessary to obtain dry powders, most of the hydroxide particles reacted to give the carbonate. Nanosized particles, produced by milling, are much more reactive and simple manipulation of dry powders is enough to promote the carbonatation process. Even though this fast carbonatation made the analysis more difficult, it is really a favorable behavior for culture heritage application because a complete carbonatation reaction, occurring in a few days, would be preferred to achieve good consolidation of wall paintings. According to the already mentioned method, the carbonatation kinetics of particles contained in a drop of dispersion deposited over a KBr pellet was followed through infrared spectroscopy, FT-IR (figure 4.18). Concentrated

systems were chosen for the experiments in order to have the highest intensity of absorption. Samples were monitored stepwise since drop deposition until reaching an asymptotic value of the peak area of carbonate. During the solvent evaporation, a saturation of the signal was achieved and no meaningful spectra could be collected. The time needed to obtain a clear spectrum was assumed to be the evaporation time of solvent. It is obvious that this process could not be considered totally completed, but it was assumed that carbonatation occurring during this time was negligible.

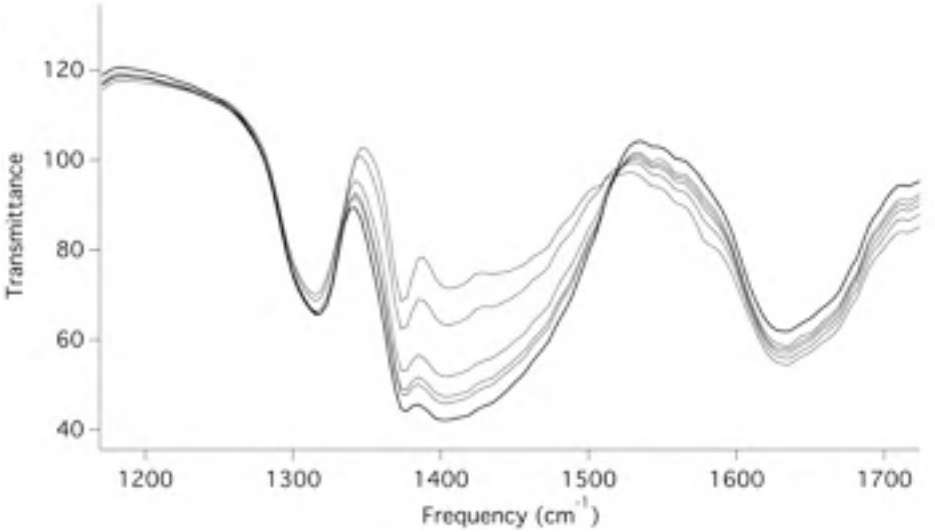

Figure 4.18. FT-IR spectra of 1-PrOH system, collected during carbonatation reaction.

Kinetics curves of EtOH, 2-PrOH, and 1-BuOH systems were fitted with an exponential function to estimate the time needed to reach an asymptotic value (figure 4.19). The following results were obtained: EtOH 320 s, 2-PrOH 158 s, and 1-BuOH 450 s. These values correspond to the characteristics of each dispersion: the longer carbonatation time, the higher dispersion capability of the solvent. According to the already mentioned definition, "evaporation time" was 115 s, 130 s, and 260 s respectively, in agreement with the volatility of the respective alcohols.

Interestingly enough, 1-PrOH dispersions show a kinetic curve with some discontinuities. In this case the evaporation time was 1000 s, and probably not all the solvent was evaporated when the carbonatation started. Also the carbonatation time of this sample was longer than other systems, 700 s.

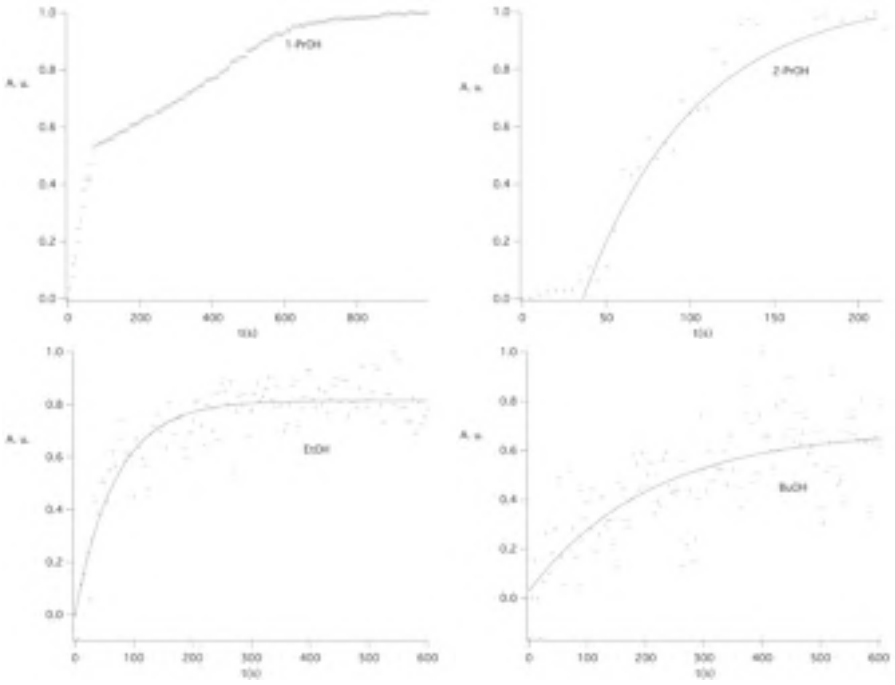

Figure 4.19. Kinetics curves obtained by measuring the absorption IR peak area of formed barium carbonate. EtOH, 2-PrOH, and 1-BuOH data are shown with an eye-line guide to evidence the shape of the curves. 1-PrOH curve showed much less dispersed data with a characteristic discontinuous shape.

In some way, this further confirmed that the interaction between 1-propanol and the nanoparticles was significant, as demonstrated by SAXS analysis, and by the settling process of barium hydroxide.
In general, it can be assumed that a similar behavior, even though less pronounced, is expected also for diluted systems. The features of the 1-PrOH system perfectly match the requirements of restoration. The evaporation time of the solvent and the carbonate formation process must allow an efficient and homogeneous penetration and distribution of particles, to prevent a white veil to form over the paintings.

4.3 Cultural Heritage Restoration

Nanotechnology has recently begun to play an important role in the field of cultural heritage conservation. This is due both to the excellent results obtained and to the meaningful improvements of the conventional

methodologies achieved by using novel nanosystems based on dispersions of precipitated inorganic nanomaterials, especially for wall paintings consolidation, and paper and wood deacidification. In fact, calcium hydroxide and magnesium hydroxide have been largely used in the past as aqueous solutions or sols to solve degradation problems. Even though, in principle, these water-based systems should be preferred, their application has numerous drawbacks and an alcoholic dispersing agent can solve them.

4.3.1 Paper deacidification

The main cellulose degradation pathways are the acid hydrolysis of glycosidic bonds and oxidation. Low pH values can lead to cellulose depolymerization even at room temperature.

The magnesium hydroxide nanoparticles were applied over a sample of Whatman paper n°1 (Schleicher & Schuell, 99% made with cotton fibers, 88.0 g/cm^2; polymerization degree, DP, 1230). This paper was selected because it can be considered a standard for a macro-invasive analysis on the degradation of cellulose after deacidification treatment and artificial aging. Inks were applied on reference paper with a brush. After a week at constant room humidity (RH 65%, 25°C), the samples were weighed in order to evaluate the amount of ink present on paper.

The samples were treated with nanoparticles, dispersed in alcohol at 0.11M. One milliliter of dispersion was applied with a brush on each sample on both sides. The treated samples were then left to dry in the air for ten days at controlled RH, i.e. for the time necessary for hydroxide to neutralize acidity and to change into carbonate. After that time, samples were weighed.

Paper degradation may be described as a shortening of cellulose chains, a depolymerization process, DP. DP can be obtained from viscosity determinations. In order to normalize results obtained from different techniques, the number of scissored glycosidic bonds (S, scission number) is commonly preferably used and defined as:

$$S = \left(\frac{1}{DP_{v,t}} - \frac{1}{DP_{v,0}} \right) \cdot 100$$

A sample treated with nanoparticle dispersions was compared to an untreated sample containing the same iron-gall ink amount. The scission

number of the first one, after aging (48h), was 0.45% while the untreated one had S=0.74%. The appearance of the treated samples after an aging cycle was good and no clear difference was detected with respect to not aged samples, while the sample without treatment showed a severe and diffuse browning, just after 24 hours and it was very fragile (complete loss of the mechanical properties just after 12 hours). The dispersing media did not induce any ink loss and $Mg(OH)_2$ nanoparticles consistently improved the resistance of paper to aging. Inked-paper treated with nanoparticles, after aging, preserved most of the typical mechanical properties of the original paper; in particular, tensile strength and elasticity remained close to their initial value.

4.3.2 Archeaological wood preservation

The wood from the Vasa can be divided in three zones, according to the pH values measured with aqueous extraction:

a. Wood from the inner part of the timbers (80mm from the nearest surface) shows very low pH values, around 2 units;
b. Wood from the surface displays a great variations in pH: very acidic conditions are found where salt precipitations are present, whereas pH values around 5-6 units are sometimes measured;
c. The intermediate region shows a general decreasing pH from the surface to the interior.

From a unique large block of pinewood from the Vasa (number 25647b), two samples of a volume of about 200cm^3, called Pine_II_Ca and Pine_II_Mg were obtained. The surfaces of the block were very dark and many spots of salts precipitation were present. The wood is unnaturally heavy and it is greasy, similar to a wax candle. As a matter of fact, samples are completely impregnated with PEG that is the major responsible of the strange appearance of the wood. It is obvious that a deacidification treatment without a removal of PEG is unfeasible; fortunately, PEG is highly soluble in water and, even tough, some of the samples are completely filled with the polymer, a prolonged immersion may remove the filler. Therefore, after washing and drying, the samples were immersed in the alkaline-heart metal hydroxide dispersions. The selected concentration for the first application was 1g/L. In order to evaluate the penetration of the particles inside the wood matrix, the samples were cut in half and pH measurements were carried out on the external region and at 5cm from the

surface. The pH values and the weight variation of the samples after the treatment are indicated in table 4.3.

Deacidification					
Samples name	Initial ext pH	pH ext	pH int	ΔW %	Applied dispersion
Pinc_II_Ca	4.0	9.8	6.8	+0.9%	Calcium hydroxide in 2-propanol 1g/L
Pinc_II_Mg	4.0	8.6	7.7	+0.8%	Magnesium hydroxide in 2-propanol 1g/L

Table 4.3. Weight and pH of the samples after the deacidification.

Both of the deacidification treatments were efficient in the neutralization of the wood acidity; in particular, higher pH values were recorded on the external region, probably due to the deposition of particles on the surfaces. As a matter of fact, a whitening of the surfaces was observed after the deacidification. Magnesium hydroxide particles, that are smaller than calcium hydroxide's ones, better penetrated inside the wood, as can be seen from the pH values measured at 5cm from the surface. The slight increase of samples weight after the treatment is ascribed to the presence of particles; in this regard, it should be underlined that no solubilization phenomena took place during the prolonged immersion in 2-propanol.

4.3.3 Stone restoration

The old hospital Sforzesco Ca' Granda is a building characterized by a large use of Angera stone, a dolostone with a particular lamellar structure of dolomite crystals ($MgCa(CO_3)_2$). The worst degradation phenomenon is the flaking that could arise by the lamellar structure, although it is possible that it was caused by the mineral clay (mainly present in the pink and the yellow form).

A dispersion containing calcium and magnesium hydroxide (4:1) was used to consolidate this stone before the reconstruction with lime and plaster. The Angera stone after the treatment was cohesive and ready to be plastered. During the dispersion application the stone changed its color but after the solvent evaporated no color alteration was observed. In figure 4.21 we show an example of Angera stone plastering: the reconstruction of *balaustrini* was performed after the nanoparticles dispersion.

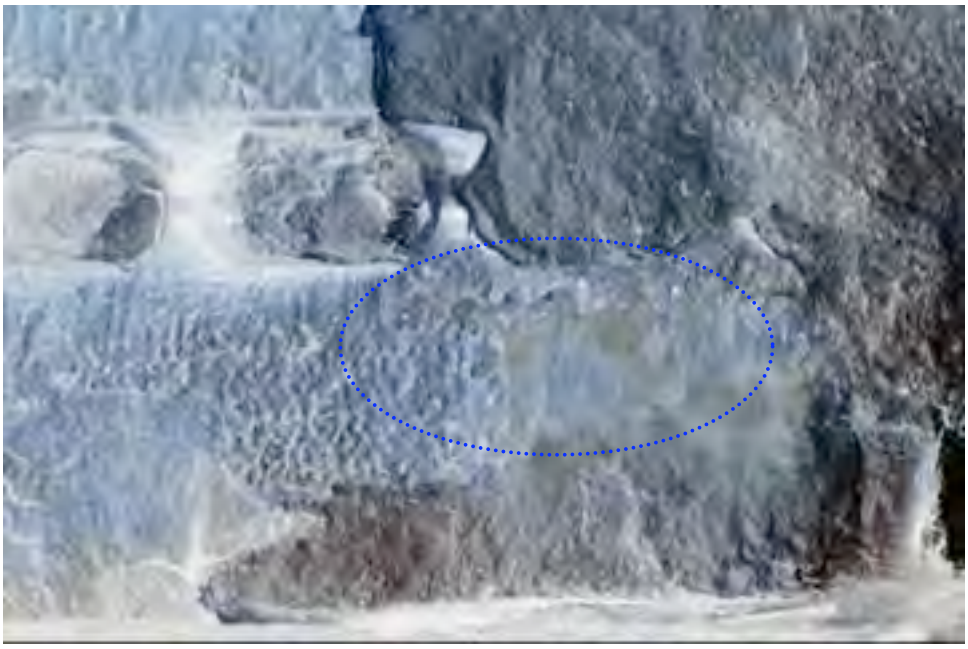

Figure 4.20. The treatment with nanoparticles of calcium and magnesium hydroxide: the dispersion was applied by means of a brush, protecting the surface with Japanese paper sheets.

Figure 4.21. The treatment with nanoparticles of calcium and magnesium hydroxide semplified the plastering of *balaustrini* of Angera stone.

4.3.4 Fresco consolidation

Mexican conservators opted for inorganic materials compatible with the artifact to be preserved in *"La Antigua Ciudad Maya de Calakmul"*, a UNESCO World Heritage Site since 2002 (Campeche, Mexico). In particular, they chose preventive treatments of the Calakmul paintings with a mix of $Ca(OH)_2$ and $Ba(OH)_2$ nanoparticle dispersions.

Figure 4.22. *Estructura 1-4* situated in the acropolis of Calakmul (MEXICO) on the left and a *fresco* contained inside of it.

Compatibility of treatment relies on the application of materials whose physico-chemical characteristics are very similar, and possibly identical, to those of the original material. Hence, the effects of possible degradation processes can be homogeneously distributed throughout the whole material, without any localized stress. In other words, the restoration materials behave as the original and this ensure the lack of physico-chemical and mechanical discontinuities between the layered structures of the wall painting.

4.4 References

[1] H. Hoffmann, Solid/Liquid Dispersions. Edited byTh. F. Tadros. Academic Press, London 1987. xii, 331 pp., Angew. Chem. 101 (1989) 545-546.

[2] P. Patnaik, Handbook of inorganic chemicals, McGraw-Hill, New York, 2003.

[3] L.A. Cosgrove, P.E. Snyder, Berillium oxide, J. Am. Chem. Soc. 75 (1953) 3102-3103.

[4] I. Brink, C. Holley, The enthalpy of formation of strontium monoxide1, The Journal of Chemical Thermodynamics. 10 (1978) 259-266.

[5] R. Konings, E. Cordfunke, W. Ouweltjes, The standard enthalpies of formation of hydroxides I. The alkaline-earth hydroxides β-$Ba(OH)_2$ and $Sr(OH)_2$, The Journal of Chemical Thermodynamics. 20 (1988) 989-992.

[6] R. Giorgi, L. Dei, P. Baglioni, A New Method for Consolidating Wall Paintings Based on Dispersions of Lime in Alcohol, Studies in Conservation. 45 (2000) 154-161.

[7] A. Nanni, L. Dei, $Ca(OH)_2$ Nanoparticles from W/O Microemulsions, Langmuir. 19 (2003) 933-938.

[8] R. Giorgi, L. Dei, M. Ceccato, C. Schettino, P. Baglioni, Nanotechnologies for Conservation of Cultural Heritage: Paper and Canvas Deacidification, Langmuir. 18 (2002) 8198-8203.

[9] V. Daniele, G. Taglieri, Nanolime suspensions applied on natural lithotypes: The influence of concentration and residual water content on carbonatation process and on treatment effectiveness, Journal of Cultural Heritage. 11 (2010) 102-106.

[10] M. Ambrosi, L. Dei, R. Giorgi, C. Neto, P. Baglioni, Stable dispersions of $Ca(OH)_2$ in aliphatic alcohols: properties and application in cultural heritage conservation, in: Trends in Colloid and Interface Science XV, Springer Berlin / Heidelberg, 2001: pagg. 68-72.

Chapter 5 – Conclusions and Perspectives

Synthesis, characterization, application and technological development are embedded throughout this work, entwining with each other in every chapter of the thesis and letting the importance of nanoparticles emerge both for future progress and for the preservation of ancient artifacts. In fact, part of this thesis is focused on the development of new materials, i.e. composites of nanoparticles in a polyamidic matrix, and part on the degradation of cultural heritage, i.e. on developing nanoparticle dispersions able to slow it down and, in many cases, to permanently stop it.

5.1 Nanocomposite developments

We successfully produced three new nanocomposite materials, and we analyzed their thermal, mechanical, chemical, optic and electric properties.

5.1.1 Nylon-6 with copper nanoparticles

A novel composite of nylon-6 with copper nanoparticles was produced. From a TEM microscopic study, we detected the homogeneous dispersion of this material. No cluster of nanoparticles was present in the composite, and this feature increased its Young module, even if only a small amount of filler was used. This aspect is very important for preserving the material from nano- and micro-metric defects. The syntheses reported in the literature had low yields because of the difficulties in handling the copper nanoparticles. During the purification step, in fact, there is the possibility that the nanoparticle surface is oxidized by atmospheric oxygen: copper nanoparticles in fact are highly reactive with oxygen. The novel synthetic method and purification that we developed allowed us to produce 20 g of material each time. After a few improvements we made a preliminary scale-up of the synthesis, producing 25 g of copper nanoparticles. We used it to produce 500 g of composite, a substantial amount for a laboratory scale,

slightly lower than a pilot plant one. The in-situ synthetic route represents an extremely effective method to produce a material with high dispersion homogeneity. Moreover, the synthesis allowed us to obtain a product with a narrow size distribution. Both the TEM analysis and the thermal conductivity measurements at low temperature (from 400 mK to 30 K) confirmed the high degree of nanoparticle monodispersity. Low-temperature measurements showed an atypical sharp dip of the thermal conductivity at 1.4 K which can be interpreted as a resonant scattering of phonons by copper nanoparticles. In fact, we developed a simple model that is in agreement with the experimental results. From analysis of the Small Angle X-Ray Scattering curve with a sphere fitting function, the mean diameter of copper nanoparticles was 8 nm (also confirmed by the TEM images). When we introduced this value in our theoretical model, we were able to predict the same temperature of 1.4 K, at which the phonons were scattered experimentally.
The crystal structure of the polymer is highly affected by the nanoparticles: their surface promotes the formation of γ-phase crystallites instead of the more common α-phase of the nylon-6. With a scale-up of the copper nanoparticle synthesis, it would be possible to increase the concentration of the filler, and this would allow us to examine the thermal and electrical properties by performing further analyses. This is definitely one of the future perspectives of this work.

We have tried to coat the nanoparticle surface with a silica shell to avoid oxidation. In fact it was demonstrated (and we confirmed it) that the silica does not allow oxygen permeation, shielding the metallic surface of the nanoparticles. A nanocomposite material must have a high dispersion homogeneity otherwise the material behavior is the same of a common composite. But a synthetic problem arose during the silica shell formation: in this step in fact, the nanoparticles must be separated from each other, since the shell has to be created around each single particle. If the shell is formed over a cluster, the nanoparticles are irreversibly stuck together and therefore not dispersible in a polymeric matrix anymore. Unfortunately, we still have not found a dispersing agent with suitable characteristics in order to avoid the copper nanoparticle aggregation.

5.1.2 Nylon-6 with zinc oxide nanoparticles

The mechanical properties of nylon-6 were improved also by using zinc oxide nanoparticles. We have examined some synthetic routes reported in

the literature and reproduced the best one, the one that was more appropriate for our aim and that had a conspicuous yield. We carried on a TEM study of the composite material: the material was homogeneous and this was probably due to the pre-activation of the nanoparticle surface with 2-propanol. During this step, the particle surface charge increases and the resulting electrostatic repulsion between the nanoparticles during the polymerization step leads to a more homogeneous material. The elected synthesis of zinc oxide nanoparticles led to a broad distribution size. We chose it in order to fill the polymer enough to modify the thermal properties other than the mechanical ones. Unfortunately, a scale-up of the synthesis would be again necessary to increase the production of zinc oxide and to perform a thermal analysis. This is another future perspective of this work.

5.1.3 Nylon-6 with cobalt ferrite magnetic nanoparticles

Finally, regarding the synthesis of new nanocomposite nylon-6 materials, we successfully synthesized 20 g of cobalt ferrite nanoparticles (with size above 20 nm) and dispersed them in 380 g of ε-caprolactam polymerizing at high temperature and pressure. This material stimulates great interest because of hyperthermic effect of the nanoparticles when an alternate magnetic field is applied. In fact, the glass transition temperature of nylon-6 (50 °C) can be reached with a magnetic field at high frequency in short time, tuning the mechanical properties of the material. Moreover, by applying a strong magnetic field during the cooling of the molten polymer, it is possible to make the material mechanically anisotropic by orienting the nanoparticles. As in the previous cases, we should increase the amount of nanoparticles with a scale-up of their synthesis with a pilot plant.

5.2 Cultural heritage “nano”restoration

As mentioned above, we have developed nanoparticles dispersions for cultural heritage preservation and restoration. In particular, four kinds of artifacts the quality of which was threatened by degradation were examined: *frescos,* paper objects, stone artworks and archeological wood.

5.2.1 Wall paintings consolidation

Calcium and barium hydroxide nanoparticles were used for the *frescos* consolidation. The nanoparticles were dispersed in four different short chain aliphatic alcohols. The application was performed in the *estructura 4* of the archaeological site of Calakmul in Mexico. Regarding the barium hydroxide dispersions, the solvents chosen as dispersing agents were ethanol, 1-propanol, 2-propanol and 1-butanol. In the 1-propanol case, a tixotropic gel was obtained, i.e. a fluid with a non-newtonian behavior that shows a time-dependent change in viscosity; the longer the fluid undergoes shear stress, the lower its viscosity. SAXS and DLS characterization and SEM analysis showed how these dispersions are suitable for wall painting consolidation. The calcium hydroxide instead was successfully dispersed in 2-propanol: a suitable amount of slaked lime, i.e. the paste produced by hydration of calcium oxide, was sonicated into the alcohol. Previous to the dispersion, the slaked lime underwent a hydrothermal treatment to reduce the calcium hydroxide particle size. The most effective treatment for the frescos consolidation seems to be the one with hybrid dispersions of calcium and barium hydroxide. In fact, after the removal of nitrates with a water compress and of sulphates with an ammonium carbonate solution (Ferroni-Dini's method), the calcium hydroxide guarantees a high compatibility with the carbonate matrix of the wall painting and the barium one reduces the mechanical stress due to the transformation of the carbonate in sulphate. When the calcium carbonate (calcite, cell volume 173 $Å^3$) transforms into calcium sulphate (selenite, cell volume 343 $Å^3$) its volume doubles causing a swelling in the paint layer which damages the image. The barium sulphate cell volume is similar to the barium carbonate one (just a 14% increase), thus the mechanical stress is considerably reduced. Moreover, the barium sulphate is more insoluble than the calcium one, and this assures an improvement on the water resistance of the wall painting.

Both the calcium and the barium hydroxide thus assure a paint layer consolidation through the carbonatation reaction. The nanoparticles penetrate through the wall painting pores re-increasing the cohesion of the material. They are linked to the carbonatic matrix through the reaction with carbon dioxide.

5.2.2 Stone artworks restoration

Also the stone artworks site in the Ca' Grande of Milano were restored in part with these dispersions. The Angera stone, a stone with dolomitic composition, undergoes slow erosion: with a nanoparticle treatment the stone can be restored. Calcium and magnesium carbonates are the most predominant constituents, thus the dispersions were prepared with the respective hydroxides suitably dispersed in 2-propanol in the same proportions of the Angera stone. Magnesium hydroxide was synthesized both through the oxide hydration (with water, with molar potassium hydroxide solution or with molar potassium nitrate solution) and via various homogeneous co-precipitation between magnesium chloride and sodium hydroxide solutions. All the samples were characterized by DLS analysis. Particles synthesized with KOH 1M quenching and cationic excess in homogeneous phase were the most suitable for these two synthetic methods, both because they were more monodispersed and because the size of the particles was smaller.

5.2.3 Paper objects deacidification

We believe that, regarding paper treatment, $Mg(OH)_2$ is the most suitable among the four hydroxides we considered. This is because both these nanoparticles are not toxic and, since this hydroxide is the most insoluble among all alkaline earth metal hydroxides we studied, the nanoparticles synthesized by homogeneous co-precipitation are the ones with the smallest size. For the paper objects early the modern ink (i.e. the aniline inks), the nanoparticles that were applied, were dispersed in a alcoholic solvent (2-propanol). For contemporary paper objects instead, it was not possible to use alcohols because they partially or totally dissolve the modern inks, so that smears appear, damaging irremediably the document. Therefore a few perfluoropolyether dispersions, which do not interact with the aniline inks, were prepared. Among all the tested fluorinated solvents, two of them led to best results and among these two, the Galden® HT70 had the best characteristics for the paper application. This is because the boiling point, the latent heat and the viscosity were similar to the 2-propanol ones, elected solvent for this kind of treatment. Paper objects mainly undergo two kinds of serious damages: on the one hand, the acid catalysis of the cellulose depolymerization (in the metal-gallic inks there was a high amount of sulfuric acid), on the other hand the oxidation due to peroxides produced by

the Fenton reaction of the iron ions of the inks. Both these phenomena led to the paper degradation, reducing its mechanical resistance.

Although magnesium hydroxide was a good substance for paper objects restoration, strontium hydroxide also seemed to give good results. The nanoparticles were synthesized both with the homogeneous precipitation method and with a wet milling process (a top-down approach). The commercial strontium hydroxide was milled in 2-propanol by using a T25 Ultra Turrax® homogenizer. This process led to formation both of particles in the nanometric scale and in the submicro- and micro-metric ones. The larger particles were removed by sedimentation to avoid the whitening over the sheet surface.

5.2.4 Archaeological wood preservation

The finding of the Swedish ship Vasa has highlighted the lack of effective conservation technologies in the waterlogged wood field. Initially, the use of polyethylene glycol (PEG), as consolidating and protective agent, avoided the collapse of the structure consequent the water evaporation. However, it started some serious phenomena of degradation related to metal iron components. Moreover, exposing the ship to the atmosphere led to oxidative processes that caused the formation of high amounts of sulfuric acid. As for the paper objects, the acid hydrolyzes the β-1,4-glucopyranosidic bond of the cellulose causing both the decreasing of the degree of polymerization (DP) and a worsening of the resistance to thermal and mechanical stress.
The alcoholic dispersions of calcium and magnesium hydroxide nanoparticles represent a good deacidification method. The small size allows a deep, prolonged and satisfying penetration into the wood pores and reaches inside the log. At this point the nanoparticles react with the acids, avoiding their hydrolyzing action. Moreover an excess of nanoparticles provides an alkaline stock, required to neutralize future production of sulfuric acid.

Publications

Physica B 405 (2010) 4247–4249

Contents lists available at ScienceDirect

Physica B

journal homepage: www.elsevier.com/locate/physb

Low-temperature thermal conductivity of Nylon-6/Cu nanoparticles

V. Martelli [a,b,*], N. Toccafondi [c], G. Ventura [a,d]

[a] INFN, Section of Florence, Via G. Sansone 1, 50019 Sesto Fiorentino, Florence, Italy
[b] LENS, University of Florence, Via Nello Carrara 1, 50019 Sesto Fiorentino, Italy
[c] Department of Chemistry - CSGI, University of Florence, Via Lastruccia 3, 50019 Sesto Fiorentino (Florence), Italy
[d] Department of Physics, University of Florence, Via G. Sansone 1, 50019 Sesto Fiorentino, Florence, Italy

ARTICLE INFO

Article history:
Received 12 January 2010
Received in revised form
1 June 2010
Accepted 14 June 2010

Keywords:
Nano-composite polymer
Low-temperature thermal conductivity
Phonon scattering

ABSTRACT

We have produced a new nanocomposite material made up of a Nylon-6 matrix in which metallic copper nanoparticles (5% in weight) are uniformly dispersed. Here we report about the measurement of the thermal conductivity of such material between 0.1 and 30 K. Thermal conductivity of the nanocomposite does not substantially differ from that of Nylon. Nevertheless data show interesting features, in particular a sharp dip at 1.6 K which can be interpreted as a resonant scattering of phonons by copper nanoparticles.

1. Introduction

We have manufactured a new nanocomposite material made up of a Nylon-6 matrix in which metallic copper nanoparticles (5% in weight) are uniformly dispersed.

The copper nanoparticles were synthesized by the method reported in the work by Wu and Chen [1]. The anhydrous particles were added to melted ε-caprolactam and polymerized to give a composite at 5% w/w. The temperature of polymerization was 260 °C. After washing with water at 90 °C, the material was melted under high vacuum, to avoid the oxidation both of the Nylon-6 and of the copper; a cylindrical sample was obtained. Starting from TEM (transmission electron microscopy) images and SAXS (small-angle X-ray scattering) profile we know that copper nanoparticles are highly monodisperse. Fitting SAXS curve we found an average nanoparticle diameter of ~8 nm.

We are now investigating the physical properties of this new material. In this paper we report about its thermal conductivity in the 0.1–30 K temperature range.

Low temperature thermal conductivity of pure Nylon has been measured by several authors:

- in 100–800 mK range by Anderson et al. [2];
- between 150 mK and 4 K by Scott et al. [3];
- between 1.4 and 20 K by Reese et al. [4].

There is a substantial agreement among data of Refs. [2–4]. Moreover NIST suggests a formula for the thermal conductivity of pure Nylon between 4 and 300 K [5].

2. Experimental technique and measurements

The thermal conductivity was measured over two temperature ranges (below and above 3 K) in different cryostats (dilution refrigerator and pulse-tube cryostat), using the same sample. The experimental arrangement is shown in Fig. 1. The thermal contact at each end of the sample was made by a copper cup which was a tight fit around the sample at room temperature, and by a 4 mm copper screw which was screwed into the sample. We do not know the thermal contraction of Nylon-6/Cu below room temperature. It is likely that, due to the small quantity of added Cu, the material contracts more than copper as it is cooled to cryogenic temperatures. However, good thermal contact is assured in any case by this scheme: even if Nylon-6/Cu should contract less, the cup will contract around the sample.

SMD (surface mount device) NiCr heaters were used to heat the sample. The sample had a thermometer mounted at both ends. In the high temperature range we used Cernox thermometers, while in the low temperature range RuO_2 thermometers were used.

The heaters and thermometers were mounted on the copper blocks. The electrical connections to the heaters and to the thermometers were made with 25 μm NbTi wires.

* Corresponding author at: INFN, Section of Florence, Via G. Sansone 1, 50019 Sesto Fiorentino, Florence, Italy. Tel.: +39 055 4572005; fax: +39 055 4572121.
E-mail address: martelli@fi.infn.it (V. Martelli).

0921-4526/$ - see front matter © 2010 Elsevier B.V. All rights reserved.
doi:10.1016/j.physb.2010.06.031

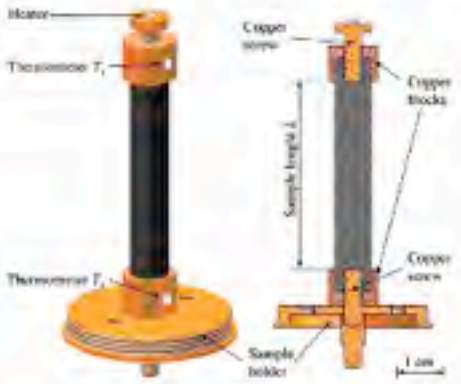

Fig. 1. Experimental setup.

The thermometers were calibrated by means of an SRD 1000 (Superconductive Reference Device) and a NBS SRM 767a fixed point device [6–8] in the lower temperature range. For the higher temperature range we used a commercial secondary calibrated thermometer, with an expected accuracy of 1%. The latter was checked at the following temperatures (boiling points were corrected for pressure dependence):

- 4.3 K: Helium boiling point;
- 9.21 K: Niobium transition in the SRM 767a fixed point device;
- 77.35 K: Nitrogen boiling point.

All thermometers were measured with AVS 47 AC resistance bridges. The sample was a cylinder with effective length (i.e. the length over which the temperature gradients were measured) $L = (44.85 \pm 0.05)$ mm, radius $r = (5.51 \pm 0.02)$ mm and geometrical factor $g = A/L = (2.13 \pm 0.02)$ mm (where A is the section of the sample).

2.1. Low temperature measurements

For the measurements below 3 K, the copper block at the bottom of the sample was screwed into a copper sample holder in thermal contact with the mixing chamber of a conventional liquid helium cooled dilution refrigerator. A copper shield, in thermal contact with the mixing chamber of the dilution refrigerator, surrounded the experiment. Power for the heater was supplied with a four wire I–V source meter (Keithley 2604). The NbTi wires leading to the heater and thermometers were electrically connected by tiny crimped Cu tubes. At the ends of the NbTi wires a four lead connection was adopted.

The thermal conductivity was measured by the longitudinal steady heat flow method. A known power P was supplied to one end of the sample to establish a difference of temperature $T_1 - T_2$ along the sample. The thermal conductivity, $k(T)$ was obtained by differentiation of the integrated power (at constant T_2),

$$P(T_1) = \frac{A}{L}\int_{T_2}^{T_1} k(T)\,dT \qquad (1)$$

where A and L are the sample section and length respectively.

2.2. High temperature measurements

The measurements above 3 K were made in a cryostat based around a pulse tube cooler. The pressure in the vacuum vessel was maintained at about 10^{-4} Pa. As with the low temperature range, the thermal conductivity was measured by a steady state technique. However, instead of mounting the sample directly onto the cold head of the cooler, it was fixed on a copper platform whose temperature could be controlled by a heater.

The thermal conductivity was evaluated by the same method used for the low temperature range described in Section 2.1.

There are three main contributions to the relative error in $k(T)$:

- the power supplied to the sample: we estimate that the relative error of P is of the order of 0.1%;
- the measurement of the geometrical factor $g = A/L$. The error in the measurements of g is estimated to be less than 1%;
- the uncertainty in the temperature, dT, due to the accuracy of the thermometers in this temperature range. A conservative value of $|dT|/T$ is $\sim 2\%$ for $T > 1$ K and $\sim 1\%$ for $T < 1$ K.

Taking into account these contributions, the maximum relative error in $k(T)$ is 3%.

3. Results and discussion

The measured conductivity $k(T)$ is shown in Fig. 2. The measurements made in the two temperature ranges appear to be in good agreement. In Fig. 2 the thermal conductivity data of pure Nylon are reported: we carried out exactly the same measurement with the epoxy (Nylon-6) not filled with the Cu nanoparticles to rule out any possible error leading to the gap. Also data from Ref. [3] and values suggested by NIST [5] are reported for the sake of comparison.

Although nanoparticles may act as nucleation centres for the formation of additional (besides crystallinity of pure Nylon) crystalline zones, the total crystallinity compared to that of pure material is unchanged; in fact (see in Fig. 2), above 4 K, the two curves have the same slope (the slope should change with the degree of crystallinity [9]). On the other hand, from Fig. 2 we immediately see that below 500 mK the material conductivity appreciably differs from that of pure Nylon. We shall now give a qualitative interpretation of this fact. We can evaluate the dimension of the inclusions which produce additional scattering

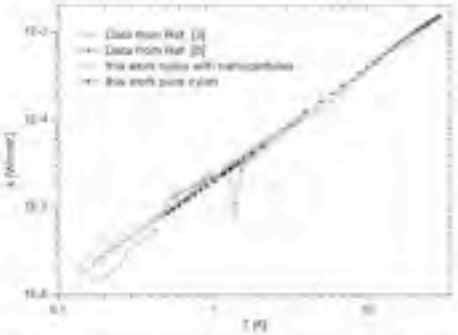

Fig. 2. Low temperature thermal conductivity of Nylon-6/Cu compared to pure nylon. Scott's data [3] and NIST suggested values are also reported [5].

processes leading to a reduced conductivity. Using the dominant phonon wavelength [10] for Nylon at 450 mK, we find that inclusion size is ~60 nm, that is the size for crystallites in pure material. Therefore, since the scattering regions have the same dimensions and volume percentage of pure Nylon, this different behaviour must be ascribed to the thermal contact resistance between Nylon and metallic nanoparticles: the thermal resistance is larger because it depends on the acoustic ratio between the two media [11].

The dip in thermal conductivity at ~1.4 K may be interpreted as a resonant scattering of phonons by Cu nanoparticles. We shall describe their motion using the 'elastic-string' model, that has been used also to describe the motion of dislocations in crystals [12].

Let us schematize nanoparticles as Cu strings, with blocked ends, in the hypothesis of only longitudinal deformation. The equation describing this vibration process is

$$\frac{\partial^2 u}{\partial x^2} - \frac{1}{c^2}\frac{\partial^2 u}{\partial t^2} = 0 \tag{2}$$

where u is the displacement from the equilibrium position, $c^2 = E/\rho$ with E longitudinal elastic modulus (Young modulus) and ρ is the (Cu) density. The main frequency resonance is

$$\nu_0 = \frac{1}{2L}\sqrt{\frac{E}{\rho}} \tag{3}$$

where L is the string-length. In case of tangential strain the shear modulus G must be used.

Of course, nanoparticles have not the shape of a string and we shall use a mean modulus M between E and G [$G = E/[1+\sigma$ with σ = Poisson ratio]:

$$M = \frac{E+G}{2} = \frac{E}{2}\frac{3+2\nu}{2(1+\nu)} \tag{4}$$

Assuming $E = 120$ GPa (for copper E is between 105 and 150 GPa and $\nu = 0.34$) we obtain $M = 82.5$ GPa.

Hence we can calculate the temperature T at which phonon frequency equals nanoparticle resonant frequency:

$$T = \frac{\hbar\nu}{k_B} = \frac{\hbar}{2L}\sqrt{\frac{M}{\rho}}\frac{1}{k_B} = 1.44\,\mathrm{K} \tag{5}$$

where $L = 8$ nm is the peak of size distribution measured by SAXS method. Note that minimum of measured k is just at 1.4 K.

Even if a similar resonant scattering of phonons by crystal-dislocation has been reported for superconductors [13], the anomalous behaviour like that around 1.4 K of fig. 2 was never observed before for nanoparticles embedded in a polymer.

References

[1] S. Wu, D. Chen, Journal of Colloid and Interface Science 273 (2004) 165.
[2] A.C. Anderson, W. Reese, J.W. Wheatley, The Review of Scientific Instrument 34 (1963) 1386.
[3] T.A. Scott, et al., Journal of Applied Physics 44 (1973) 1212.
[4] W. Reese, J.E. Tucker, The Journal of Chemical Physics 43 (1965) 105.
[5] E.D. Marquardt, J.P. Le, R. Radebaugh, Cryogenic material properties database, in: Presented at the 11th International Cryocooler Conference, Keystone, Co., June 20–22, 2000.
[6] W. Resch, et al., in: B. Pellmuth et al. (Eds.), Proceedings of the TEMPMEKO, VDE Verlag, Berlin, 2001, p. 397.
[7] S. Schütt, et al., Journal of Low Temperature Physics (2005) 136.
[8] J.F. Schooley, R.J. Soulen Jr., G.A. Evans Jr., Standard reference materials: preparation and use of superconductive fixed point devices, SRM 767, National Bureau of Standards, Boulder, CO, 1972. SRS Special Publication 260-44. U.S. Govt. Printing Office, Washington, DC.
[9] D. Greig, M.S. Sahota, Journal of Physics C: Solid State Phys. 16 (1983) 1933.
[10] T. Elkinos, R.O. Pohl, Physical Review B: Condensed Matter and Materials Physics 36 (1987) 6051.
[11] W.A. Little, Canadian Journal of Physics 37 (1959) 334.
[12] A. Granato, Physical Review 111 (1958) 740.
[13] A.C. O'Hara, A.C. Anderson, Physical Review B 10 (1974) 574.

CHEMISTRY
A EUROPEAN JOURNAL

DOI: 10.1002/chem.201001443

3rd EuCheMS Chemistry Congress

Nanoparticles for Cultural Heritage Conservation: Calcium and Barium Hydroxide Nanoparticles for Wall Painting Consolidation

Rodorico Giorgi, Moira Ambrosi, Nicola Toccafondi, and Piero Baglioni*[a]

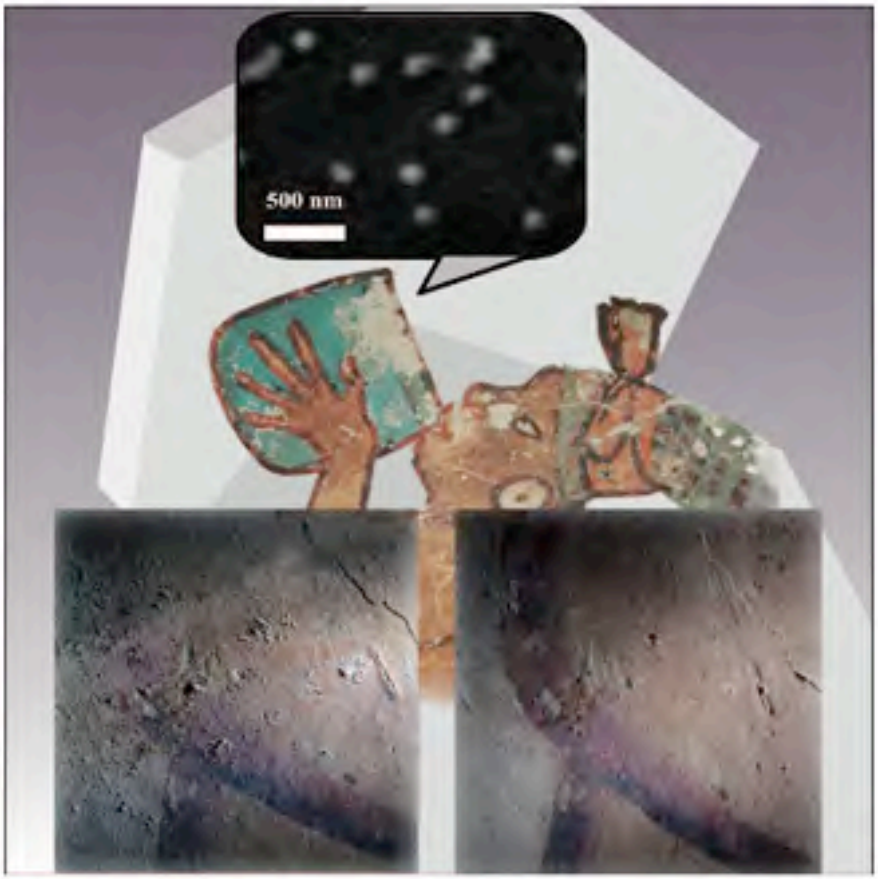

CONCEPT

Abstract: Nanotechnology provides new concepts and materials for the consolidation and protection of wall paintings. In particular, humble calcium and barium hydroxide nanoparticles offer a versatile and highly efficient tool to combat the main degradation processes altering wall paintings. Clear example of the efficacy and potentiality of nanotechnology is represented by the conservation in situ of Maya wall paintings in the archaeological area in Calakmul (Mexico).

Keywords: barium · calcium · conservation · hydroxides · nanoparticles · nanotechnology · restoration

Introduction

Historically, lime has been used by all the civilizations in every age and geographical area. Although it is not clear exactly when use of lime in mortars began, ancient examples have been found in the east Mediterranean area. One of the earliest documented uses of lime as a construction material dates back to 4000 BC, when Egyptians used it for plastering the pyramids.[1] This technology was used in the classical age by Greeks and Romans (Vitruvius provided basic guidelines for lime mortar usage in his treatise *De architectura*), by Mesoamericans in the Precolumbian age, and it was largely diffused in the Middle and Far East throughout the centuries.

The burning of limestone produces, through thermal decomposition of the material and elimination of carbon dioxide, porous lumps of calcium oxide known as quicklime. These lumps react with water to form calcium hydroxide (lime slaking) as dry lime powder or lime putty, depending on the amount of water used.[2] The mixing of hydrated lime with an aggregate (usually sand) and more water forms mortar. The aggregate is necessary to avoid cracks that form upon drying; moreover, it imparts hardness to the mortar and favours the formation of porosity. The final hardening and mechanical strength of the mortar are due to the carbonation process of calcium hydroxide, which reacts with carbon dioxide dissolved in water to form calcium carbonate.

Hydraulic limes partly replaced ordinary lime mortars from the middle of the eighteenth century, the latter were completely abandoned with the development of Portland cement (patented by Joseph Aspdin, an English mason/builder, in 1824). This trend was certainly favoured by the well known difficulties associated with the use of lime mortars, such as the long setting times, particularly under very high relative humidity (RH) conditions. Moreover, because of their weak mechanical strength, lime mortars are prone to degradation due to salt crystallisation processes.[3]

A large part of the artistic cultural heritage from the past is related to wall paintings performed on plaster (also named fresco paintings; Scheme 1). Salt contamination in

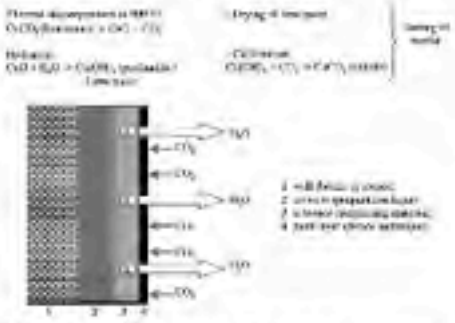

Scheme 1. Schematic representation of the stratigraphy of a wall painting executed by the fresco technique. Pigments are entrapped in the growing calcite originating from the carbonation of lime.

wall paintings is a challenge for their conservation. The paint layer is at the interface between the wall and the surrounding environment and it is strongly susceptible to degradation caused by the mechanical stresses that arise from salt crystallisation, usually occurring at the surface. Salt solutions eventually impregnate the porous network of the wall and move through by capillarity. Crystallisation takes place when the ions' concentration exceeds saturation, often as a result of water evaporation at the interface. This process is generally accompanied by volume expansion; the formation of new crystals inside the pores and/or at the interface between the paint layer and the plaster generates mechanical stresses and results in either lifting and detachment of the paint layer, or cracks and fissuring of the plaster.[3] Sulfates are commonly found as contaminants of wall paintings, since they result from the chemical degradation of calcium carbonate due to acid pollutants. Thus, besides representing a symptom of an already happened chemical degradation process, sulfates favour further deterioration because of the aforementioned mechanical stresses.

The effects of salt crystallisation are usually strongly amplified if any protective coating, possibly applied in previous restoration treatments, is present. Polymers, mainly acrylic and vinyl resins, have been widely used to consolidate wall paintings and to confer protection and hydrorepellency to the painted layer.[4] Formulations based on acrylate/meth-

[a] Dr. R. Giorgi, Dr. M. Ambrosi, Dr. N. Toccafondi, Prof. P. Baglioni
Department of Chemistry & CSGI
University of Florence
via della Lastruccia 3-50019 (Italy)
Fax: (+) 0554573372
E-mail: baglioni@csgi.unifi.it

acrylic and acrylate/vinylacetate co-polymers have been extensively used for decades; unfortunately they threaten the survival itself of works of art and they can now be considered as one of the most dangerous sources of degradation. In the presence of polymer film, salt crystallisation processes involve deeper areas, with stronger de-cohesion, until the complete powdering of the painting. The polymer closes the surface pores, generating mechanical stresses towards the paint layer. These polymers have been considered perfectly reversible materials for a long time. Unfortunately, their reversibility, that is, the possibility to solubilise them by the same solvent used for the application, has been proved to be a *chimera*. In fact, polymer resins degrade quickly with drastic variation of their physicochemical properties. In summary, contrary to the expectations, polymers used for the protection of wall paintings have induced further degradation of the works of art and their chemical modifications, such as cross-linking, strongly hampers their removal.[5]

Concept

For the above reasons, the use of inorganic materials (possibly of the same materials used for the works of art), which are compatible with wall paintings, minimises the aforementioned risks and prevents unexpected side effects. Inorganic consolidants are highly chemically stable and preserve the wall painting porosity, so ensuring long-lasting consolidation effects.

With the aim of solving the problem of the degradation of wall paintings caused by the presence of sulfates and to achieve a good consolidation, in the mid-seventies Enzo Ferroni developed a conservation treatment based on the application of ammonium carbonate and barium hydroxide solutions. This methodology was used for the first time during the restoration of wall paintings by Beato Angelico in Florence.[7]

The Ferroni method involves the application of ammonium carbonate and barium hydroxide in a two-step procedure [Eq. (1)–(2)]. Ammonium carbonate changes gypsum into soluble ammonium sulfate, which is mostly absorbed by the cellulose poultice usually used for the application of the ammonium carbonate solution [Eq. (1)]. The subsequent application of an excess of barium hydroxide leads to a viable consolidation effect [Eq. (3)–(5)], thanks to the formation of barium carbonate [Eq. (3)] and the re-generation of calcium hydroxide [Eq. (4)], through a double-exchange reaction with calcium carbonate.

$$(NH_4)_2CO_3 + CaSO_4 \cdot 2H_2O \rightarrow (NH_4)_2SO_4 + CaCO_3 + 2H_2O \quad (1)$$

$$(NH_4)_2SO_4 + Ba(OH)_2 \rightarrow BaSO_4 + 2NH_3 + 2H_2O \quad (2)$$

$$Ba(OH)_2 + CO_2 \rightarrow BaCO_3 + H_2O \quad (3)$$

$$Ba(OH)_2 + CaCO_3 \rightarrow Ca(OH)_2 + BaCO_3 \quad (4)$$

$$Ca(OH)_2 + CO_2 \rightarrow CaCO_3 + H_2O \quad (5)$$

This "new" lime undergoes a slow carbonation reaction that enhances the mechanical strengthening of the paintings. Part of the applied barium hydroxide completes the transformation of gypsum, forming insoluble barium sulfate.

Unfortunately, at that time, the methodology was strongly averted by restorers who were confident of the use of polymer resins, mainly for the easy and fast application procedure. Indeed, this simple consolidation procedure, known as Ferroni or Florentine method, presents a twofold advantage, since it simultaneously provides the consolidation of wall paintings and a substantial removal of gypsum.

Although calcium hydroxide is one of the most ancient and widely used building materials, its application as consolidation agent of wall paintings is insignificant.[8] There is no doubt that lime ensures the highest physicochemical compatibility with the work of art and it should be preferred when degradation results from loss of calcium carbonate. Nevertheless, the low solubility of calcium hydroxide in water (about 1 g L^{-1}) has hindered its use for years. Saturated solutions (lime-water) have been used only in a few specific cases. Alternatively, application of lime dispersions is hampered by the possible veil formation (due to the calcium hydroxide reaction with carbon dioxide) on the treated surfaces. Whitening could be overcome by using alcoholic dispersions of very tiny particles, with size lower than that of surface pores, which are in the range of micrometers.[9]

Dry Hydrate Lime and Lime Putty

The slaking of quicklime (also known as hydration process) is the most common and cheapest method to prepare $Ca(OH)_2$ powder. By mixing one part by weight of CaO with about 0.5–0.75 part of water, a dry hydrate (i.e. $Ca(OH)_2$ powder) is obtained. Due to the high temperature developed during hydration, amounts of water slightly higher than the theoretical one are usually required to reach a complete hydration.[10] On the other hand, the slaking with an excess of water produces a lime putty. The latter is characterised by finer particles and, therefore, a higher surface area, which confers a higher reactivity and plasticity to the putty than the dry hydrate. Lime putty contains chemically bound water and about 30–40% *w/w* of free water surrounding hydrate colloids.[11] It has been shown that free water prevents particles' spontaneous aggregation, by acting as a lubricating agent.[12]

It is not easy to define the best hydration parameters tailored to the final characteristics of powder and/or colloids. It is known that both large excess or insufficient amounts of water (lower than the stoichiometric ratio) produce very poor lime. In the first case, a fast hydration of quicklime lumps leads to the formation of a close surface calcium hydroxide layer, the low porosity of which inhibits further

water diffusion; in the second case, very high temperature is reached locally, which causes the burning of hydrate and its complete dehydration.[10]

Classic historical sources by Pliny and Vitruvius, as well as the Renaissance treatise by Cennino Cennini, report recipes to enhance the slaked lime quality. In particular, a prolonged storage and/or pure water was recommended to reach a complete ripening of lime, which usually requires several months or even years. Practical experience has defined the best aging procedure to improve plasticity and workability of lime putties, however, little is known about mechanisms underlying the observed improvements.

The effect of prolonged storage of lime under water has been recently analysed by Rodriguez-Navarro et al.[11] Crystal morphology and size of calcium hydroxide particles were shown to significantly change upon aging. Over time, prismatic crystals present in fresh lime putty undergo relevant size reduction and convert to sub-micrometer platelike crystals. The higher solubility of the prism faces compared to the basal faces of the hexagonal portlandite was hypothesized as an explanation for the observed prismatic-to-platelike transformation. Secondary nucleation of plate-like nano-sized portlandite crystals was also detected. The higher surface area and the changes in morphology account for the greater water adsorption capability and the resulting greater plasticity, water retention and workability of mortars prepared by aged lime putty.

The carbonation process of lime mortar proceeds through carbon dioxide diffusion followed by a chemical reaction to form calcium carbonate crystals. This process is influenced by several factors, the most important being the environmental humidity, the carbon dioxide concentration and the permeability of the mortar, which controls gas diffusion. The latter is also influenced by the carbonation reaction itself, since formation of calcium carbonate in the outer layer modifies the porosity of the mortar. Ciurlia et al.[12] demonstrated that mortars prepared with aged lime putties showed faster carbonation process compared to mortars containing fresh, commercially available, hydrate lime.

Interestingly, it was observed that once hydrate lime putty is dried, it does not recover its initial properties by re-dispersion in water.[13] Many attempts have been carried out to better understand this irreversibility, due to its important scientific and technological implications, particularly in the field of cultural heritage conservation.

Short-range van der Waals forces are responsible for the attractive interactions that favour clustering of lime colloids. In principle, these forces are not strong enough to inhibit a complete re-dispersion of dry calcium hydroxide. Nevertheless, the original colloidal domain cannot be recovered even through vigorous stirring. This behaviour was elucidated by Rodriguez-Navarro et al.,[11] who concluded that the irreversible colloidal behaviour of hydrate lime results from an aggregation mechanism involving an oriented (epitaxial) stacking of nano-sized platelike $Ca(OH)_2$ particles.[14] This aggregation process occurs already in diluted dispersion and, evidently, is becomes dominant during drying.

Therefore, we can conclude that slaked lime is probably one of the oldest nanomaterials known to mankind and that the ideal consolidating agent for wall paintings and limestone should be based on nano-sized crystals with a platelike shape. These characteristics provide a good consolidation and ensure a long-lasting effect.

We synthesized calcium hydroxide in a homogeneous-phase reaction, the simplest way to prepare nano-sized particles with the required platelike morphology.

Synthesis of Calcium Hydroxide Nanoparticles and Preparation of Alcohol Dispersion: An Overview

Nanoparticles of calcium hydroxide have represented a substantial improvement for the conservation of wall painting. The target was the synthesis of particles smaller than 300 nm and their proper dispersion in suitable solvents; thus particles could penetrate the thin painted layer carried by the dispersing solvent.

Calcium hydroxide nanoparticles were synthesized through homogeneous-phase reaction in water and other organic solvents. The size and shape of the particles could be tuned by proper selection of some reaction parameters, as the reaction temperature, the concentration of the reactants and their mole ratio.

Calcium hydroxide nanoparticles were prepared in water at about 90 °C[15] with concentration of the reactants in the range 0.10–0.75 M for Ca^{2+} salts and 0.18–1.50 M for OH^-, spanning molar ratios in the range 1.2–2.0 (cation:anion). This synthetic pathway was modified by Dei et al.[15] using ethylene and propylene glycol as reaction solvents in order to reach higher temperatures (up to 175 °C). Both synthetic routes produced nano-sized crystals of calcium hydroxide with a platelike shape. The average size and particle size distribution showed meaningful differences depending on the synthetic procedure. The synthesis at higher temperatures in glycol produced particles of 30–40 nm, while particles with an average size of 200–300 nm were usually obtained for reaction in water at 90 °C (see Figure 1).

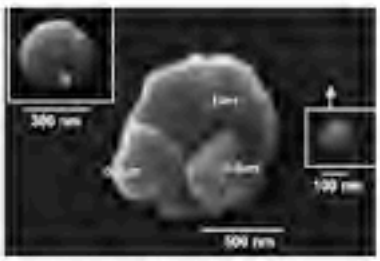

Figure 1. Clusters of calcium hydroxide nanoparticles prepared through a homogeneous phase reaction in water at 90 °C, revealed by means of scanning electron microscopy (SEM).

Calcium hydroxide nanoparticle dispersions were also prepared starting from slaked lime. Heterogeneous-phase reaction of CaO with water produces, under specific conditions, lime putty, which usually has some unreacted CaO in the core of the particles. By using an autoclave system for the control of temperature and pressure, it is possible to force the hydration until a complete slaking of the lime is achieved. In this way, lime putty particles may undergo further fragmentation due to the volume expansion associated to the transformation of CaO to $Ca(OH)_2$, leading to the reduction of the particles size.

Although synthesised particles have both size and size distributions ideal for the application on wall paintings, they cannot be used as a dispersion in water, because of their tendency to aggregate in this solvent. A substantial improvement was achieved by using short chain alcohols as the dispersing media to produce kinetically stable dispersions. In particular, it was shown that 1-propanol and 2-propanol provide a good de-aggregation and stabilisation of the nanoparticles. It was hypothesised that this process occurs because of the physical absorption of alcohols onto the nanoparticles' surfaces, also favoured by the positive electro-kinetic potential of particles themselves. This will be further discussed in the following. Figure 2 shows the particle size distribution of calcium hydroxide nanoparticles' dispersions obtained by dynamic light scattering (DLS) measurements.[7]

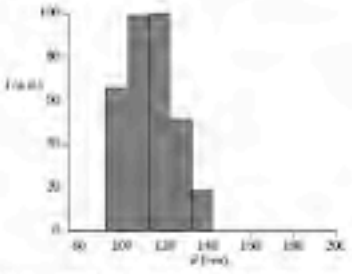

Figure 2. Particle size distribution of calcium hydroxide nanoparticles in 2-propanol, as obtained by DLS.

Co-precipitation reactions produce sodium chloride as a side-product and require time-consuming steps of purification. These are usually performed by dialysis against a lime-water solution. Purification from glycols is slightly more difficult, because of the adsorption of the solvent molecules on the nanoparticles surfaces. It was shown that this adsorption favours aggregation of the synthesised particles and produces micron-sized clusters. Glycol removal is usually achieved by peptisation treatment in an ultrasonic bath by using 2-propanol as washing medium.

The aggregation behaviour of nanoparticles in 2-propanol and ethylene glycol (EG) was investigated by using contrast-variation small-angle neutron scattering (SANS), and small- and wide-angle X-ray scattering (SAXS and WAXS). Nanoparticles aggregate into mass-fractal superstructures upon dispersion in 2-propanol; more compact and larger aggregates are formed when ethylene glycol is used as dispersing medium.

The specific surface area measured at the Porod limit is very high for nanoparticles in 2-propanol ($\approx 200\ m^2 g^{-1}$), almost 30 times that determined in EG ($\approx 7\ m^2 g^{-1}$). These differences depend on the relevant transformations of the surface at a microstructural level, which were demonstrated to arise from competitive solvent adsorption. Contrast-variation SANS analysis suggested that the composition of the first layer of solvent adsorbed onto the nanoparticles is determined by a thermodynamic equilibrium that favours ethylene glycol compared to 2-propanol by 2.4 kJ mol^{-1} with respect to the bulk solvent composition.[7]

As mentioned above, nanoparticles prepared in glycols strongly aggregate to form micrometer-sized clusters, which can be peptised (de-aggregated) by washing with 2-propanol to yield individual nano-sized units. The hexagonal platelike nanoparticles form stacks, as evidenced by the increase of relative intensity of the peak ascribable to basal (001) crystallographic face present in the WAXS profile.[7] SAXS and SANS investigations were also carried out in order to investigate the role of ethylene glycol and 2-propanol adsorption on the stability and compactness of calcium hydroxide nanoparticles' agglomerates. It was shown that de-aggregation actually proceeds through physisorption of 2-propanol molecules onto the particle surface. 2-Propanol and EG present a competitive adsorption on the nanoparticles' surface, showing opposite effects on the aggregation. In EG, nanocrystals are strongly aggregated, forming stacked plates and only micrometer-sized structures are observed. In 2-propanol the individual crystals are resolved by surface adsorption, leading to a stable dispersion; mixtures of the two solvents produce intermediate structures.

Nano-Sized Crystals of Barium Hydroxide as a New Tool for Consolidation of Wall Paintings

When large amounts of soluble sulfates (i.e., sodium or magnesium sulfates) are present in a wall painting, consolidation with calcium hydroxide nanoparticles might not produce durable results. In fact, sulfate ions can react with calcium hydroxide to give a double-exchange reaction [Eq. (6)], producing the slightly soluble gypsum (calcium sulfate dihydrate). The final result is the lack of the consolidation effect. Moreover, re-crystallisation of the newly formed gypsum leads to the formation of a white glaze on the painted surface.

$$Ca(OH)_2 + Na_2SO_4 + 2H_2O \rightarrow CaSO_4 \cdot 2H_2O + 2NaOH \quad (6)$$

Barium hydroxide nanoparticles represent a really useful alternative and a complementary tool to finalize this process.

In fact, $BaSO_4$ is totally insoluble and the aforementioned solubilisation–crystallisation cycles of sulfates are completely inhibited. Barium and calcium hydroxide can be used simultaneously and the thermodynamic equilibrium favours the formation of the less soluble barium sulfate [Eq. (7)]:

$$Ba(OH)_2 + CaSO_4 \cdot 2H_2O \rightarrow BaSO_4 + Ca(OH)_2 + 2H_2O \quad (7)$$

Mixed formulations can be used for the pre-consolidation of surfaces largely contaminated by sulfates, the damage by which is so substantial that they cannot be cleaned without causing loss of material. Nowadays the common practice for the re-consolidation is the use of adhesives, such as calcium oxalate or acryl/vinyl polymers.

Synthesis of nano-sized barium hydroxide following a bottom-up approach is strongly hampered by its solubility in water. Better results were recently achieved through a top-down process. Micron-sized grains of barium hydroxide were dispersed in short-chain alcohols (1-propanol and 2-propanol) at high temperature and pressure, and milled to obtain a strong size reduction from several microns to about 100 nm[11] (Figure 3). Dynamic light scattering shows particles size distributions similar to those obtained for calcium hydroxide (Figure 4).

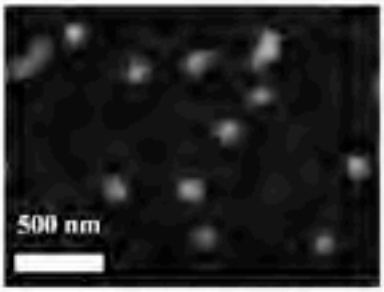

Figure 3. Barium hydroxide nanoparticles observed by means of scanning electron microscopy (SEM).

Both 1-propanol and 2-propanol present the appropriate features as dispersing media for application purposes: they are environmentally friendly, rather volatile and they show low surface tension. Despite their similarities, these solvents behave very differently; in fact, 1-propanol gives more stable dispersions and fast de-aggregation. Aggregation (and re-dispersion) phenomena cause quantifiable changes in particle size distribution, which affects the kinetic stability and other macroscopic properties of the colloidal dispersions.

It was observed that concentrated barium hydroxide dispersions (20–33.3 g L^{-1}) in 1-propanol spontaneously form supramolecular structures that show the typical characteristics of a thixotropic gel. Specific interactions of 1-propanol

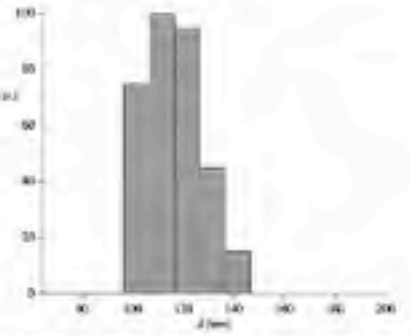

Figure 4. Particle size distribution of barium hydroxide nanoparticles in 1-propanol, as obtained by DLS.

with barium hydroxide nanoparticles were investigated by SAXS.[12] Preliminary results seem to indicate that nanoparticles organise to form threads by stacking, which further assemble into bundles.[13]

1-Propanol dispersions seem to loose their periodical organisation upon dilution and the nanoparticles are completely dispersed within the solvent. Dilute dispersions in 2-propanol are much less stable and particles have a high polydispersity.

It is worthwhile noting that dilution of a 1-propanol gel by 2-propanol does not induce any de-aggregation of the fibril structures previously mentioned, demonstrating the higher affinity of barium hydroxide towards 1-propanol compared to 2-propanol. Thus, unlike calcium hydroxide nanoparticles, which give very kinetically stable dispersions in both 1-propanol and 2-propanol, barium hydroxide shows a peculiar affinity with 1-propanol. This finding suggests that mixed barium and calcium hydroxide formulations in 1-propanol can be used for pre- and consolidation treatments.

An Example of the Nanoparticles Application for the Rescue of Mesoamerican Wall Paintings

La Antigua Ciudad Maya de Calakmul is located in the Campeche state (Mexico), inside the Calakmul Biosphere Reserve, which is an extensive protected area that preserves the typical tropical forest environment of Central America.[14] The city of Calakmul, discovered in the jungle in 1931, was declared a UNESCO World Heritage Site in 2002. Calakmul was, together with Tikal in Guatemala, one of the most important cities of the Classic Maya period (AD 250–800). More than 6000 elements, including buildings, monuments, altars, and stelae (stone or wooden slabs erected for commemorative purposes), have been identified; in particular, the stelae (about 120) represent a precious witness of history, since all the main historical events were recorded as sculpted bas-relief.

Calakmul was inhabited for more than 12 centuries and was slowly abandoned towards the year AD 900 (Post-Classic period). Cyrus Lundell, the botanist who discovered the city, named it Calakmul, which translated from the Maya language means "two (Ca) *clone* (lak) artificial hills or mounds (mul)", taken from the presence of two big pyramids. The urban area of Calakmul occupies a natural dome covering about 25 km^2, surrounded by a lower area, or *bajo*, that collects water during rainy seasons.

The "Proyecto Arqueologico Calakmul" was established in 1993 and it is directed by the archaeologist Ramón Carrasco Vargas. This project involves archaeologists, architects, engineers, conservators and epigraphists, besides other specialists. The University of Florence (CSGI) has been an active partner since 2004, being involved in the study of the painting technique and in the development of nanotechnology for the consolidation and protection of the wall paintings and limestones.

In 2005 an extraordinary painting cycle was discovered inside the Structure I of the "Acropolis Chik Naab"[22] (see Figure 5). These paintings constitute one of the most important documents of the pre-Columbian art history and a rare example of Maya painting from the Early Classic period (250–600 BC). Wall paintings were intentionally entombed by Maya, who used specific materials (stones with a well-defined size and a great number of ceramic fragments) that were applied over a thick foundation layer, made of fine powder of stucco mortar and limestone, put in contact with the painting surfaces. After this step, a successive construction was built on top of the pre-existing building. The deliberate and careful burial of these paintings indicates the intention to preserve them, possibly for some religious reason. Inside Structure I, the mural paintings covered the walls (or steps) of a pyramidal substructure. The squared building has a 10 m base and is 5 m high; it is fully decorated with murals depicting scenes of daily life that can offer insight into Mayan social relationships. This archaeological discovery is extraordinary, because Mayan people, as well as many other civilizations, mostly depicted rulers, deities and religious authorities; paintings describing domestic and craft-made activities of the Maya people have only been found in Calakmul.[22]

Figure 5. Structure I in the Acropolis Chik'Naab in Calakmul (top): mural painting from the Early Classic Maya period, showing (in the step of substructure I in the south-east side of the building (bottom).

The subtropical climate of south Mexico presents a quite high and constant temperature (about 30 °C), independent of the season. The seasons are characterised by a short but really intensive rainy period, with a relative humidity of about 90%. For the most part of the year, relative humidity inside Structure I is very close to saturation conditions; therefore, the surfaces of the paintings are usually slightly wet.

It is clear that excavation and recovery of the paintings led them to the exposure of new environmental conditions (light, temperature and humidity), presenting a real challenge for their conservation. To prevent degradation from these strong environmental variations, the paintings have been protected with the installation of a roof, and the presence of people was reduced to the minimum necessary to perform the delicate excavations and restoration work. Nevertheless, a consolidation treatment was necessary to conserve the paintings and we were involved in the formulation of systems respectful of the physicochemical characteristics of the paintings.

Recent history of conservation in Mexico has definitely shown that interventions based on polymer resins, largely used in the past by European and American conservators in Mexican archaeological sites, are not durable and are usually really detrimental for the survival of paintings (and limestones).[23] These circumstances are common to most of the Mexican archaeological sites. There is evidence that clearly shows how degradation of wall paintings' in Cholula, Cacaxtla, Teotihuacan and Mayapan has been caused by the presence of polymer resin coatings.[24] In the archaeological site of Kohunlich (Quintana Roo state), for example, the severe damage of modelled stucco polychrome masks (flaking and powdering of the surfaces) is the final result of polymers' degradation due to exposure to a tropical climate.[25] Considering that the Biosphere of Calakmul has similar characteristics to that of Kohunlich, a different approach for the conservation of paintings and limestones has been undertaken.

This Mexican conservationists have decided on the use of inorganic materials compatible with the work of art to be preserved and, in particular, they opted for preventive treatments of the Calakmul paintings by nanoparticle dispersions in organic media.

Compatibility relies on the application of materials that possess physicochemical characteristics which are very similar, or possibly identical, to those of the original material. Hence, the effects of possible degradation processes can be homogeneously distributed throughout the whole material, without any localised stress. In other words, the restoration materials behave as the original, which ensures the lack of physicochemical and mechanical discontinuities between the layered structures of the wall painting.

In Calakmul, Maya paintings were treated by using a mixture of calcium and barium hydroxide nanoparticles. A blend of hydroxides was chosen and initially applied, because of the presence of sulfate salts. This formulation, used for consolidation of the wall paintings, was beneficial and led to a good consolidation effect even on wall paintings containing high amounts of salts. A dispersion of 5 g L^{-1} in 1-propanol was applied on the paintings by brushing. Barium hydroxide constituted 20 wt% of the total nanoparticle amount used. The consolidation effect was significant already after one week. Figure 6 shows the effect of the application procedure of nanoparticles on the painted surfaces. The size of the nanoparticles allowed a good penetration without white glaze formation and the results of application are excellent: the paintings are stable and do not show ongoing degradation processes.

Figure 6. Details of the mural paintings reported in Figure 5. Pictures on the left show the presence of sulfates over the surface and flaking phenomena damaging the paint layer; pictures on the right show the same areas six months after the application of a calcium/barium hydroxide nanoparticle mixture.

Summary and Outlook

Nanoscience and nanotechnology are revolutionising material science. The developments of novel tailored nanoparticle-based materials are creating new tools for Conservation Science and constitute the most advanced systems for consolidation of wall paintings.

Humble calcium hydroxide particles can be transformed into a noble material with excellent features as a consolidation agent, when synthesised as a nanomaterial. We have pioneered the use of calcium hydroxide nanoparticles to restore wall paintings, the degradation of which is basically due to the transformation of calcium carbonate into gypsum. Nanoparticles of calcium hydroxide efficiently interact with carbon dioxide to reform calcium carbonate and replace the degraded original ligand, leading to the re-cohesion of the paint layer.

In the presence of large amounts of sulfates, the consolidation effect of calcium hydroxide is boosted by the complementary use of barium hydroxide nanoparticles, which leads to the formation of the totally insoluble, and therefore inert, barium sulfate.

Each formulation requires specific procedures for the synthesis and this concept reports an overview for the preparation of inorganic consolidation materials, which ensure the safe and durable restoration of wall paintings. The application of mixtures of calcium and barium hydroxide nanoparticles to the recently discovered Maya paintings in Calakmul is illustrated.

The examples reported in this Concept article suggest the enormous possibilities that nanoscience opens up for Cultural Heritage conservation, due to the unique properties that the reduction in particle size confers to nanomaterials compared to their micrometric counterparts.

Acknowledgements

The authors wish to thank Ramon Carrasco Vargas director of the "Proyecto Arqueológico Calakmul", María Cordoba Hinojosa head of conservation and restoration in the "Proyecto Arqueológico Calakmul", Diana Magaloni director of the Museo Nacional de Antropología in Mexico City, Lilia Rosete Weber, national coordinator of Cultural Heritage Conservation at the National Institute of Anthropology and History (INHA), and Alfonso de María y Campos, general director of the INHA. Financial support from CSGI is acknowledged.

[1] W. D. Kingery, P. B. Vandiver, M. Prickett, *J. Field Archaeol.* **1988**, *15*, 219; S. Pesenti, G. Tonniolo, G. Torricelli, S. Cerri, M. Hirli, F. Gioffredda, P. Rossi-Doria, A. De Rege, D. Pozzi, P. J. Petrarolha, G. Benedetti in *ICCROM—Cements and Grouts Used in the Conservation of Historic Buildings*, Rome, **2002**, p.61; R. S. Boynton, *Chemistry and Technology of Lime and Limestone*, 2nd ed., Wiley, New York, **1980**.

[2] K. Elert, C. Rodriguez-Navarro, E. S. Pardo, E. Hansen, O. Cazalla, *Stud. Conserv.* **2002**, *47*, 62.
[3] A. Arnold, K. Zehnder, *J. Cryst. Growth* **1989**, *97*, 513; A. Arnold, K. Zehnder in *Proceedings of the 1st International Symposium on Conservation of Monuments in the Mediterranean Basin* (Eds.: F. Zezza), Frato, Brescia, **1989**, p. 31; L. Dei, M. Mauro, P. Baglioni, C. Mengucci, Del Fà, F. Frolini, *Langmuir* **1999**, *15*, 8015; G. W. Scherer, *Cem. Concr. Res.* **2003**, *34*, 1613.
[4] E. Ferroni, P. Baglioni in *Proceedings of the Symposium on Scientific Methodologies Applied to Works of Art – Florence 1984*, Montedison Progetto Cultura, Milano, **1986**, pp.108.
[5] C. Horie in *Materials for Conservation: Organic Consolidants, Adhesives and Coatings*, Butterworth-Heinemann, London, **1987**; P. Mora, L. Mora, P. Philippot in *Conservation of Wall Painting*, Butterworths, London, **1984**.
[6] R. Giorgi, M. Baglioni, D. Berti, P. Baglioni, *Acc. Chem. Res.* **2010**, *43*, 695; P. Baglioni, R. Giorgi, L. Dei, *C. R. Chim.* **2009**, *12*, 61.
[7] P. Baglioni, E. Carretti, L. Dei, R. Giorgi, *Self-Assembly* (Ed.: B. H. Robinson), IOS, Amsterdam, **2003**, pp.32–41; E. Ferroni, V. Malaguzzi-Valeri, G. Rovida in *Proceedings of the ICOM Conference in Amsterdam*, ICOM Committee for Conservation, Paris, **1969**.
[8] P. Baglioni, L. Dei, R. Giorgi, *Stud. Conserv.* **2000**, *45*, 154; I. Brajer, N. Kalsbeek, *Stud. Conserv.* **1999**, *44*, 145.
[9] M. Ambrosi, L. Dei, R. Giorgi, C. Neto, P. Baglioni, *Langmuir* **2001**, *17*, 4251; P. Baglioni, R. Giorgi, *Soft Matter* **2006**, *2*, 293.
[10] M. E. Holmes, G. J. Fink, F. C. Mathers, *Chem. Metal. Eng.* **1922**, *27*, 1212; W. G. Whittman, G. H. B. Davis, *Ind. Eng. Chem.* **1926**, *18*, 118.
[11] D. G. R. Bonnell, *J. Soc. Chem. Ind. London Trans. Commun.* **1934**, *58*, 279; C. R. Navarro, E. Hansen, W. S. Gizell, *J. Am. Ceram. Soc.* **1998**, *3032*; D. R. Moorehead, *Cem. Concr. Res.* **1986**, *16*, 700.
[12] C. Rodriguez-Navarro, E. Ruiz-Agudo, M. Ortega-Huertas, E. Hansen, *Langmuir* **2005**, *21*, 10948.
[13] C. R. Rodriguez-Navarro, E. Hansen, S.W. Gizell, *J. Am. Ceram. Soc.* **1998**, *81*, 3032.
[14] O. Cazalla, C. Rodriguez-Navarro, E. Sebastian, G. Cultrone, M. J. De La Torre, *J. Am. Ceram. Soc.* **2000**, *83*, 1070.
[15] K. W. Ray, F. C. Mathers, *Ind. Eng. Chem.* **1928**, *20*, 475.
[16] R. L. Penn, *J. F. Banfield, Science* **1998**, *281*, 969; R. L. Penn, G. Oskam, T. J. Strathmann, P. C. Searson, A. T. Stone, D. R. Veblen, *J. Phys. Chem. B* **2001**, *105*, 2177.
[17] B. Salvaderi, L. Dei, *Langmuir* **2001**, *17*, 2371.
[18] E. Gabrowsky, I. Morrison in *Measurements of Suspended Particles by QELS*, Wiley-Interscience, New York, **1983**.
[19] E. Frolini, M. G. Page, R. Giorgi, H. Colfen, P. Baglioni, B. Demé, T. Zemb, *Langmuir* **2007**, *23*, 2330.
[20] N. Toccafondi, R. Giorgi, M. Ambrosi, E. Frolini, P. Baglioni, unpublished results.
[21] R. Carrasco, *Maya* (Ed.: G. Ortelli), Rizzoli, New York, **1998**, pp.372–385; R. Carrasco, M. Colón, *Arqueología Mexicana XIII* **2005**, *75*, 40; R. Carrasco Vargas in *The Metropolis of Calakmul, Campeche in Maya Civilization*, **1998**, Thames and Hudson, New York, pp.372–385.
[22] R. Carrasco-Vargas, V. A. Vázquez-Lopez, S. Martín, *Proc. Natl. Acad. Sci. USA* **2009**, *106*, 19245.
[23] H. Orea, V. Magar in *ICOM Committee for Conservation, 13th Triennal Meeting Rio de Janeiro* (Ed.: R. Vontobel), James & James, London, **2002**, pp. 176–182.
[24] D. Magaloni, T. Falcon in *Temas y problemas—I 15th Coloquio del Seminario de Estudio del Patrimonio Artístico* (Eds.: A. T. Molina, E. X. de Anda Alanís), UNAM IIE, Mexico City, **1997**, pp.107–124; I. Torres, G. Pelaez, Cazaulla, *Proyecto de Investigación y Conservación*, INAH, Gobierno del Estado de Tlaxcala, **1990**, pp. 77–87; T. López, V. M. Dávila, *33rd International Symposium on Archaeometry* (Eds.: H. Kars, E. Burken, Vrije Universiteit, Amsterdam, **2002**, p. 189; A. Espinosa, *In situ Archaeological Conservation* (Ed.: H. W. M. Hodges), INAH, Mexico City, **1987**, pp. 84–90.
[25] J. Riederer in *ICOM Committee for Conservation, 7th Triennal Meeting, Copenhagen* (Ed.: D. de Froment), ICOM Committee for Conservation, Paris, **1984**, pp. 21–22.

Published online: July 23, 2010

Langmuir
Article
pubs.acs.org/Langmuir

Hydroxide Nanoparticles for Deacidification and Concomitant Inhibition of Iron-Gall Ink Corrosion of Paper

Giovanna Poggi, Rodorico Giorgi, Nicola Toccafondi, Verena Katzur, and Piero Baglioni*

Department of Chemistry and CSGI, University of Florence, via della Lastruccia 3 - Sesto Fiorentino, 50019 Florence, Italy

Received August 5, 2010. Revised Manuscript Received October 24, 2010

This Article reports an investigation on the use of magnesium hydroxide nanoparticles dispersed in alcohols to inhibit two different and synergistic degradation processes usually affecting historically valuable manuscripts and, more generally, paper documents. We show that the preservation of paper from acid hydrolysis and oxidative ink corrosion can be achieved by stabilizing the final pH of deacidified paper around 6.5 to 7.5. Reactive magnesium hydroxide nanoparticles with a narrow size distribution, obtained by using a novel synthetic procedure, are very efficient in controlling paper's pH to avoid further degradation of cellulose from acid hydrolysis, oxidative ink corrosion, or both. The deacidification and antioxidant actions of magnesium hydroxide nanoparticles are compared with magnesium oxide particles present in one of the best mass deacidification methods (Bookkeeper).

Introduction

In a recent highlight,[1] Wouters outlined that paper objects are deteriorating rapidly and their long-term conservation requires a full understanding of the chemical degradation mechanisms to conceive appropriate methodologies for conservation. Basically, conservation is entering in the science arena moving from a consolidated "trial and error practice" to the use of a deep scientific background. In this respect, nanoscience is of tremendous help, as outlined in recent publication by us.[2−10]

The main cellulose degradation pathways are the acid hydrolysis of glycosidic bonds and oxidation. Low pH values can lead to cellulose depolymerization, even at room temperature.[11] Protons hydrolyze the $\beta(1,4)$-glycosidic bond of the cellulose, leading to a decrease in the chain length to the molecular level and to a loss of mechanical resistance on the macroscopic scale.[12] It is well known that during the making of iron-gall inks, gallic acid, formed by hydrolysis of tannins extracted from gall-nuts, reacts with iron(II) sulfate (i.e., vitriol, as reported in old recipes) to give a pyrogallate complex of iron(III) and sulfuric acid.[13,14] Iron-gall ink was commonly used in ancient manuscripts that are contaminated by acids, especially in the capital letters, where a high amount of ink was used. A variant of iron-gall ink, widely used in Europe for a long time,[15−17] contains copper salts (called metal-gall inks) and produces similar degradation mechanisms shown by iron inks.

However, sulfuric-acid-catalyzed hydrolysis of cellulose is not the only paper degradation pathway due to the presence of iron-gall ink. Transition-metal ions usually catalyze cellulose oxidation through a free radical mechanism known as the Fenton reaction, which involves iron ions (in the presence of copper, the reaction is called Fenton-like reaction) and hydrogen peroxide formed in situ[17] according to the following relationships.

(1) Formation of peroxides in acidic medium:

$$Fe^{2+} + O_2 + H^+ \rightarrow Fe^{3+} + HOO^{\bullet}$$

$$Fe^{2+} + HOO^{\bullet} + H^+ \rightarrow Fe^{3+} + H_2O_2$$

(2) Homolytic decomposition of peroxides by transition metal ions:

$$Fe^{2+} + H_2O_2 \rightarrow Fe^{3+} + OH^- + OH^{\bullet} \quad \text{Fenton reaction}$$

$$Cu^{+} + H_2O_2 \rightarrow Cu^{2+} + OH^- + OH^{\bullet} \quad \text{Fenton-like reaction}$$

These processes can produce severe degradation of paper as the perforation of the inked areas or a general loss of the typical mechanical properties of paper, that is, elasticity and tensile strength. As a consequent effect of paper degradation, it is not rare to see

*Corresponding author. Tel: +39 0554573032. Fax: +39 0554573032. E-mail: baglioni@fi.unifi.it.

(1) Wouters, J. *Science* **2008**, *322*, 1198–1198.
(2) Chelazzi, D.; Baglioni, P.; Giorgi, R. *Macromol. Symp.* **2006**, *238*, 80–86.
(3) Giorgi, R.; Bozzi, C.; Dei, L.; Gabbiani, C.; Newman, R. W.; Baglioni, P. *Langmuir* **2005**, *21*, 8495–8501.
(4) Giorgi, R.; Chelazzi, D.; Baglioni, P. *Appl. Phys. A: Mater. Sci. Process.* **2006**, *83*, 669–673.
(5) Giorgi, R.; Chelazzi, D.; Baglioni, P. *Langmuir* **2005**, *21*, 10743–10748.
(6) Giorgi, R.; Dei, L.; Ceccato, M.; Schettino, C.; Baglioni, P. *Langmuir* **2002**, *18*, 8198–8203.
(7) Carretti, E.; Bonini, M.; Dei, L.; Berrie, B. H.; Angelova, L. V.; Baglioni, P.; Weiss, R. G. *Acc. Chem. Res.* **2010**, *43*, 751–760.
(8) Carretti, E.; Fratini, E.; Berti, D.; Dei, L.; Baglioni, P. *Angew. Chem., Int. Ed.* **2008**, *47*, 8902–8905.
(9) Giorgi, R.; Baglioni, M.; Berti, D.; Baglioni, P. *Acc. Chem. Res.* **2010**, *43*, 695–704.
(10) Baglioni, P.; Giorgi, R. *Soft Matter* **2006**, *2*, 293–303.
(11) Feugel, H.; Wegener, D. *Wood: Chemistry, Ultrastructure, Reactions*; Walter de Gruyter: Berlin, 1984.
(12) Ott, R. S.; Wong, L. C.; Hornstein, O. C.; Mares, T.; Graef, J. N. *Text. Res. J.* **1954**, *24*, 369–436.
(13) Nassau, J. O.; Miesch, C. T. *1st ICOM-CC Conf. 12th Triennial Meeting*; Bridgland, J., Ed.; James and James: London, 1999; pp 528–533.
(14) Krekel, C. *Chemische Struktur historischer Eisengallustinten*. In *Tintenfraß in Archiv und Bibliothek*; Banik, G., Weber, H., Eds.; Workshop der Staatlichen Archivverwaltung Baden-Württemberg, Amt 6, Landesarchivdirektion, Kohlhammer: Stuttgart, Germany, 1995; Vol. 16, pp 25–36.
(15) Kolar, J.; Strlič, M.; Bučar, M.; Matsui, T.; Šelih, V. S.; Simčič, T. *Acta Chim. Slov.* **2003**, *50*, 763–779.
(16) Del Carmine, P.; Giannini, L.; Hoogen, W.; Lazzeri, F.; Mandò, P. A. *Nucl. Instrum. Methods Phys. Res., Sect. B* **1996**, *113*, 354–359.
(17) Lazzeri, F.; Mandò, P. A. *Nucl. Instrum. Methods Phys. Res., Sect. B* **1998**, *136–138*, 644–652.
(18) Neevel, J. G. *The Development of a 'Bio Conservation Treatment for Ink Corrosion' Based on the Natural Anti-Oxidant Phytate*. http://cool.conservation-us.org/jaic/jaic45/jaic45-1-003.pdf (accessed Feb 23, 2010).

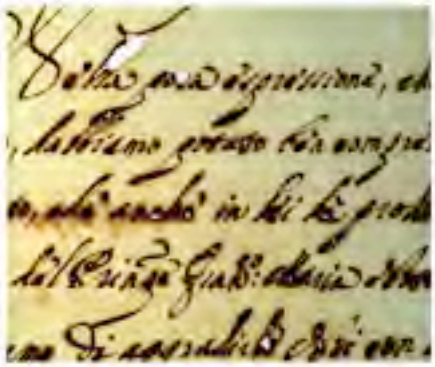

Figure 1. Typical example of metal-gall ink corrosion on an 18th century document.

portions of documents from the 16th, 17th, and 18th centuries completely corroded by inks (See Figure 1.)

Several methods have been proposed to achieve an efficient and long-lasting conservation treatment. Phytate aqueous solutions were demonstrated to stop Fenton reaction efficiently by coordination of the iron ions.[17–20] More recently, the usage of tetrabutylammonium bromide (TBAB) or other alkylammonium bromides[17,20–23] as antioxidants for metal-gall inks and nonaqueous deacidification treatments have been proposed. Among the nonaqueous methods, the Bookkeeper+ (Preservation Technologies, L.P.) is a dispersion of mainly microsized particles of MgO in fluorinated solvents.[24] Although it presents several advantages over the conventional deacidification methods, Bookkeeper also shows some drawbacks; for example, its application is discouraged when paper porosity is low because of the fact that the particles present in the Bookkeeper are not small enough to penetrate uniformly inside the paper and may produce a light whitening of the document surface. Moreover, to stabilize the magnesium oxide dispersion, high concentrations of fluorinated surfactants are used. The long-term effects of these surfactants that remain on paper after the treatment are not yet known.[25] Despite these drawbacks, Bookkeeper is widely used, and it is one of the best nonaqueous mass deacidification treatments available.

(18) Kolar, J.; Strlič, M.; Štolfa, M. *Polym. Degrad. Stab.* **2005**, *91*, 3179–3187.
(19) Neevel, J. G. *Restaurator* **1995**, *16*, 143–160.
(20) Kolar, J.; Mozir, A.; Kolar, M.; de Bruin, G.; Pihlar, B.; Strlič, M. *J. Cult. Herit.* **2007**, *8*, 19–24.
(21) Neevel, J. G. *In The Iron Gall Ink Meeting*; Brown, J. E., Ed.; The University of Northumbria: Newcastle upon Tyne, U.K., 2000; pp 127–134.
(22) Zappalà, A.; De Stefani, C. *Restaurator* **2005**, *26*, 36–45.
(23) Hennigan, L.; Ralston, R.; Banik, G.; Halvorson, E.; Allman, L.; Proksanis, T.; Perilloux, A. *Cellulose* **2008**, *15*, 865–876.
(24) Poulikos, A.; Hennigan, L.; Banik, G. *Cellulose* **2008**, *15*, 849–859.
(25) *European Research Project Into Con-Deacidification of Iron Gall Ink Containing Paper*. CEC http://cordis.europa.eu/search/index.cfm?fuseaction=proj.document&PJ_LANG=EN&PJ_RCN=3471645&pid=9&q=CA13A4932D0842D2CE4802A4307C7A2D&type=sim (accessed Nov 16, 2010).
(27) Kolar, J.; Mozir, A.; Štolfa, A.; Štrlič, M.; Cerra, D.; Conte, V.; Morvan, V.; Steemers, T. *In Recent Advances in Book and Paper Conservation: Annual Congress of the European Confederation of Conservator-Restorers' Organisations*; Proceedings of the ECCO Congress, Istanbul, Turkey, 2–5 May 2007; Archetype Publications: London, 2008; pp 134–139.
(28) Mahieux, E.; Kolar, J.; Strlič, M.; Pedron, S. *e-Preserv. Sci.* **2009**, *7*, 13–18.
(29) Preservation Technologies Website – Bookkeeper FAQ Section. http://www.ptlp.com/faq.html (accessed Feb 25, 2010).
(30) Zervos, S.; Walworth, A. *Stud. Conserv.* **2001**, *46*, 69–89.
(31) George, R.; Daly, T.; Shahani, C.; Maclaren, R. *In Postprints of the Baltimore Congress 1985: Works of Art on Paper: Books, Documents and Photographs: Techniques and Conservation*; Mitchell, Mrs. Garnett, V., Ed.; The Institute for Conservation: London, 2002; pp 69–73.
(32) Sequeira, S.; Casanova, C.; Cabrita, E. J. *J. Cultural Heritage* **2006**, *7*, 264–272.

Table 1. Composition of the Reaction Mixture for the Preparation of Metal-Gall Ink

gall nuts	85 g
ethyl alcohol	10 mL
distilled water	192 mL
acetic acid	17.4 mL
metal salt	4.8 g
arabic gum	4.8 g

Recent studies[8,9,11–14] have shown that alcoholic dispersions of calcium and magnesium hydroxide nanoparticles can be used for the neutralization of paper acidity and can generate an alkaline reserve of carbonate (after the reaction of the hydroxide with CO_2 from air) that prevents further degradation. This method was very well received.[12–14] However, the efficacy of nanoparticles on the corrosive metal-gall inks has not yet been studied.

In this manuscript, the application of nanoparticles for the deacidification of paper and the inhibition of Fenton reactions are investigated, and their efficacy has been compared with the Bookkeeper+ method. Bookkeeper, a dispersion of magnesium oxide in fluorinated solvents, was chosen because it is a very good deacidification method and it is similar to nanoparticles in terms of chemical composition (microparticles of MgO vs nanoparticles of $Mg(OH)_2$). We show that a deacidification treatment based on magnesium hydroxide nanoparticles in alcohol dispersion is able to preserve paper, with a single treatment, from both acid hydrolysis and oxidative ink corrosion by simply controlling the final pH of paper to 6.5 to 7.5, opening new perspectives in the conservation of cellulose-based documents and artifacts.

Materials and Methods

Synthesis and Preparation of $Mg(OH)_2$ Nanoparticles Dispersion. Magnesium hydroxide nanoparticles were synthesized through a coprecipitation reaction at 90 °C in an IKA reactor apparatus. Two different preparations were made. In the first, 1 M $MgCl_2$ aqueous solution was mixed with a 4 M NaOH solution, resulting in a molar ratio of 1:1.6 between Mg^{2+} and OH^- ions; in the second, a molar ratio of 1:2 was obtained with 1 M $MgCl_2$ aqueous solution and a 3.5 M NaOH solution. Precipitated $Mg(OH)_2$ was maintained under stirring for 3 h to peptize the particles. Nanoparticles were purified by dialysis using distilled water. Two different dispersions were prepared from each preparation: the first one starting from the wet precipitate (containing about 50% of water) and the second from nanoparticles dried at 50 °C under vacuum. Dispersions in 2-propanol were obtained by using an ultrahomogenizer system (Ultraturrax T50) and sonicating with a Bronson sonicator S-450D.

Ink Preparation. Inks used in this work were prepared according to an adapted recipe by Petrus Castoreus reported in the *De Arcendenda Corporum Gravitate* treatise (A.D. 1610).[31] Table 1 reports the composition of the reaction mixture used for the preparation of the ink.

The ink was prepared as follows: gall nuts (provided by Zecchi – Art Shop, Florence) were broken and then grinded in a mortar to optimize the extraction of tannic acid. The obtained powder was placed in a beaker with ethyl alcohol, acetic acid, and water, and the mixture was heated to the boiling point. The initial volume of the suspension was reduced to ~35%, cooled, left to rest for 4 days, and filtered to separate the powder from the yellowish

(33) Wallace, E.; Parmentola, C. *Restaurator* **2007**, *28*, 197–203.
(34) Wallace, E.; Parmentola, C. *Restaurator* **2008**, *29*, 225–238.
(35) Bell, P. *Nanotechnologies for Conservation of Cultural Heritage: Paper and Canvas Deacidification*. Rensselaer Polytechnic Institute: Troy, NY, **2007**. doi: 10.1016/j.culher.2010.07.011. (Accessed November 19, 2010.)
(36) Horie, C. V. *Q. Fr. Zeit.* **2003**, *44*, 31–35.

DOI: 10.1021/la103994j | 9082

Table 2. Composition of the Investigated Inks

ink name	metal/gall resin (weight ratio)	Cu^{2+}/Fe^{3+} (molar ratio)	$FeSO_4 \cdot 7H_2O$ (weight)	$CuSO_4 \cdot 5H_2O$ (weight)
Ink_Fe_1:1	1		0.8 g	
Ink_Fe_1:2	0.5		2.4 g	
Ink_1:1_Cu-1	1	1	2.5 g	2.5 g
Ink_1:1_Cu-0.25	1	0.25	7.5 g	0.8 g

solution. The mixture was then heated to the boiling point, and the metal salt was slowly added. The solution suddenly turned black because of the formation of the pyrogallate−metal complex. Arabic gum (from Zecchi) was then added to the solution under vigorous stirring. The ink was heated until a film appeared on the surface. Four inks were prepared according to this procedure to simulate the high variability of the composition of inks that can be found on valuable historical manuscripts. Two pure iron-gall inks were prepared by using a different gall nuts and iron salt ratio. Two additional formulations were obtained by adding a mixture of iron and copper sulfates to obtain metal-gall inks with a different Cu^{2+}/Fe^{3+} molar ratio. Salts used for the preparation of the four inks were copper(II) sulfate pentahydrate supplied by Carlo Erba (Italy) and iron(II) sulfate heptahydrate (Pb, Ba, Cl: chlorides < 300 ppm; Zn < 500 ppm; heavy metals < 50 ppm; K_2O < 0.3%; M_2O_3 < 0.1%) supplied by Fluka Chemicals. Other reagents were ethyl alcohol (96%) and acetic acid (99.5%) supplied by Fluka Chemicals.

In Table 2, compositions of the four model inks are reported.

In summary: (1) Ink_Fe_1:1 represents a classic pure iron-gall ink that contains only iron ions. The ratio between metal salts and gall nuts (w/w) implies that iron ions are in excess with respect to gallic acid molecules;[30] therefore, free iron ions are present and catalyze cellulose oxidation according to the mechanism above described. (2) Ink_Fe_1:2 represents a lesser-corrosive pure iron-gall ink because of the lower amount of iron salt used. (3) Ink_1:1_Cu-1 is a metal-gall ink prepared with a molar ratio of 1:1 between copper and iron sulfates. (4) Ink_1:1_Cu-0.25 contains a small amount of copper (∼20% of the total weight of metal salts added). The molar ratio between copper and iron ions is 0.25.

Paper and Ink Application. Whatman paper no. 1 (Schleicher & Schuell, 99% made with cotton fibers, 88.0 g m^{-2}, degree of polymerization (DP) 1230[31]) was selected for the experiments because it can be considered to be a reference paper for a manifold extensive analysis on the degradation of cellulose after deacidification treatments and artificial aging. Inks were applied on the paper by means of a brush. After 1 week at constant room humidity (RH 45%, 25 °C), the samples were weighed to evaluate the amount of ink present on paper. The average value was 55 ± 2 mg (2.3 mg cm^{-2}) under the normal laboratory conditions with a water content in the paper of ∼5%.[32] Figure 2 shows a typical inked sample: the ink is on one side of the reference paper, whereas the verso presents only some spotted areas due to ink penetration.

Applied Inks Treatments. Inked papers were treated with the following conservation treatments.

Water (AQ). Samples were immersed in distilled water (25 °C) for 20 min. After soaking, the samples were left to dry in the air at controlled RH for 3 days. After this time, samples were weighed.

Bookkeeper (BK). Samples were treated with a commercial dispersion of MgO of micro- and submicrometed particles in fluorinated solvent (perfluorinated-hydrocarbon and fluorinated surfactants[33]). Dispersion (3 mL) was applied by means of a brush on each sample on both sides. The treated samples were then left to dry in the air at controlled RH for 10 days, time necessary to neutralize acidity and to change magnesium oxide into carbonate, that is, the alkaline reserve. After this time, samples were weighed.

Dispersion of $Mg(OH)_2$ Nanoparticles in 2-Propanol (Mg). Samples were treated with 0.11 M (6.4 ± 0.5 g/L) nanoparticles,

Figure 2. Inked Whatman paper sample: recto (left) side and verso (right) side.

dispersed in alcohol, at approximately the same concentration as Bookkeeper formulation. Dispersion (3 mL) was applied by means of a brush on both sides of each sample. The treated samples were then left to dry in the air for 10 days at controlled RH, time necessary for the acidity neutralization and the chemical reaction of the hydroxide into carbonate. After this time, samples were weighed.

Characterization of Nanoparticles Dispersions. A Brookhaven Plus90 size analyzer, equipped with a Peltier temperature control system, was used to perform dynamic light scattering (DLS) analysis. A vertically polarized He−Ne laser (λ = 633 nm, 5 mW) was used as the light source. The laser long-term power stability was ±0.2%.

Inked-Paper Sample Characterization. Paper degradation may be described as a shortening of cellulose chains that is a depolymerization process. DP can be obtained from viscosity determinations.[34] To normalize the DP results obtained from different techniques, the scission number, that is, the number of scissioned glycosidic bonds (*S*), is commonly preferably used and defined as

$$S = \left(\frac{1}{DP_{n,t}} - \frac{1}{DP_{n,0}} \right) \cdot 100$$

where $DP_{n,t}$ is the average chain length at time, *t*, and $DP_{n,0}$ is the average chain length at time zero. The average chain length is empirically calculated, halving the corresponding DP, obtained from viscosity determinations.[35]

In this Article, a kinematic Ubbelohde viscometer has been used for the determination of specific viscosity of a cellulose cupriethylenediamine water (1:1) solution. Cupriethylenediamine (CED) was supplied by Carlo Erba (Italy).

Each paper sample contained a meaningful amount of ink that might influence its specific viscosity. Because the same amount of ink (55 mg ± 2 mg) is present on each sample, we can rule out the ink influence on the viscosity (ink, however, can be affected by a systematic error). It is worth noting that DP determination by viscometry is an international standard procedure for the characterization of cellulose during the industrial papermaking process. As previously indicated, metal-gall ink leads to paper oxidation; therefore, CED solution, with its high basicity (pH > 12), also induces a depolymerization through β-alkoxy elimination mechanism.[36,37] This is the reason why all measured DP values underestimate the real ones. Because the experimental data refer to homogeneous series of samples, the comparison of these results can be considered to be fully acceptable.

pH measurements were performed with a digital pH-meter Crison Basic 20, through 1 h cold water (4 mL) extraction of 60 mg

(36) Choi, 2002. (as quoted in ref 35).
(37) Williams, P. W. *Biopolymers* **1974**, *13*, 43.
(38) Strlič, M.; Kolar, J.; Žigon, M.; Pihlar, B. *J. Chromatogr. A* **1999**, *847*, 169.
(39) Strlič, M.; Poggi, G.; Fiorin, A.; Lo Nostro, P. *Biomacromolecules* **2003**, *4*, 1632.

of paper, according to a commonly used procedure in conservation laboratories.

Inked-Paper Sample Aging. An accelerated aging cycle was used to maximize paper corrosion. Samples were put in a sealed box to prevent the evaporation of the volatile degradation products and kept at 90 °C. The humidity inside the box was maintained at 75% with a potassium chloride saturated aqueous solution. Sample aging was monitored after 6, 12, 24, and 48 h.

Results and Discussion

The presence of metal-gall ink on paper implies locally (i.e., on inked strokes) very low pH values due to the presence of sulfuric acid. Moreover, in an acidic medium, copper and iron ions, as previously indicated, induce cellulose oxidation through Fenton and Fenton-like reactions. For these reasons, a deacidification intervention and an antioxidant treatment are both needed to preserve paper from degradation.

Strlič[47] investigated two common redox couples of transition-metal ions (Fe(II)/Fe(III) and Cu(I)/Cu(II)) present in ancient inks and showed that the catalytic activity of iron is maximum in the pH range 8 to 8.5, whereas for copper ions, the catalytic activity sharply increases for pH >8.5. Recent particle-induced X-ray emission (PIXE) investigations performed on several historical documents showed that copper is often associated with iron-gall ink,[48−51] this implies that deacidification treatments on paper could be detrimental when the final pH is higher than 8.5, and explains why some deacidified inked papers are more prone to oxidation.[5] For this reason, several groups have searched and studied antioxidant materials to be combined with the commonly used deacidification treatments.[11,27,28,39,52,53]

It has also been shown[47] that catalytic activity of metal ions (copper or iron) is minimal when pH is around neutrality. This means that the precise control of paper acidity/alkalinity could provide an easy way to reduce the degradation rate of oxidation through Fenton and Fenton-like reactions. In other words, it should be possible to inhibit the ink-catalyzed degradation of cellulose with only a deacidification/conservation treatment.

In previous studies, we proposed the use of calcium and magnesium hydroxide nanoparticles for the deacidification of acidic papers.[5,6,11] Nanoparticles were shown to be efficient in the deacidification and were able to form an alkaline reserve that prevents documents from further degradation.[27−34]

Particle size distribution of three magnesium hydroxide dispersions was obtained by DLS. Dispersion of the wet precipitate of the 1:2 salts ratio preparation (Materials and Methods section) showed a unimodal distribution of particles size (Figure 3).

The average size distribution was centered at 350−400 nm. Although this size distribution is acceptable for a deacidification treatment, smaller particles are preferable to avoid whitening of the inked paper and for a better homogeneity of particles distribution within the cellulose fibers. Dispersion of dried particles of 1:2 ratio preparation redispersed in isopropyl alcohol showed a bimodal size distribution with the first distribution centered at ~140 nm and a second one centered at about 350−400 nm. This result suggests that the different size distributions measured by DLS for wet and dried particles depend on the hydrogen bonding capacity of the solvent[54] and, in the present case, are due to the presence of the residual water from the synthesis that interacts with magnesium hydroxide nanoparticles favoring the clustering

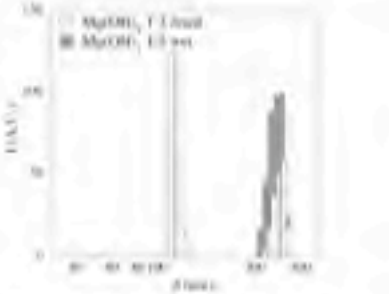

Figure 3. Histograms representing the size distribution of $Mg(OH)_2$ 1:2 dried and $Mg(OH)_2$ 1:2 wet nanoparticles dispersions obtained by DLS analysis.

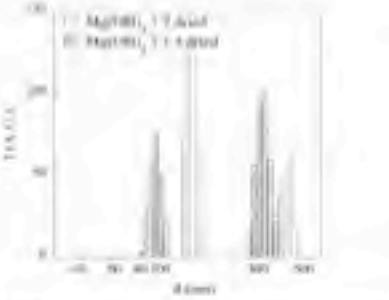

Figure 4. Histograms representing the size distribution of $Mg(OH)_2$ 1:2 dried and $Mg(OH)_2$ 1:1.4 dried nanoparticles dispersions obtained by DLS analysis.

of the nanoparticles. By simply drying the nanoparticles, part of the clusters is dissolved, and the real dimensions of the synthesized nanoparticles are revealed after redispersion in 2-propanol.

The synthesis of magnesium hydroxide using a slightly larger amount of magnesium with respect to the coprecipitating ions (1:1.4 ratio) produced even smaller particles, as shown in Figure 4. DLS analysis of the dispersion obtained starting from the dried nanoparticles showed a bimodal size distribution with one particles population centered at 90 nm and the second one centered at 300 nm. The presence of free magnesium ions seems to inhibit nanoparticles clustering, suggesting the possible charging of particles surfaces with the Mg^{2+} excess, which partially inhibits aggregation.

Considering that the usage of smaller particles for paper treatment, besides aesthetical reasons, is preferable because of their higher chemical reactivity, in this study, we used the dispersion with a size distribution centered around 90 nm for the deacidification of inked samples. Particle size plays a really important role in the acidity neutralization and in the carbonation process that provides to the paper the alkaline reserve, which is essential to achieve a long-lasting deacidification.

None of the conservation treatments examined in our study produced appreciable color change on the surface of the paper samples. Nonaqueous treatments prevent ink from possible risks of solubilization. However, aqueous treatments are still used in some cases: physicians and limewater, for example, are commonly applied on paper when less-water-sensitive inks were used. To

(47) Strlič, M.; Kolar, J.; Šelih, V. S.; Kočar, D.; Pihlar, B. *Acta Chim. Slov.* **2003**, *50*, 619−632.
(48) Reissland, B. *Restaurator* **1999**, *20*, 147−160.
(49) Fuster-López, L.; Piqué, M.; Giorgi, R.; Cotte, M.; Baglioni, P.; Dreon, R.; Zanini, P. *Langmuir* **2007**, *23*, 2350−2354.

 DOI: 10.1021/la103044t

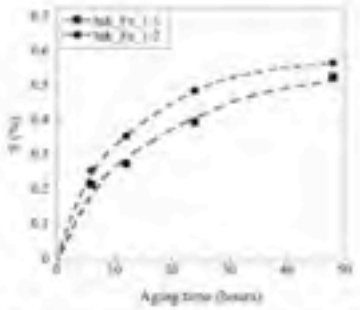

Figure 5. Cellulose degradation curves of paper sample treated with Ink_Fe_1:1 and with Ink_Fe_1:2; comparison between the scission number of the cellulose bonds (*S*%) for the untreated samples.

Table 3. Degrees of Polymerization (DP) of Paper Samples Covered with Ink_Fe_1:1 and with Ink_Fe_1:2 and Washed with Water (AQ)

aging time (h)	Ink_Fe_1:1 untreated	Ink_Fe_1:1 AQ	Ink_Fe_1:2 untreated	Ink_Fe_1:2 AQ
	DP	DP	DP	DP
0	1062	712	988	821
6	467	535	452	565
12	431	393	390	528
24	339	336	289	421
48	279	247	259	297

highlight the effects of aqueous deacidification over the inked paper, we immersed some samples in water for 20 min. The aqueous treatment (AQ) led to a considerable loss (~50%) of the applied ink, as determined by gravimetric measurements. The ink loss is a hurdle in the field of manuscript conservation; therefore, the usage of aqueous methods must be limited and discouraged. On the other side, the deacidification with the nonaqueous dispersions did not cause ink bleeding, as expected. Upon the aging, the treated samples mostly preserved their original mechanical properties, with the exception of the samples treated with water (AQ) that showed some degradation effects. The untreated samples lost their typical mechanical strength just after 24 h of aging, becoming very fragile and tending to crumble if manipulated.

Depolymerization of cellulose, due to acid hydrolysis or to the combined action of oxidation and hydrolysis, was monitored, determining the DP through viscosity measurements to quantify the samples degradation upon the aging. Kinetic constant could not be obtained from this data set because the DP did not reach a plateau (LODP).[37] For each series of samples, a table indicates the average degree of polymerization values (±50 DP). The corresponding scission numbers (*S*%) are reported in the Figures, as eye-line guide helps the comparison between the different conservation treatments upon the aging.

Figure 5 shows a comparison between samples covered with Ink_Fe_1:1 and Ink_Fe_1:2 that contains a different amount of free iron ions.[30]

It is important to note that DP values (Table 3) just after the application of ink ($t = 0$) having different iron content showed a difference that is slightly larger than the error limit (±50 units), in favor of the iron-richer ink. Upon the aging, samples with a lower amount of iron excess degrade faster, this result might not be

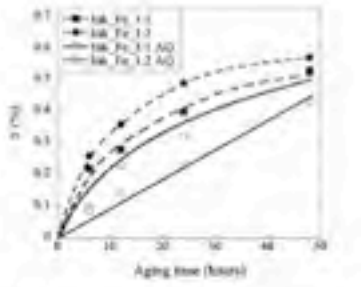

Figure 6. Cellulose degradation curves of paper sample treated with Ink_Fe_1:1 and with Ink_Fe_1:2; comparison between untreated samples and samples washed with water (AQ).

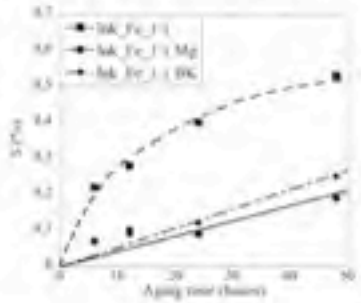

Figure 7. Cellulose degradation curves of paper sample treated with Ink_Fe_1:1; comparison between untreated inked paper and the samples deacidified with nanoparticles (Mg) and with Book-keeper (BK).

indicative of real different degradation processes because the differences in DP are close to the experimental error (±50 DP). To test the efficacy of the two deacidification methodologies for the concomitant inhibition of acid-catalyzed and oxidative cellulose degradation, we chose to apply the treatments on ink, with larger free-ions content, that is, Ink_Fe_1:1.

As expected, all inked-paper samples immersed in water (AQ) presented a considerable ink loss (~50% by weight) with a consequent decrease in the cellulose degradation upon aging, mainly due to the decrease in the iron amount present on the paper. (See Figure 6.) In the case of Ink_Fe_1:1, free iron ions were largely removed with washing, producing some benefit for cellulose within 24 h of aging. This is even more evident for Ink_Fe_1:2 samples, where an even smaller amount of free ions was originally present. This latter case suggests that degradation rate of cellulose, due to the presence of acids coming from inks and to the catalytic activity of free ions, is not strictly depending on the concentration. In fact, Figure 5 shows that the two inks degrade paper in almost the same way. After water treatment, the iron-richer ink still contains some amount of free ions, and this explains the degradation of Ink_Fe_1:1 sample upon aging.

The nanoparticles efficacy against paper aging and the comparison with the commercial Bookkeeper method are reported in the following. Figure 7 (see also the corresponding Table 4) shows the cellulose degradation curves upon the aging of inked paper samples after the application of two conservation methodologies

(35) Calvini, P. *Cellulose* **2008**, *15*, 445–456.

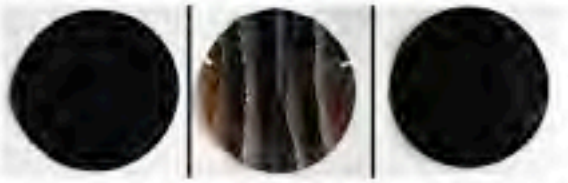

Figure 8. Comparison between inked paper samples before and after the aging. On the left, a unaged sample; on the middle, the untreated aged sample, where the loss of the paper mechanical properties is evident; on the right, the sample deacidified with nanoparticles that retain the mechanical properties of the unaged sample.

Table 4. Degrees of Polymerization (DP) of Paper Samples Covered with Ink_Fe_1:1 and Deacidified with Bookkeeper (BK) and $Mg(OH)_2$ Nanoparticles (Mg)

aging time (h)	Ink_Fe_1:1 Bookkeeper (BK)	Ink_Fe_1 Nanoparticles (Mg)
	DP	DP
0	1037	995
6	743	725
12	712	710
24	651	686
48	445	501

(Bookkeeper and $Mg(OH)_2$ nanoparticles in 2-propanol dispersion).

The appearance of the samples after aging was good, and any appreciable difference was detected with respect to unaged samples. The dispersing media used for the Bookkeeper and nanoparticles dispersions did not induce any ink ions, contrary to the immersion in water. Curves of $S(\%)$ versus aging time (Figure 7) showed for Bookkeeper and nanoparticles a very good protection against paper aging. It must be reminded that to disperse the microsized particles of magnesium oxide, a surfactant is needed; on the other side, nanoparticles dispersion does not require any other product to be stabilized and, therefore, it can be considered to be a deacidification methodology that is "safer" than Bookkeeper. However, Bookkeeper has the advantage that the microparticles are in fluorinated solvents that confer a larger flexibility for mass deacidification.

As reported in the Introduction, iron-gall inks often contain copper as contaminant that is known to amplify the degradation pattern during the aging of the paper. In the following section, we report the evaluation of $Mg(OH)_2$ nanoparticles application to samples with iron-gall inks containing copper, that is, metal-gall inks.

At pH > 8.5, copper ions are catalytically more active than iron in cellulose degradation, favoring radical formation and leading to Fenton-like reaction.[31] Paper samples treated with metal-gall inks were dark, very similar to the ones treated with pure iron gall inks; Ink_1:1_Cu-1, containing 50% copper content (mol/mol), presented some very light tone changes toward brown.

Any meaningful color changes were appreciated after 48 h of aging for the samples deacidified with the nanoparticles. The untreated samples showed a severe and diffuse browning, just after 24 h. (See Figure 8.) Some differences were observed in the mechanical properties of the untreated samples: paper containing a copper-richer ink (Ink_1:1_Cu-1) was very fragile, even after 6 h of aging with the complete loss of the mechanical properties just after 12 h. Samples inked with copper-poorer ink (Ink_1:1_Cu-0.25) seemed to be a little more resistant, even though they crumbled after 48 h. On the contrary, all of the samples treated with magnesium hydroxide nanoparticles showed a mechanical strength very similar to that of the unaged samples.

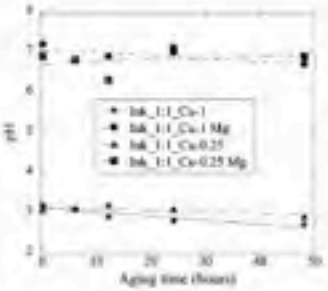

Figure 9. pH values during aging of the samples inoculated with different Cu/Fe metal-gall inks (Cu-1 and Cu-0.25) and protected with $Mg(OH)_2$ nanoparticles application (Cu-1 Mg and Cu-0.25 Mg).

Table 5. Degrees of Polymerization (DP) of Samples Covered with Ink_1:1_Cu-1 and with Ink_1:1_Cu-0.25 and Deacidified with $Mg(OH)_2$ Nanoparticles (Mg)

aging time (h)	Ink_1:1_Cu-1 untreated	Ink_1:1_ Cu-1 Mg	Ink_1:1_Cu-0.25 untreated	Ink_1:1_ Cu-0.25 Mg
	DP	DP	DP	DP
0	917	829	843	846
6	508	590	699	733
12	220	386	480	471
24	149	329	299	377
48	105	294	205	291

To investigate the role of acidity in the ink-catalyzed corrosion of cellulose, we monitored the pH during the aging. The initial ink pH was strongly acidic (pH 3), and this value was found for all examined inks. The deacidification treatment with nanoparticles was performed to reach pH 7, which is a suitable value because the catalytic activity of copper and iron ions is at the minimum value.[32]

Figure 9 shows that pH of the deacidified samples is stable during the aging, whereas a little decrease (0.5 pH unit) was observed for the untreated samples. A similar trend was observed for the paper samples treated with pure iron gall-inks. As can be seen from Tables 3 and 5, the addition of copper to the iron-gall ink induced a more pronounced degradation on paper samples. It is worth noting that the initial DP values of Ink_1:1_Cu-1 and Ink_1:1_Cu-0.25 systems are lower than those of the corresponding samples treated with pure iron-gall inks.

These measurements were performed 30 days after ink application, enough to highlight the degradative effect of the different inks. Moreover, samples ink_1:1_Cu-1 showed a degradation rate

 DOI: 10.1021/la103044t

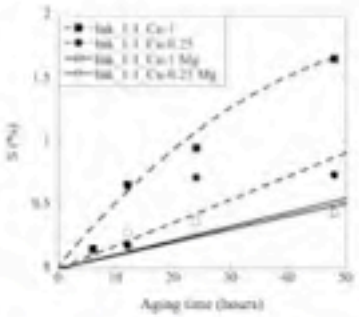

Figure 10. Cellulose degradation curves of paper sample treated with Ink_1:1_Cu-1 and with Ink_1:1_Cu-0.25: comparison between untreated and deacidified with nanoparticles (Mg) samples.

almost doubled with respect to ink_1:1_Cu-0.25 samples containing a lower amount of copper ions. In both cases, as already seen for the pure iron-gall inks, nanoparticles deacidification produced (Figure 10) a strong inhibition of the cellulose depolymerization processes.

Conclusions

In the present work, the deacidification of paper at pH 7 was demonstrated to be sufficient to achieve a complete conservation treatment to inhibit simultaneously metal-catalyzed oxidation and acid-catalyzed hydrolysis of cellulose. To this purpose, magnesium hydroxide particles with average size and size distribution optimal for paper conservation have been synthesized, and their properties have been investigated and compared with commercial magnesium oxide dispersions (Bookkeeper). Both of these are nonaqueous deacidification methods. The nonaqueous Bookkeeper or nanoparticles pH-controlled deacidification processes are very efficient in "protecting" cellulose from depolymerization, even in the presence of transition-metal ions that catalyze oxidative processes. The main advantage with respect to commonly used antioxidant treatments as phytates or TBAB (both requiring a farther deacidification process) is that it is possible to inhibit in a single step two degradation pathways (oxidation and hydrolysis), acting on paper degradation in a synergistic way. Moreover, the usage of alcohol, or fluorinated solvents, to disperse inorganic particles minimizes the risk of swelling and solubilization of metal-gall inks, which may be lost by using aqueous treatment.[23−25,43] Nanoparticles of magnesium hydroxide are slightly better than the popular Bookkeeper and do not present the possible drawbacks due to the large amount of fluorinated surfactants used to stabilize the dispersion of magnesium oxide in the Bookkeeper. These fluorinated surfactants remain on the paper after the deacidification procedure with possible side effects during the natural aging of paper that are unknown at the present.

Acknowledgment. We wish to thank Marta Settembri and Veronica Baldoneschi for their precious assistance and Adele Giannetti for her precious cooperation. CSGI is acknowledged for financial support.

Ringraziamenti

Questi tre anni di dottorato mi hanno permesso di conoscere il significato di ricerca, mi hanno insegnato cose che sono state fatte o scritte e cose che non si possono scrivere. Ho imparato infatti quanto sia determinante avere un maestro su cui contare nei momenti di difficoltà e con cui gioire dei piccoli successi. Ringrazio il Prof. Piero Baglioni, persona insostituibile nel mio corso di studi per essermi stata vicina e per avermi iniziato al mondo del lavoro e della ricerca scientifica.

Ringrazio Rodorico Giorgi per avermi sempre coinvolto in nuove ed avvincenti sfide e per aver riposto in me sempre molta fiducia.

Ringrazio Silvia Nappini, amica di sempre, per aver condiviso le pene a cui alle volte si rimane esposti.

Ringrazio Tamer Al Kayal per aver reso sicuramente più lieto questo periodo alleggerendo con la simpatia l'atmosfera lavorativa.

Ringrazio Emanuela Grassi, Manola Trastulli e Filippo Baldereschi per il supporto tecnico e l'amicizia di cui mi han fatto dono.

Ringrazio Chiara Vannucci per avermi affiancato con i fitting e per non essersi mai tirata indietro quando avevo bisogno di aiuto.

Ringrazio Giovanna Poggi per il supporto tecnico cartaceo e linguistico.

Ringrazio Valentina Martelli per aver ampliato le mie conoscenze ed avermi dato la possibilità di muovermi in nuovi ambiti.

Ringrazio Martina Bachelli per essersi fidata di me anche quando la situazione faceva acqua da tutte le parti.

Ringrazio Silvia Milani per avermi seguito con disponibilità e pazienza nelle misure di spettroscopia.

Ringrazio Massimo Bonini, Emiliano Fratini, Francesca Ridi, Emiliano Carretti e Debora Berti per avermi sempre indicato la strada quando nuove problematiche mi si ponevano davanti.

Ringrazio Marcia Arroyo per il supporto linguistico di spagnolo e Lorenza Bernini per quello culturale.

Ringrazio Giacomo Pizzorusso e Michele Baglioni per essere stati sempre pronti alle emergenze Nanorestore.

Infine ringrazio Marco Lagi, fratello di sventure, per aver sempre assecondato le mie strampalate idee e perché so che continuerà a farlo. Grazie Ma', il supporto tecnico linguistico è stato fondamentale per tesi e articoli.